

Chapter 6

Phenomenological Modeling for Large-Signal Behavior of Ferroelectric Materials



As already discussed in Chap. 3, the electromechanical coupling within piezoelectric materials can be attributed to intrinsic and extrinsic effects. If piezoelectric materials show extrinsic effects, they will be frequently named ferroelectric materials. While intrinsic effects determine the small-signal behavior, extrinsic effects dominate the large-signal behavior of those materials. The small-signal behavior can simply be described through the material law of linear piezoelectricity (see linearization in Fig. 6.1 and Sect. 3.3). In contrast, the large-signal behavior of ferroelectric materials calls for special modeling treatments since it originates from altered geometric alignments of unit cells. Such altered geometric alignments will cause nonlinear as well as hysteretic material behavior (i.e., hysteresis curves) when sufficiently large electrical and/or mechanical loads are applied. Note that this fact is of utmost importance for ferroelectric actuators, which are utilized, e.g., in high-precision positioning systems (cf. Chap. 10).

Ferroelectric actuators usually operate far below their mechanical resonance frequencies. It will, therefore, be reasonable to assume a uniform mechanical displacement along their surfaces if the bottom and top surface are completely covered with electrodes (cf Fig. 4.20 on p. 121). Without limiting the generality, we exclusively consider hereafter electrical and mechanical quantities in the thickness direction (3-direction) of ferroelectric materials. Due to this fact, components in 1-direction and 2-direction as well as indices for 3-direction of the relevant physical quantities can be omitted. Figure 6.1 exemplarily depicts symmetrical hysteresis curves of a ferroelectric material for both the electric polarization $P(E)$ and the mechanical strain $S(E)$ in case of electrical excitation with the electric field intensity E . Mainly, one can distinguish between three different working areas detailed below.

- **Bipolar working area:** The ferroelectric material is alternately driven in positive as well as negative saturation leading to P_{sat}^{\pm} for the electric polarization and S_{sat}^{\pm} for the mechanical strain, respectively. The resulting hysteresis curves $P(E)$

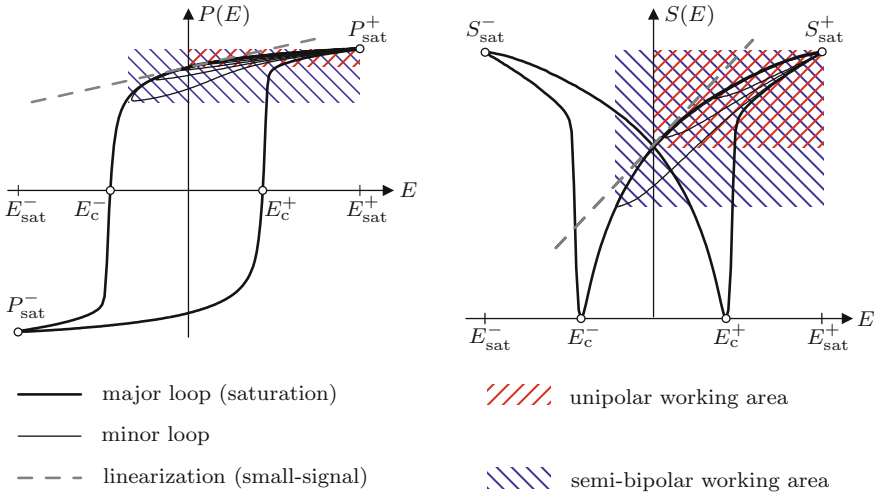


Fig. 6.1 Symmetrical hysteresis curves of ferroelectric materials for electric polarization $P(E)$ and mechanical strain $S(E)$ versus applied electric field intensity E in different working areas; electric polarization P_{sat}^{\pm} and mechanical strain S_{sat}^{\pm} in positive as well as negative saturation, respectively; coercive field intensity E_c^{\pm} ; linearization relates to small-signal behavior of ferroelectric materials

and $S(E)$ (thick lines in Fig. 6.1) are known as major loops. According to its shape, $S(E)$ is also called *butterfly curve*.

- **Unipolar working area:** The ferroelectric material operates with positive or negative electric field intensities, i.e., $E \geq 0$ or $E \leq 0$. Hence, the material can be driven either in positive or negative saturation. Compared to the bipolar working area, mechanical strains and, consequently, mechanical displacements of a ferroelectric actuator get reduced remarkably. The resulting hysteresis curves $P(E)$ and $S(E)$ are referred to as minor loops (thin lines in Fig. 6.1).
- **Semi-bipolar working area:** In contrast to the unipolar working area, the ferroelectric material operates with a larger range of electric field intensities in the semi-bipolar working area. Thereby, one of the conditions $E_c^- < E \leq E_{\text{sat}}^+$ or $E_{\text{sat}}^- \leq E < E_c^+$ (coercive field intensity E_c) has to be fulfilled. As a result, the achievable mechanical strains increase but stay below values of the bipolar working area. The hysteresis curves $P(E)$ and $S(E)$ are again referred to as minor loops.

This chapter primarily deals with Preisach hysteresis modeling, which represents a phenomenological modeling approach for the large-signal behavior of ferroelectric materials in the mentioned working areas. Before we study in Sect. 6.3 alternative phenomenological modeling approaches that also focus on the macroscopic transfer behavior of ferroelectric materials, hysteresis will be mathematically defined. Moreover, an overview of material models on different length scales (e.g., atomistic scale) is given in Sect. 6.2. Contrary to phenomenological modeling approaches, those material models aim at describing the physical behavior of ferroelectric

materials as accurate as possible. In Sect. 6.4, we will introduce the classical Preisach hysteresis operator \mathcal{H}_P , which comprises weighted elementary switching operators. Section 6.5 details different weighting procedures for the elementary switching operators. Because the classical Preisach hysteresis operator is only suitable to a limited extent for predicting hysteretic behavior of ferroelectric actuators in practical applications, a so-called generalized Preisach hysteresis model (operator \mathcal{H}_G) will be introduced in Sect. 6.6. This extended Preisach hysteresis model enables, e.g., the consideration of asymmetric behavior in hysteresis curves. After that, a parameter identification strategy is presented which allows reliable predictions of electrical and mechanical quantities through Preisach hysteresis modeling. To apply Preisach hysteresis modeling in practical applications of ferroelectric actuators (e.g., in high-precision positioning systems), it is of utmost importance to invert the Preisach hysteresis operator. Owing to this fact, Sect. 6.8 finally addresses an iterative inversion procedure, which enables efficient determinations of the aimed electrical excitation signals in a reasonable time. Throughout the whole chapter, piezoceramic disks made of the ferroelectrically soft materials PIC255 (manufacturer PI Ceramic GmbH [71]) as well as Pz27 and the ferroelectrically hard material Pz26 (manufacturer Meggitt Sensing Systems [65]) serve as test objects.

6.1 Mathematical Definition of Hysteresis

There exist various meanings and definitions for the term *hysteresis* in technical areas (e.g., [61, 64]). However, several similarities can be found in these definitions. Here, we especially concentrate on a transmission system with one input $x(t)$ and one output $y(t)$, both depending on time t . When the system exhibits hysteresis¹ in its transmission behavior, three properties will apply to such a system [64, 94]:

1. The output $y(t)$ is clearly defined by the progression of $x(t)$ and the initial state of the transmission system.
2. We can mathematically link $y(t)$ and $x(t)$ with the aid of nonlinear relations describing branches in the xy -plane (see, e.g., Fig. 6.7c). A change between different branches may occur at extrema of the system input $x(t)$.
3. The sequence of extrema in $x(t)$ exclusively determines the progression of the system output $y(t)$. In contrast, values in between these extrema as well as the time response of $x(t)$ do not modify the current output. For this reason, the transmission behavior is rate-independent.

Due to the fact that there always occur creep processes in ferroelectric materials, the third property is, strictly speaking, violated. Nevertheless, the superposition of a rate-independent hysteresis model with an additional approach (e.g., viscoelastic model)

¹Since the system owns one scalar input and one scalar output, the hysteresis is also named *scalar hysteresis*.

can be utilized to consider creeping. Two further properties apply to the large-signal behavior of ferroelectric materials:

4. The current system output $y(t)$ is only influenced by dominating extrema² in $x(t)$. Past extrema of smaller magnitudes than the subsequent ones are deleted in the system history and, thus, do not alter $y(t)$.
5. Because of this *deletion property*, all hysteresis branches in the xy -plane are located within an area, which is given by the last two dominating extrema.

Apart from the listed properties, one can in general distinguish between hysteresis featuring *local memories* or *nonlocal memories* [64].

- Local memories: The upcoming path of $y(t)$ solely depends on the current value of $x(t)$.
- Nonlocal memories: In addition to the current value of the system input, past extrema of $x(t)$ affect the upcoming progression of $y(t)$.

Actually, the large-signal behavior of ferroelectric materials also depends on past extrema. Thus, we have to deal with nonlocal memories.

6.2 Modeling Approaches on Different Length Scales

Aside from the objective, we may classify modeling approaches for ferroelectric materials according to the considered length scale. Basically, five different length scales are known: (i) Atomistic, (ii) mesoscopic, (iii) microscopic, (iv) macroscopic, and (v) multiscale (see Fig. 6.2). In the following, let us briefly discuss selected modeling approaches for ferroelectric materials on these length scales.

Atomistic Scale

At the level of the atomistic scale, one considers processes taking place in the crystal lattice of a material. Thereby, common calculation methods (e.g., *ab initio* and *density functional theory*) from solid-state physics are frequently used. The methods yield quantitative information for lattice spacing, elastic, and stiffness tensors as well as for the spontaneous polarization within ferroelectric materials [16, 97]. Besides, so-called *core-shell models* may be applied to simulate phase transitions and motions of the domain walls [13, 25, 83]. Such models are based on electrostatic interactions among elastically supported cores and shells. Further literature concerning modeling approaches on the atomistic scale can be found in the review articles by Cohen [17] and Sepiarsky et al. [83]. In general, these modeling approaches provide valuable insight for material development. However, the required computational effort restricts their application to small volumes and short time intervals.

²A maximum/minimum will be dominant if its value is smaller/larger than the previous maximum/minimum (see Sect. 6.4).

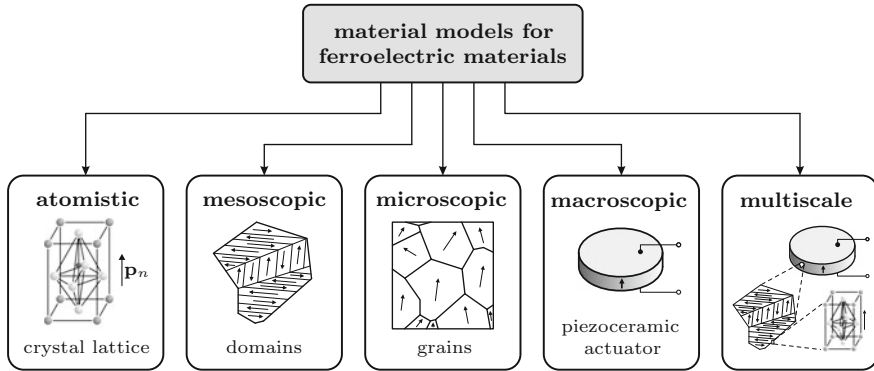


Fig. 6.2 Classification of material models for ferroelectric materials into different length scales [101]

Mesoscopic Scale

Modeling on the mesoscopic scale will be conducted if complex domain structures or lattice defects within ferroelectric materials shall be investigated. Oftentimes, the underlying modeling approaches are based on the *Landau theory*, which is understood as an extension of thermodynamic potentials by an order parameter [53]. Through this order parameter, we can explain phase transitions within materials. Note that such approaches are not only utilized on the mesoscopic scale but also on the microscopic and macroscopic scale. A well-known approach on the mesoscopic scale is the *phase field model*, where the (spontaneous) polarization serves as order parameter [39, 96]. Another method for ferroelectric materials, the *sharp interface approach* [80], is mainly based on two assumptions: (i) Each domain is a homogeneous region and (ii) material properties may jump across domain interfaces.

Microscopic Scale

The microscopic scale is very similar to the mesoscopic scale. That is why there is mostly no clear distinction between modeling approaches on these scales (e.g., [39]). One of the first approaches concerning modeling of ferroelectric materials on the microscopic scale was published by Hwang et al. [42]. They assume that the grains within the material are randomly orientated in the initial state. Since each grain has its own electric polarization, the global polarization state is neutral. By means of energy-based switching criterion depending on both electrical and mechanical excitations, the orientation of the grains is modified. Consequently, the global polarization state as well as the geometric dimension of the investigated ferroelectric material changes. Due to the simplification of equal excitations for every grain, there is a lack of accuracy. However, this modeling approach served as a basis for several further developments [39]. Huber et al. [40] suggest an alternative approach that utilizes crystal plasticity theory instead of energy-based switching criterion. Modeling approaches on the microscopic scale, which additionally consider rate-dependent

behavior, can be found in [4, 9]. An overview of further computation methods is given in the review article by Kamlah [50].

Macroscopic Scale

Modeling approaches on the macroscopic scale lead to a significant reduction in computation time compared to those on the microscopic scale. Several macroscopic modeling techniques are based on the *Landau–Devonshire theory*, which is thermodynamically motivated and can be used to describe phase transitions within ferroelectric materials [21]. The disadvantage of this rate-independent approach lies in the restriction to monocrystalline materials and one-dimensional behavior. Bassiouny et al. [8] presented another thermodynamically consistent approach considering ferroelectricity as well as ferroelasticity. They divided the electric polarization and mechanical strain into a reversible and an irreversible part, respectively. Alternative macroscopic modeling techniques that also exploit separate analysis of reversible and irreversible parts were developed by Kamlah and colleagues [51, 52]. Their approaches rely on phenomenological internal variables for electrical and mechanical quantities. Because electromechanical couplings within ferroelectric materials are considered in both directions, electrical and mechanical excitation can be taken into account at the same time. Further modeling approaches on the macroscopic scale are suggested by Landis [57] and Schröder et al. [81].

Multiscale Approaches

Apart from the approaches on the previously mentioned length scales, there exist various techniques that exploit simultaneous modeling on different scales. These so-called multiscale approaches aim to transfer effects on low abstraction levels to higher ones at reasonable computation time, which is usually achieved by *homogenization methods* within FE simulations. A multiscale approach on the atomistic and the mesoscopic scale was published by Völker et al. [97]. While they use phase field models on the mesoscopic scale, the density functional theory as well as the core-shell model are applied on the atomistic scale. Multiscale approaches combining microscopic and macroscopic scale with the aid of FE simulations can be found in [53, 56, 82, 96]. For instance, Keip [53] presented the *FE Square method* that is based on a microscopic *representative volume element* (abbr. RVE). At each grid point on the macroscopic scale, he deduces appropriate boundary conditions for the RVE. Averaging methods yield effective material parameters on the microscopic scale that can then be applied on the macroscopic scale. Contrary to multiscale approaches based on FE simulations, Smith et al. [84] developed the *homogenized energy model*, which combines mesoscopic and macroscopic scale. Similar to the Landau–Devonshire theory, they introduce a thermodynamically motivated switching criterion on the mesoscopic scale. Stochastic homogenization provides low-order macroscopic models with effective parameters for ferroelectric materials. Ball et al. [7] published an extension of this approach, which enables additional consideration of mechanical stresses.

Overall, the presented approaches on the different length scales aim to model the behavior of ferroelectric materials (e.g., during poling) as accurate as possible. The resulting knowledge facilitates the research on and development of those materials. However, due to the required computational effort, most of the modeling approaches cannot be used to compensate nonlinearities of ferroelectric actuators in practical applications, e.g., positioning. Moreover, the simulation of minor loops poses a problem and the major loops are commonly of angular shape. For all these reasons, we need alternative modeling approaches that allow a sufficiently precise prediction of the actuator behavior in a reasonable computation time. The following section deals with such models for ferroelectric materials.

6.3 Phenomenological Modeling Approaches

In contrast to the approaches in Sect. 6.2, we will discuss here techniques that do not intend to model the real physical behavior of ferroelectric materials. The focus lies exclusively on the scalar transfer behavior of the fabricated transducer (e.g., piezoceramic actuator), i.e., input quantity as well as output quantity in predefined spatial directions. This transfer behavior is simulated through efficient phenomenological models on the macroscopic scale. Several approaches originate from plasticity theory and the research on ferromagnetic materials. For ferroelectric materials, we can classify appropriate phenomenological models into five groups [101]: (i) polynomial description, (ii) rheological models, (iii) Duhem models, (iv) fractional derivatives, and (v) switching operators. The basic principles of these groups are explained below.

Polynomial Description

There can be found many different approaches to simulate the transfer behavior of ferroelectric actuators by means of appropriate polynomials. For instance, Chonan et al. [15] describe branches in hysteresis curves of the mechanical displacement with separately parameterized polynomials for increasing and decreasing input voltage, respectively. In [93], hysteresis loops of ferromagnetic materials are modeled through piecewise linear approximations. Another technique utilizes ellipses to simulate minor loops in the transfer behavior of a piezoceramic actuator [33]. Altogether, it can be stated that polynomial descriptions will yield excellent results for the predicted output if the cycles of the input quantity are well known in advance. However, due to the fact that there is no memory of past inputs, these approaches do not meet the requirements of hysteresis models, which should be valid for general inputs (see Sect. 6.1).

Rheological Models

Basically, the term *rheology* refers to the analysis of mechanical constitutive properties for materials through the construction of ideal bodies, named *rheological models*. In doing so, we combine elementary rheological models in series and in parallel that are given by rheological state equations. Visintin [94] suggests the application of

several of those elementary rheological models representing the main mechanical properties elasticity, viscosity, plasticity as well as strength. Similar to elementary rheological models, one can take advantage of lumped circuit elements from electrical engineering [58]. The parameters of the underlying state equations are derived by comparing model outputs with measurements. Reiländer et al. [76] published such a rheological model to predict the hysteretic behavior of a piezoceramic stack actuator. Further rheological models for ferroelectric actuators can be found in [74, 77].

Duhem Models

The main idea of Duhem models lies in mathematically explaining hysteretic behavior by means of differential equations and integral operators. These phenomenological models are based on the fact that one can only switch between different branches in the hysteresis curve when the derivative of the input changes its sign [61, 94]. A similar property may be attributed to rheological models. Hence, it is oftentimes difficult to distinguish between Duhem and rheological models. Very well-known representatives of generalized Duhem models are *LuGre* as well as *Dahl models* [70, 107]. Although both models can be implemented efficiently, they exhibit a number of drawbacks with regard to applications for ferroelectric materials. For instance, neither asymmetric hysteresis curves nor saturation effects can be simulated. Moreover, the fact that the input history is not considered may lead to physically impossible outputs, e.g., crossing hysteresis curves. An extended version of Duhem models for ferroelectric materials, the so-called *Bouc-Wen model* [100], is utilized for micro as well as nanopositioning (e.g., [59]). Wang et al. [98] presented a modified Bouc-Wen model to predict the hysteretic behavior of a piezoceramic stack actuator. The *Jiles–Atherton model* is a further Duhem model for ferroelectric actuators, which was originally developed for ferromagnetic materials [36, 45]. Also for this phenomenological hysteresis model, one has to cope with physically impossible outputs like unclosed hysteresis loops.

Fractional Derivatives

Another phenomenological approach for modeling hysteresis of ferroelectric materials exploits fractional derivatives. According to models of dry friction in mechanical processes, Guyomar and colleagues [34, 35] describe the electric polarization within the material through an appropriate fractional derivative. They predict the polarization for large electrical excitation with respect to excitation frequency, i.e., the dynamic behavior of ferroelectric materials. In [24], one can find an extended version to additionally consider mechanical stresses in hysteresis curves of the electric polarization. However, so far, there are not known any further approaches based on fractional derivatives, which also allow simulating hysteresis of the mechanical displacement for ferroelectric materials.

Switching Operators

Numerous phenomenological models to describe hysteretic behavior of ferromagnetic and ferroelectric materials use a weighted superposition of elementary switching operators, which are commonly named *hystérons*. Preisach [73] developed such

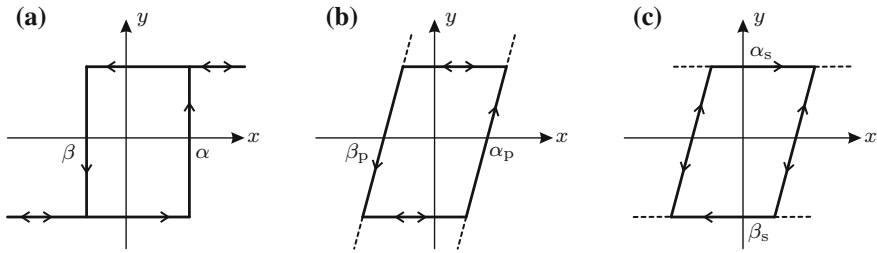


Fig. 6.3 Different elementary switching operators with input x and output y for phenomenological hysteresis models: **a** Relay operator; **b** linear play operator ($\alpha_p = -\beta_p$); **c** linear stop operator ($\alpha_s = -\beta_s$)

a model that was originally motivated by physical processes taking place within ferromagnetic materials during magnetization. With a view to applying the *Preisach hysteresis model* to various physical issues, Krasnosel'skii and Pokrovskii [55] carried out a purely mathematical examination of this approach. Moreover, they investigated three different types of elementary switching operators (see Fig. 6.3): (i) *Relay operators* that are used for Preisach hysteresis models as well as (ii) *linear play operators* (backslash operators) and (iii) *linear stop operators*. The weighted superposition of play and stop operators is commonly referred to as *Prandtl–Ishlinskii model*³ [94].

In case of ferroelectric materials, Prandtl–Ishlinskii models are mostly based on linear play operators (e.g., [43, 75]). Al Janaideh et al. [2] presented an extension of this model to incorporate the rate-dependent behavior of smart actuators. Besides, they suggest a hyperbolic tangent function as generalized play operator, which enables the consideration of saturation effects [3]. A major problem of the play operator lies in the simulation of asymmetric hysteresis curves. Due to this fact, Dong and Tan [23] developed an asymmetric play operator. As alternative approach, Jiang et al. [44] applied especially for piezoelectric actuator systems two separate operators, one for increasing and one for decreasing inputs, respectively.

To sum up, each of the five phenomenological approaches for modeling the hysteresis of ferroelectric materials exhibits advantages and drawbacks. Many of the approaches (e.g., rheological models) have proved to be very efficient in calculation but will yield inadequate results if a precise prediction of the hysteretic behavior is required. Since both the polynomial description and the Duhem models do not use internal variables, the predicted hysteresis curves may be physically impossible, e.g., unclosed hysteresis loops as a result of the Jiles–Atherton approach. Moreover, there are not known phenomenological approaches according to fractional derivatives, which can be applied to simulate both electric polarizations and mechanical displacements of ferroelectric actuators.

³Strictly speaking, Preisach models constitute a special case of Prandtl–Ishlinskii models.

Phenomenological modeling approaches based on switching operators lead to significantly improved results than the other ones. However, in general, the required computational effort to calculate the model output for common implementations is comparatively high. Regarding asymmetric hysteresis curves as well as saturation effects, it can be stated that Preisach models are much more flexible than common Prandtl–Ishlinskii models. Nevertheless, in contrast to Preisach models, we are able to directly invert Prandtl–Ishlinskii models, which is decisive for hysteresis compensation. Besides, Preisach models require more elementary switching operators (i.e., relay operators), but the amount of parameters per a single operator is lower than for Prandtl–Ishlinskii models.

The focus in the present book lies on predicting the hysteretic behavior of ferroelectric actuators for various configurations and practical applications as precise as possible. On account of that fact, we will exclusively discuss Preisach hysteresis models in the following. This includes its efficient implementation (see Sect. 6.4.2) as well as inversion (see Sect. 6.8).

6.4 Modeling of Preisach Hysteresis Operator

In the year 1935, Preisach published a hysteresis model that is commonly known as *classical Preisach hysteresis model* [64, 73]. From the mathematical point of view, this hysteresis model belongs to the phenomenological models. It is often utilized to simulate magnetization of ferromagnetic materials as well as polarization of ferroelectric materials. Owing to the fact that we solely consider scalar inputs and outputs, the subsequent explanations refer to the scalar Preisach hysteresis model and the scalar Preisach hysteresis operator.⁴ Extended versions concerning vector quantities can be found in, e.g., [48, 68, 88].

6.4.1 Preisach Hysteresis Model

To study the Preisach hysteresis model, let us assume a transmission system with the scalar input $x(t)$ and the scalar output $y(t)$, both normalized quantities depending on time t (see Fig. 6.4a). The basic idea of the Preisach hysteresis model lies in the weighted superposition of elementary switching operators $\gamma_{\alpha\beta}$. Each of them features two defined output states, i.e., -1 as well as $+1$. The switching between these two output states may occur when the operator input $x(t)$ reaches one of the changeover points α and β (see Fig. 6.4b). Mathematically, the current state of a single elementary switching operator $\gamma_{\alpha\beta,n}$ with the changeover points α_n and β_n is defined as

⁴For compactness, the term *scalar* is omitted in the following.

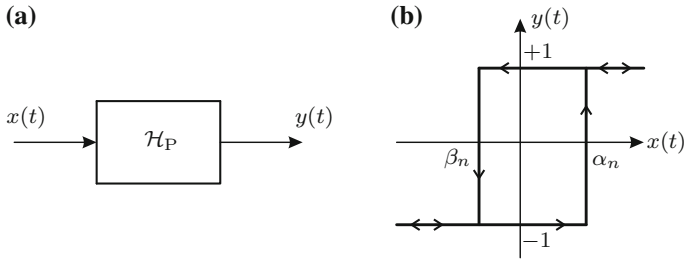


Fig. 6.4 **a** Preisach hysteresis operator \mathcal{H}_P with input $x(t)$ and output $y(t)$, both depending on time t ; **b** elementary switching operator $\gamma_{\alpha\beta,n}$ with changeover points α_n and β_n

$$\gamma_{\alpha\beta,n}[x](t) = \begin{cases} +1 & : x(t) \geq \alpha_n \\ \gamma_{\alpha\beta,n}[x](t^-) & : \beta_n < x(t) < \alpha_n \\ -1 & : x(t) \leq \beta_n \end{cases} \quad (6.1)$$

The operator output will switch from -1 to $+1$ if the operator input $x(t)$ exceeds α_n . When $x(t)$ falls below β_n , switching from $+1$ to -1 will take place. Naturally, the operator will exclusively switch if the previous output does not coincide with the current one. Because each switching operator $\gamma_{\alpha\beta,n}$ retains its output (*i.e.*, $\gamma_{\alpha\beta,n}[x](t^-)$) for $\beta_n < x(t) < \alpha_n$, we are able to simulate system behavior with certain memory. Apart from that fact, the definition of the elementary switching operators implies the condition $\alpha_n \geq \beta_n$ for the changeover points.

According to the idea of Preisach hysteresis models, the weighted superposition of all possible switching operators links the input $x(t)$ to the output $y(t)$ of the transmission system. Therefore, $y(t)$ is given by (see Fig. 6.5)

$$y(t) = \mathcal{H}_P[x](t) = \iint_{\alpha \geq \beta} \mu_{\mathcal{H}}(\alpha, \beta) \gamma_{\alpha\beta}[x](t) \, d\alpha \, d\beta \quad (6.2)$$

Here, $\mathcal{H}_P[x](t)$ stands for the resulting Preisach hysteresis operator, which is applied to the input $x(t)$. The expression $\mu_{\mathcal{H}}(\alpha, \beta)$ individually weights the switching operators and, thus, is usually referred to as *weighting distribution*.

The value range of the changeover points α_n and β_n becomes

$$\mathcal{P} = \{(\alpha_n, \beta_n) \in \mathbb{R}^2 : x_{\min} \leq \beta_n \leq x(t) \leq \alpha_n \leq x_{\max}\} \quad (6.3)$$

with the minimum x_{\min} and the maximum x_{\max} of the input. Since $\alpha \geq \beta$ has to be fulfilled, we can display this value range as triangular in the two-dimensional space with the axis α and β . Each point in this plane relates to exactly one elementary switching operator. Figure 6.6a depicts the triangular as well as three elementary switching operators. If the current outputs (-1 or $+1$) of the switching operators $\gamma_{\alpha\beta}$ are plotted in the triangular, one will obtain the so-called *Preisach plane* $\mathcal{P}(\alpha, \beta)$.

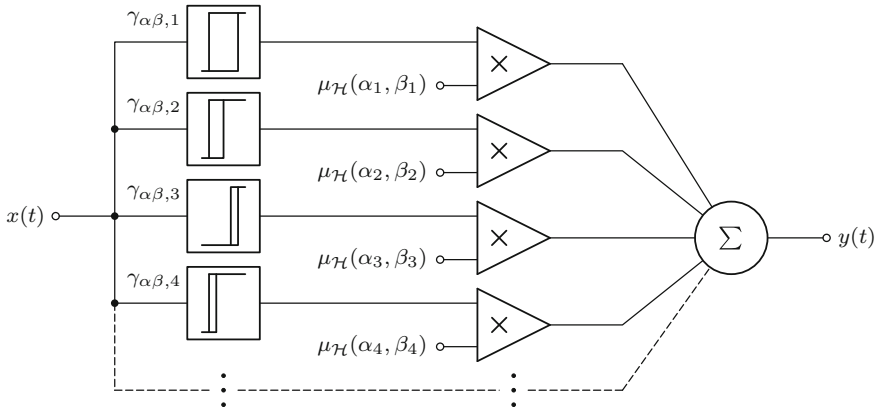


Fig. 6.5 Link of model input $x(t)$ and output $y(t)$ according to Preisach hysteresis model; elementary switching operators $\gamma_{\alpha\beta,n}$ with changeover points α_n and β_n ; individual weights $\mu_{\mathcal{H}}(\alpha_n, \beta_n)$ of elementary switching operators

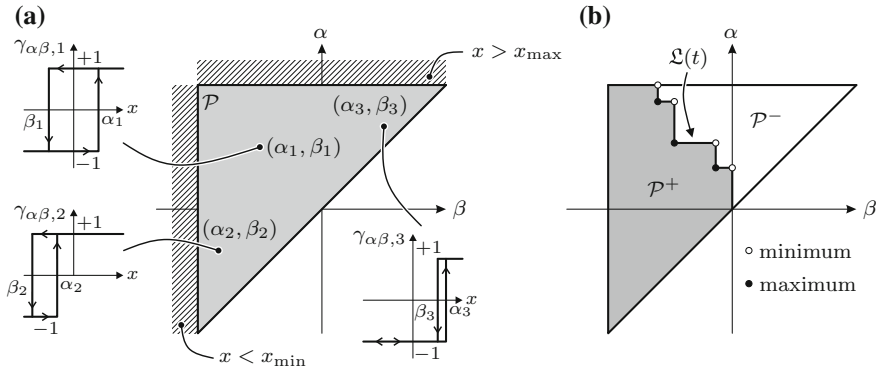


Fig. 6.6 **a** Triangular comprising value range of changeover points α_n and β_n for elementary switching operators $\gamma_{\alpha\beta,n}$; **b** Preisach plane $\mathcal{P}(\alpha, \beta)$ divided into \mathcal{P}^+ and \mathcal{P}^- , which indicate current output value (+1 or -1) of elementary switching operators; dividing line $\mathcal{L}(t)$ containing maxima and minima

Moreover, due to the fact that each elementary switching operator owns his unique weighting $\mu_{\mathcal{H}}(\alpha, \beta)$, the Preisach plane can also be used to show the distribution of weights.

As discussed above, the switching operators $\gamma_{\alpha\beta}$ and, consequently, also the Preisach hysteresis operator $\mathcal{H}_{\mathcal{P}}$ can only change their output if the input is altered, i.e., $\partial x / \partial t \neq 0$. The two possibilities of differential changes in the input lead to

$$\textcircled{A} : \quad \frac{\partial x(t)}{\partial t} > 0 \Rightarrow -1 \longrightarrow +1 \quad \forall \gamma_{\alpha\beta,n} : \alpha_n \leq x(t) \quad (6.4)$$

$$\textcircled{B} : \quad \frac{\partial x(t)}{\partial t} < 0 \Rightarrow +1 \longrightarrow -1 \quad \forall \gamma_{\alpha\beta,n} : \beta_n \geq x(t) , \quad (6.5)$$

which means on the one hand that for increasing inputs, solely the changeover values α_n of $\gamma_{\alpha\beta,n}$ are decisive. On the other hand, decreasing inputs relate to the changeover values β_n . As a result, we obtain at any time two interrelated areas within the Preisach plane \mathcal{P} , namely \mathcal{P}^+ and \mathcal{P}^- , fulfilling the property $\mathcal{P}^+ \cup \mathcal{P}^- = \mathcal{P}$. In those areas, the elementary switching operators take the output values (see Fig. 6.6b)

$$\mathcal{P}^+ = \{ \gamma_{\alpha\beta,n} : \gamma_{\alpha\beta,n} = +1 \} \quad \text{and} \quad \mathcal{P}^- = \{ \gamma_{\alpha\beta,n} : \gamma_{\alpha\beta,n} = -1 \} . \quad (6.6)$$

The dividing line between \mathcal{P}^+ and \mathcal{P}^- is indicated with $\mathcal{L}(t)$. Commonly, this line is a staircase-shaped curve. Depending on the current input $x(t)$ and its history, $\mathcal{L}(t)$ is modified, e.g., the amount of steps is altered.

With a view to explaining the fundamentals of the Preisach hysteresis operator \mathcal{H}_P in more detail, it is convenient to perform a graphical interpretation [36, 101]. In doing so, we choose an input signal $x(t)$ that enables us to discuss the most important characteristics of \mathcal{H}_P . Figure 6.7a and b depict this input signal and the current configuration of the Preisach plane $\mathcal{P}(\alpha, \beta)$ for selected instants of time, namely t_A, \dots, t_N . Furthermore, the operator output $y(t)$ is plotted against the input until the considered instant of time for unweighted elementary switching operators (i.e., $\mu_{\mathcal{H}}(\alpha, \beta) = 1$; Fig. 6.7c) as well as for the weighted ones (Fig. 6.7d). Let us take a look at the different instants of time, which are parameterized with A, ..., N.

- A: The input signal $x(t)$ is assumed to be zero at the beginning of the graphical interpretation. Additionally, the areas \mathcal{P}^+ and \mathcal{P}^- should be equal. In case of a symmetric weighting distribution (i.e., $\mu_{\mathcal{H}}(\alpha, \beta) = \mu_{\mathcal{H}}(-\beta, -\alpha)$), we obtain $y(t) = 0$ as operator output.
- B: According to (6.4), the operators $\gamma_{\alpha\beta}$ will take the output value +1 when $x(t)$ exceeds their changeover points α . Therefore, the dividing line $\mathcal{L}(t)$ between \mathcal{P}^+ and \mathcal{P}^- moves upwards leading to an increase in $y(t)$.
- C: After passing through the virgin curve, $y(t)$ reaches its positive saturation. All elementary switching operators exhibit then the output value +1, i.e., $\mathcal{P} = \mathcal{P}^+$ and $\mathcal{P}^- = \emptyset$.
- D: Similar to B, the operators $\gamma_{\alpha\beta}$ will take the output value -1 when $x(t)$ falls below their changeover points β . As a result, the dividing line $\mathcal{L}(t)$ between \mathcal{P}^+ and \mathcal{P}^- moves to the left yielding a decreasing output $y(t)$.
- E...F: If the input $x(t)$ stays constant (i.e., $\partial x(t)/\partial t = 0$), $\mathcal{L}(t)$ and, consequently, $y(t)$ will remain unchanged.
- G...H: In case of inputs outside of the defined range $x_{\min} \leq x(t) \leq x_{\max}$, $y(t)$ also remains unchanged. Contrary to the positive saturation in C, the Preisach plane becomes $\mathcal{P} = \mathcal{P}^-$ for negative saturation, i.e., $\mathcal{P}^+ = \emptyset$.

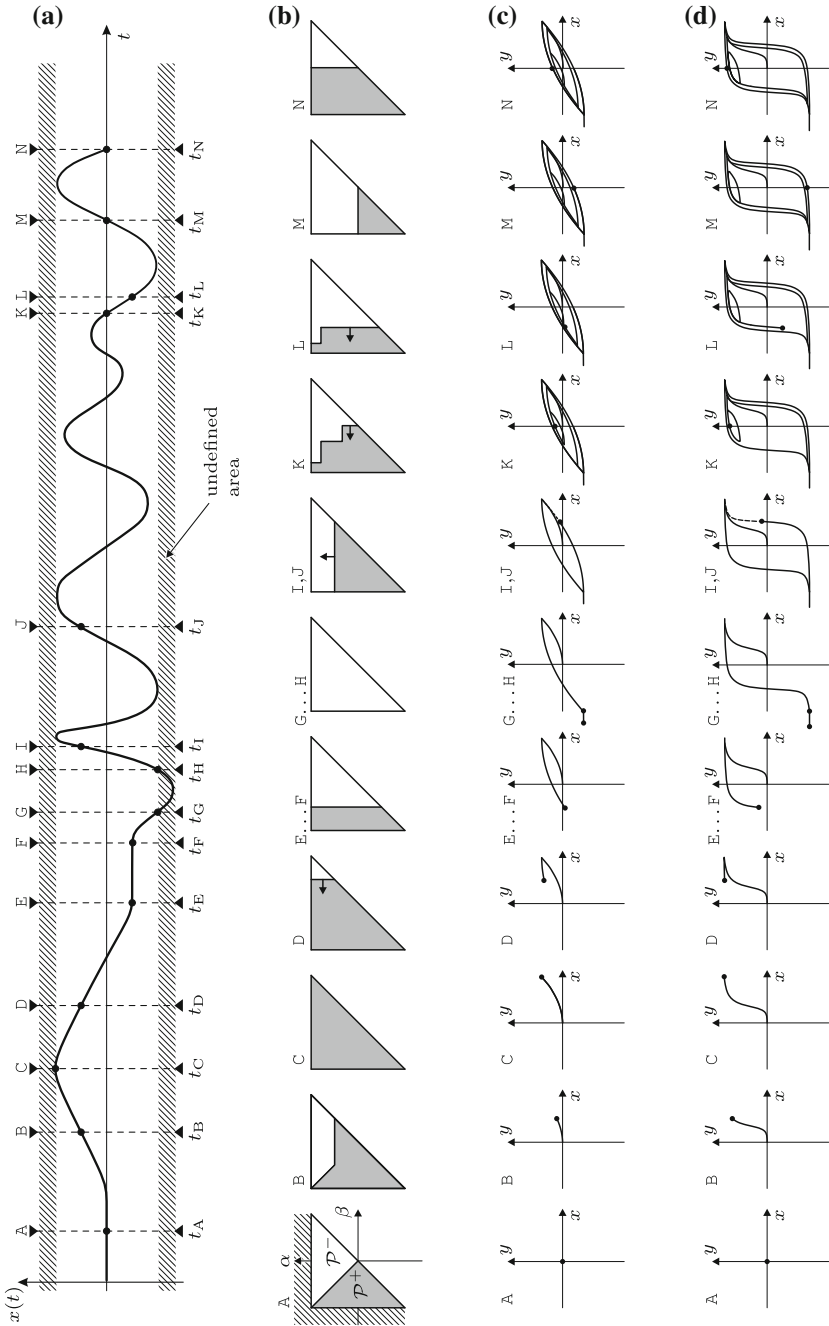


Fig. 6.7 Graphical interpretation of Preisach hysteresis operator \mathcal{H}_P [101]; **a** progression of input signal $x(t)$ with respect to time t ; **b** Preisach plane $\mathcal{P} = \mathcal{P}^+ \cup \mathcal{P}^-$ for A, \dots, N at t_A, \dots, t_N ; operator output y versus input x for **c** unweighted (i.e., $\mu_{\mathcal{H}}(\alpha, \beta) = 1$) and **d** weighted elementary switching operators $\gamma_{\alpha\beta}$

- I, J: Although the slope of $x(t)$ differs for t_I and t_J , the configuration of $\mathcal{P}(\alpha, \beta)$ stays constant, which leads to $y(t_I) = y(t_J)$. We are, therefore, not able to consider a rate-dependent system behavior by means of the classical Preisach hysteresis model.
- K: From t_I to t_K , there occur several successive local extrema in $x(t)$. If one of these maxima/minima is smaller/larger than the previous extrema of the same type, it will be called *dominating extremum*. Such extrema determine the corner points of $\mathcal{L}(t)$ in $\mathcal{P}(\alpha, \beta)$ and, according to the definition of the Preisach hysteresis operator, they affect the subsequent progression of $y(t)$. Due to this fact, we can state that these extrema represent the memory within the hysteresis model.
- L: Inputs that are higher in magnitude than the previous extremum cause movements of $\mathcal{L}(t)$ in horizontal and vertical direction, respectively. Since the previous extremum is deleted in $\mathcal{P}(\alpha, \beta)$, the underlying principle is commonly referred to as *wiping-out rule* or *deletion rule* of the Preisach hysteresis operator.
- M, N: If we do not know the history of $x(t)$, the current configuration of the Preisach plane will also be unknown which makes it impossible to compute subsequent states of $y(t)$. This can be avoided by driving the system into positive or negative saturation. Therewith, a defined state of $\mathcal{P}(\alpha, \beta)$ is achieved.

From the graphical interpretation, two additional key findings arise: (i) Since past extrema of the input affect the current output of \mathcal{H}_p , the classical Preisach hysteresis model is applicable to describe hysteresis exhibiting nonlocal memories. (ii) The comparison of unweighted and weighted elementary switching operators in Fig. 6.7c, d reveals that the distribution of weights $\mu_{\mathcal{H}}(\alpha, \beta)$ has a major influence on the shape of the hysteresis curve. It is, therefore, of utmost importance to identify an appropriate distribution for $\mu_{\mathcal{H}}(\alpha, \beta)$ because only in this way, we can reliably predict the system behavior.

6.4.2 Efficient Numerical Calculation

The Preisach hysteresis operator \mathcal{H}_p and its inversion as well as the identification of the weighting distribution $\mu_{\mathcal{H}}(\alpha, \beta)$ require a large number of individual computation steps. With regard to practical applications of the hysteresis operator, the efficient numerical calculation is, thus, of utmost importance. For this purpose, a novel approach was developed at the Chair of Sensor Technology (Friedrich-Alexander-University Erlangen-Nuremberg) within the framework of the doctoral thesis by Wolf [101]. The key points of the approach are explained in the following.

Discretization

The implementation of the Preisach hysteresis operator on a computer system demands various discretizations, which are listed below.

- The continuous input $x(t)$ is converted to a discrete-time and discrete-value version by an analog-to-digital conversion since the subsequent signal processing is

computer-based. Similarly, the operator output $y(t)$ is a discrete-time and discrete-value signal. Let us assume equidistant sampling with sampling time ΔT . Hence, the available input and output signal become $x(t_k = k\Delta T)$ and $y(t_k = k\Delta T)$, whereas $k \in \mathbb{N}^+$ denotes the index of the sampling point, respectively.⁵ Moreover, $x(k)$ is normalized to its maximum, i.e.,

$$x(k) = \frac{X(k)}{2 \cdot \max(|X(k)|)} \Rightarrow x(k) \in [-0.5, 0.5] \quad (6.7)$$

with $X(k)$ representing the original discrete-time and discrete-value input. For the changeover points α and β of the elementary switching operators $\gamma_{\alpha\beta}$, the normalization leads to the condition $-0.5 \leq \beta \leq \alpha \leq 0.5$.

- According to the definition of the Preisach hysteresis operator \mathcal{H}_p in (6.2), the output results from the input by analytically evaluating a double integral in the two-dimensional space. However, there does not exist an analytical solution for this integral. That is the reason why we have to perform a summation of the spatially discretized triangular instead, which contains discretized values for the changeover points α and β (see Fig. 6.8a). Without limiting the generality, the possible values of both changeover points are discretized in M equally distributed intervals leading to $\alpha(i = 1, \dots, M)$ and $\beta(j = 1, \dots, M)$.
- Due to the discretization of α and β , the configuration of the Preisach plane $\mathcal{P}(\alpha, \beta)$ for time step k as well as the weighting distribution $\mu_{\mathcal{H}}(\alpha, \beta)$ can be written as matrices, both featuring the dimension $M \times M$. They are given by (matrix elements $\mathcal{P}_{ij}(k)$ and μ_{ij})

$$\left. \begin{array}{ll} \mathcal{P}(k) = [\mathcal{P}_{ij}(k)] & \text{with } \mathcal{P}_{ij} \in \{-1, 1\} \\ \boldsymbol{\mu} = [\mu_{ij}] & \text{with } \mu_{ij} \in \mathbb{R}_0^+ \end{array} \right\} \forall (i, j) \in \Lambda. \quad (6.8)$$

Λ represents the definition area of the spatially discretized Preisach plane, i.e., $\Lambda = \{(i, j) : i \leq M + 1, j \leq M + 1 - i\}$. Note that outside of this definition area, the matrix elements $\mathcal{P}_{ij}(k)$ and μ_{ij} are zero, respectively.

The discretization M of α and β determines the resulting discretization of the operator output $y(k)$. A finer discretization leads to a higher resolution of $y(k)$. However, the greater M , the longer the computation will take for common implementations of the Preisach hysteresis operator. On this account, one has to find a compromise between output resolution and computation time. The path toward an implementation enabling both fine discretization and reasonable computation time is detailed below.

Numerical Calculation

As stated above, a weighted summation of the spatially discretized Preisach plane $\mathcal{P}(k)$ is necessary to compute the operator output $y(k)$ for time step k . The double integral in (6.2) changes into the double summation (element μ_{ij} of the weighting

⁵To achieve a compact notation, we use the abbreviation $x(k\Delta T) \hat{=} x(k)$.

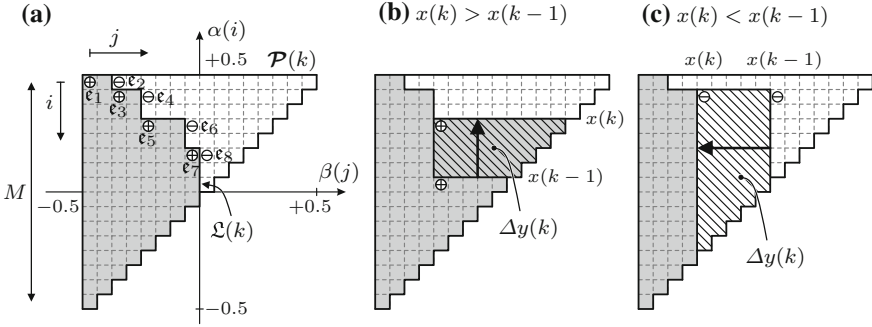


Fig. 6.8 a Spatially discretized Preisach plane $\mathcal{P}(k)$ for time step k ; modification of Preisach plane for **b** increasing and **c** decreasing input $x(k)$ of Preisach hysteresis operator \mathcal{H}_P ; \oplus and \ominus indicate maxima and minima of dominating extrema, respectively

matrix μ)

$$y(k) = \sum_{i=1}^{i_{\max}} \sum_{j=1}^{j_{\max}} \mathcal{P}_{ij}(k) \mu_{ij} \quad \text{with} \quad \begin{cases} i_{\max} = M + 1 - j \\ j_{\max} = M + 1 - i \end{cases} \quad (6.9)$$

Note that $\mathcal{P}_{ij}(k)$ refers to the current state (i.e., $\{-1, 1\}$) of the elementary switching operator $\gamma_{\alpha\beta}$ featuring the changeover points $\alpha(i)$ and $\beta(j)$. Because this calculation is highly inefficient, a differential scheme should be applied instead, which exclusively considers modifications within the Preisach plane $\mathcal{P}(k)$ for time step k . The modifications lead to changes $\Delta y(k)$ in the operator output that are equal to the swept area in the Preisach plane (see Fig. 6.8b and c). A proper method to determine $\Delta y(k)$ is the so-called *Everett function* \mathcal{E} [26]. Therewith, the current output $y(k)$ becomes [36]

$$\begin{aligned} y(k) &= y(k-1) + \Delta y(k) \\ &= y(k-1) + \mathcal{E}(x(k-1), x(k)) \\ &= y(k-1) + \text{sign}(x(k) - x(k-1)) \cdot \iint_{\Delta y(k)} \mu_{\mathcal{H}}(\alpha, \beta) \, d\alpha \, d\beta. \end{aligned} \quad (6.10)$$

The trapezoidal area $\Delta y(k)$ results from the difference of partial areas within the weighted Preisach plane, which are given by the successive inputs $x(k-1)$ and $x(k)$. Depending on the direction of change in the input, $\Delta y(k)$ must be added to (see Fig. 6.8b) or subtracted from (see Fig. 6.8c) the previous output $y(k-1)$. We take this fact into account by the signum function $\text{sign}(\cdot)$.

In order to evaluate the Preisach hysteresis operator \mathcal{H}_P efficiently for each time step k , it is useful to conduct as many calculation steps as possible in advance. The optimized approach mainly comprises the three following substeps.

1. Computation of the Everett Matrix

Since the distribution of the discretized weighting distribution μ_{ij} is time-invariant, we can compute the swept areas in advance, i.e., the Everett function \mathcal{E} . The *Everett matrix* $\mathcal{E} = [\mathcal{E}_{ij}]$ stands for the numerically integrated weighting distribution and reads as

$$\mathcal{E}_{ij} = \sum_{r=i}^{r_{\max}} \sum_{s=j}^{s_{\max}} \mu_{rs} \quad \text{with} \quad \begin{cases} r_{\max} = M + 1 \\ s_{\max} = M + 1 - i \end{cases} \quad (6.11)$$

Each component $\mathcal{E}_{i_n j_n}$ refers to the sum over a triangular ($i \geq i_n$ and $j \geq j_n$) in the weighting matrix μ .

2. Configuration of the Preisach Plane

Now, the Everett matrix \mathcal{E} can be utilized to compute the operator output $y(k)$. In doing so, we require the current dominating extrema of the input history. The extrema are located on the dividing line $\mathcal{L}(k)$ between \mathcal{P}^+ and \mathcal{P}^- . Let us assume $m(k)$ dominating extrema at time step k named $\mathbf{e}_1, \dots, \mathbf{e}_{m(k)}$. The vectors $\mathbf{e}_i(k)$ and $\mathbf{e}_j(k)$ of length $m(k)$ indicate the location of those extrema in the spatially discretized Preisach plane, i.e.,

$$\left. \begin{aligned} \mathbf{e}_i(k) &= [i_1(k), \dots, i_n(k), \dots, i_{m(k)}(k)]^t \\ \mathbf{e}_j(k) &= [j_1(k), \dots, j_n(k), \dots, j_{m(k)}(k)]^t \end{aligned} \right\} \text{with } 1 \leq n \leq m(k) \leq M. \quad (6.12)$$

As we have to distinguish whether the extremum represents a minimum or a maximum (see Fig. 6.8a), an additional vector $\mathbf{s}(k)$ is necessary, which contains the sign of each dominating extremum. This vector of length $m(k)$ is defined as

$$\mathbf{s}(k) = [\mathfrak{s}_1(k), \dots, \mathfrak{s}_n(k), \dots, \mathfrak{s}_{m(k)}(k)]^t \quad (6.13)$$

with

$$\mathfrak{s}_n(k) = \begin{cases} -1 & : i_n = i_{n-1} \quad (\text{minimum}) \\ +1 & : j_n = j_{n-1} \quad (\text{maximum}) \end{cases}. \quad (6.14)$$

For the subsequent time step $k + 1$, the vectors $\mathbf{e}_i(k)$, $\mathbf{e}_j(k)$ as well as $\mathbf{s}(k)$ of the previous time step k need to be updated. Thereby, the following operations are applied:

- When the operator input increases (i.e., $x(k + 1) > x(k)$), the current value $x(k + 1)$ will be compared to the changeover points $\alpha(\mathbf{e}_i(k))$. In case of a decreasing input (i.e., $x(k + 1) < x(k)$), the comparison is carried out with respect to $\beta(\mathbf{e}_j(k))$. According to the definition of i and j (cf. Fig. 6.8a),

an increasing input yields $i_{m(k+1)}(k+1) < i_{m(k)}(k)$ and a decreasing one $j_{m(k+1)}(k+1) < j_{m(k)}(k)$.

- A change of sign in the input slope leads to an additional dominating extremum, i.e., $m(k+1) = m(k) + 1$. Consequently, the length of $\mathbf{e}_i(k)$, $\mathbf{e}_j(k)$ and $\mathbf{s}(k)$ increases by one, respectively.
- If $x(k+1) > \alpha_n(k)$ is fulfilled for increasing input signals, the vectors $\mathbf{e}_i(k)$, $\mathbf{e}_j(k)$ and $\mathbf{s}(k)$ will be shortened to the length $n - 1$. The same applies to decreasing inputs in case of $x(k+1) < \beta_n(k)$. Then, the n th entry of the vectors contains the location of the last dominating extremum in the spatially discretized Preisach plane as well as the sign.

3. Calculation of the Operator Output

The operator output $y(k)$ for time step k results from substep 1 and 2. We use the vectors $\mathbf{e}_i(k)$ and $\mathbf{e}_j(k)$ to select for every dominating extremum of the input $x(k)$ one entry in the Everett matrix \mathcal{E} . Furthermore, the selected entries are superimposed with respect to the signs of the dominating extrema, which are listed in $\mathbf{s}(k)$. Altogether, $y(k)$ computes as

$$y(k) = \frac{1}{2} \mathcal{E}_{i_1(k)j_1(k)} \cdot \mathbf{s}_1(k) + \sum_{n=2}^{m(k)} \mathcal{E}_{i_n(k)j_n(k)} \cdot \mathbf{s}_n(k) . \quad (6.15)$$

By means of this approach, the evaluation of the Preisach hysteresis operator is optimized. Compared to the common implementation of the Everett function (6.10), we can reduce the computation time by a factor of more than 100 [101]. Since the common implementation is mostly restricted to discretizations $M < 100$ of the Preisach plane, additional interpolation algorithms are required to achieve a reasonable resolution of the operator output [36, 76]. In contrast, the presented approach allows fine discretizations (e.g., $M = 300$) and, therefore, a high resolution without any interpolation.

6.5 Weighting Procedures for Switching Operators

As has been shown in Fig. 6.7, the weighting distribution $\mu_{\mathcal{H}}(\alpha, \beta)$ remarkably affects the output of the Preisach hysteresis operator \mathcal{H}_P and, therefore, the resulting hysteresis curve. That is the reason why one can find numerous publications addressing identification as well as description of $\mu_{\mathcal{H}}(\alpha, \beta)$ for ferromagnetic and ferroelectric materials.

Before we study suitable weighting procedures and identifications, let us deduce physically motivated properties of $\mu_{\mathcal{H}}(\alpha, \beta)$. Switching processes taking place within ferroelectric materials arise from complex interactions of mechanical and electric fields on mesoscopic as well as microscopic length scales. We do not consider such interactions because the Preisach hysteresis operator represents a purely phenomenological modeling approach. However, from the macroscopic point of view,

there occurs a statistical accumulation of domains, which show a specific switching property that is very well explained by selected elementary switching operators $\gamma_{\alpha\beta}$. Consequently, the weights $\mu_{\mathcal{H}}(\alpha, \beta)$ for these elementary switching operators have to possess high numerical values. In this context, four assumptions can be made for simulating the large-signal behavior of ferroelectric materials by means of Preisach hysteresis models:

1. A positive change in the electric field intensity $E(t)$ with time increases the electric polarization $P(t)$ of the ferroelectric material. In the same way, a negative change reduces $P(t)$. Therefore, the weight $\mu_{\mathcal{H}}(\alpha, \beta)$ for each elementary switching operator has to be positive, i.e.,

$$\mu_{\mathcal{H}}(\alpha, \beta) > 0 \quad \forall \alpha, \beta : -0.5 \leq \beta \leq \alpha \leq +0.5 . \quad (6.16)$$

2. The switching behavior of unloaded domains within ferroelectric materials is assumed to be symmetrical. Elementary switching operators with the changeover points $\alpha = -\beta$ emulate this behavior. As a consequence, we can expect that the weights for those operators are rather large.
3. If ferroelectric materials are excited with a symmetric electrical signal regarding its magnitude, the resulting magnitude of $P(t)$ will be mostly symmetrical, too. To consider such material behavior, the weighting distribution $\mu_{\mathcal{H}}(\alpha, \beta)$ should be symmetrical about the axis $\alpha = -\beta$, i.e., $\mu_{\mathcal{H}}(\alpha, \beta) = \mu_{\mathcal{H}}(-\beta, -\alpha)$.
4. As hysteresis curves of the electric polarization indicate, the steepest slope is reached close to the coercive field intensity E_c^\pm . This implies that, statistically, the majority of domains within ferroelectric materials will switch when the applied electric field intensity is similar to E_c^\pm . In the weighting distribution, the normalized coercive field intensities e_c^\pm are located at the axis $\alpha = -\beta$. Hence, there also arise the maximum values of the weights.

Principally, one can distinguish between two approaches to determine weighting distributions $\mu_{\mathcal{H}}(\alpha, \beta)$ for the Preisach hysteresis model: (i) $\mu_{\mathcal{H}}(\alpha, \beta)$ is spatially discretized in elements and (ii) $\mu_{\mathcal{H}}(\alpha, \beta)$ is defined through an analytical function. We will study the main aspects of selected implementations for both approaches in Sects. 6.5.1 and 6.5.2.

6.5.1 Spatially Discretized Weighting Distribution

Here, let us concentrate on two different implementations to obtain the spatially discretized weighting distribution $\mu = [\mu_{ij}]$. While the first implementation is based on *first-order reversal curves* (FORCs), the second one minimizes deviations between appropriate measurements and simulations.

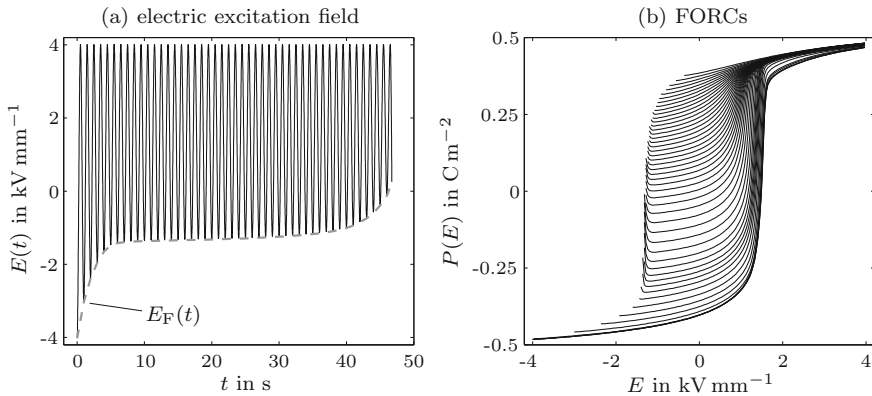


Fig. 6.9 **a** Possible input signal $E(t)$ to obtain FORCs (first-order reversal curves) for ferroelectric materials; reversal field intensity $E_F(t)$; **b** resulting FORCs for piezoceramic disk (diameter 10.0 mm; thickness 2.0 mm; material PIC255)

First-Order Reversal Curves

First-order reversal curves result from alternately loading the investigated material with a particular sequence of increasing and decreasing input signals. In case of ferroelectric materials, such a sequence starts at the electric field intensity E_{sat}^- , which leads to the negative saturation $P(E_{\text{sat}}^-)$ of the electric polarization. The electric field intensity is always increased up to positive saturation (i.e., E_{sat}^+) and, then, reduced again to a value slightly higher than the previous minimum (see Fig. 6.9a). Consequently, the local minimum $E_F(t)$ (reversal field intensity) of the input increases and its maximum remains constant with respect to time t . For the mentioned input sequence, the FORCs are defined as part of the hysteresis curve ranging from local minimum $P(E_F)$ to global maximum $P(E_{\text{sat}}^+)$, respectively (see Fig. 6.9b).

Mayergoyz [62, 64] exploited FORCs to identify spatially discretized weighting distributions for ferromagnetic materials. In doing so, he evaluated the second-order partial derivative of the acquired FORCs and performed a special coordinate transform. Some research groups (e.g., Stanco et al. [86] and Stoleriu et al. [87]) applied a similar approach for characterizing ferroelectric materials. However, the identification of the spatially discretized weighting distribution μ for those materials through FORCs exhibits various drawbacks [101]. The main drawbacks are the following:

- The slope steepness in hysteresis curves for ferroelectric materials is usually much larger than for ferromagnetic materials. Since especially at the steepest slopes, most switching processes of the unit cells take place within the ferroelectric materials, one has to change the reversal field intensity $E_F(t)$ slowly (see Fig. 6.9a). For this reason, the required measurement effort increases remarkably.
- To some extent, there occur negative entries in the identified μ for ferroelectric materials, which result from creep effects during the extensive FORCs acquisition.

Strictly speaking, such negative entries contradict the previously deduced Assumption 1 (see p. 214) for the weighting distribution.

- With a view to measuring FORCs, the investigated ferroelectric material has to reach its negative as well as positive saturation. It seems only natural that this is not always possible in practical applications of actuators, which incorporate such materials.
- The Preisach hysteresis model will be particularly well suited for predicting hysteretic behavior of materials if the input signals for identification are similar to those in the application. However, FORCs result from a predefined input sequence ranging from negative to positive saturation. Owing to this fact, we favor identification procedures allowing a flexible choice of input sequences instead.

According to the listed drawbacks, alternative approaches (see, e.g., Sect. 6.5.2) are required which yield weighting distributions for ferroelectric materials.

Adjustment of Simulations

Contrary to the previously mentioned method for the identification of μ , Kaltenbacher and Kaltenbacher [49] suggest an approach that is based on comparing measurements to outputs of the Preisach hysteresis operator \mathcal{H}_p . Hegewald [36, 37] firstly applied this approach for ferroelectric materials. To distinguish the resulting spatially discretized weighting distribution from the later ones, let us introduce the notation $\mu_{\text{HEG}} = [\mu_{\text{HEG},ij}]$, which represents the aimed quantity. The principal idea of the approach is minimizing the least squares error between normalized acquired data for the electric polarization $p_{\text{meas}}(k)$ and predicted model outputs, i.e., (time step $k = 1, \dots, k_{\text{max}}$)

$$\min_{\mu_{\text{HEG}}} \sum_{k=1}^{k_{\text{max}}} \left[p_{\text{meas}}(k) - \sum_{i=1}^{i_{\text{max}}} \sum_{j=1}^{j_{\text{max}}} \mathcal{P}_{ij}(k) \cdot \mu_{\text{HEG},ij} \right]^2. \quad (6.17)$$

Thereby, the matrix elements $\mu_{\text{HEG},ij}$ are iteratively adjusted in a convenient way. If the changeover points α and β of the elementary switching operators $\gamma_{\alpha\beta}$ are discretized in M intervals, respectively, μ_{HEG} will contain $n_{\text{HEG}} = (M^2 + M)/2$ independent entries.

In the following, we take a look at results for a piezoceramic disk (diameter 10.0 mm; thickness 2.0 mm), which is made of the ferroelectrically soft material Pz27. To experimentally determine the electric polarization P in thickness direction, a *Sawyer–Tower circuit* [79] was utilized,⁶ i.e., an additional capacitor C_{ST} was connected in series to the investigated piezoceramic disk. Note that C_{ST} has to feature a high capacitance value as well as a high insulating resistance. Figure 6.10a depicts both measured hysteresis curves $P_{\text{meas}}(E)$ and simulated ones $P_{\text{sim}}(E)$ with respect to the applied electric field intensity E . The waveform of $E(t)$ that was utilized for exciting the piezoceramic disk is shown in Fig. 6.10e. This waveform also served as input sequence to identify μ_{HEG} through minimizing the least squares error (6.17).

⁶The Sawyer–Tower circuit was applied for all measurements of P in this chapter.

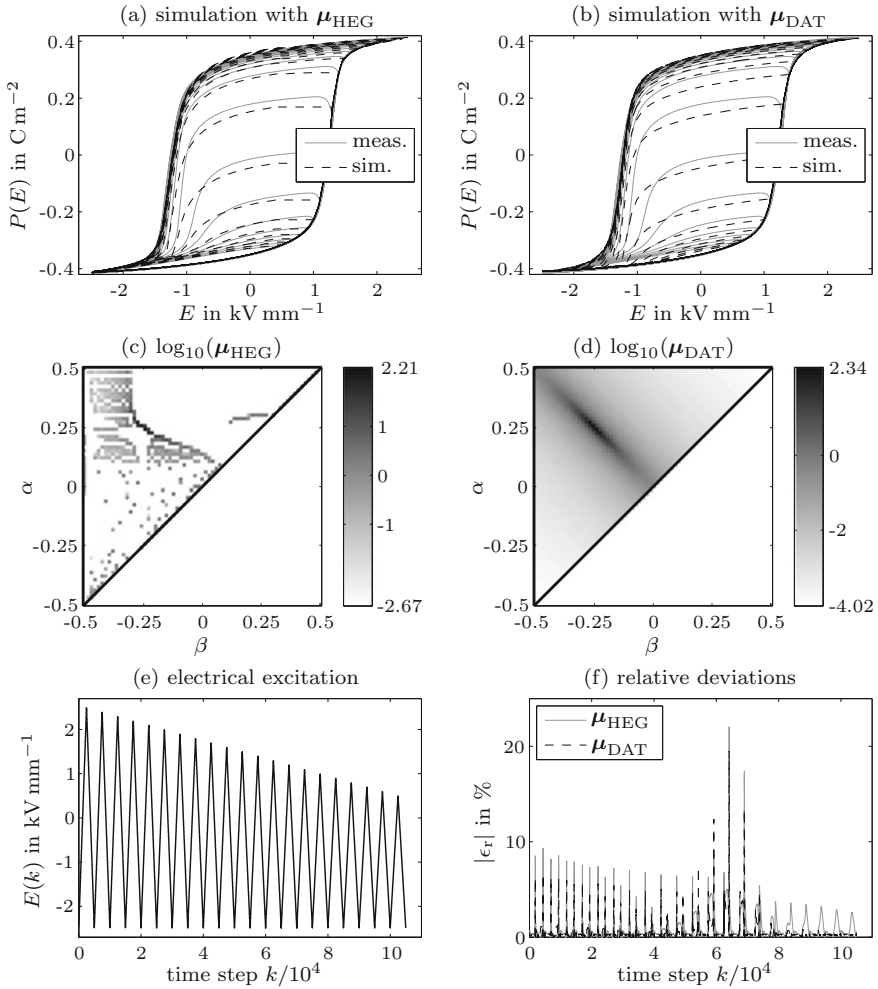


Fig. 6.10 Comparison of measurements and simulations for $P(E)$ in case of **a** μ_{HEG} and **b** μ_{DAT} ; **c** and **d** spatially discretized weighting distributions for $M = 67$; **e** electrical excitation $E(k)$ for identifying μ_{HEG} and μ_{DAT} ; **f** normalized relative deviations $|\epsilon_r|$ (magnitude) between simulations and measurements; piezoceramic disk (diameter 10.0 mm; thickness 2.0 mm; material Pz27)

As the comparison in Fig. 6.10a reveals, $P_{\text{meas}}(E)$ and $P_{\text{sim}}(E)$ coincide very well. The deviations between them can be mainly ascribed to creep processes, which we do not consider in the classical Preisach hysteresis model. Even though the excitation signal refers to a large operating range of the piezoceramic disk, the simulation procedure yields promising results.

The identified spatially discretized weighting distribution μ_{HEG} for $M = 67$ intervals (i.e., $n_{\text{HEG}} = 2278$ entries) is given in Fig. 6.10c. μ_{HEG} exhibits a wide value range and only for a few combinations of changeover points, the obtained weights

are large. Actually, the majority of weights is rather small. This may lead to problems when the dividing line $\mathcal{L}(t)$ (cf. Fig. 6.6b) crosses isolated regions of small weights since the operator output will hardly change [101]. Moreover, μ_{HEG} is strongly asymmetric, which does not agree with the deduced Assumption 3 (see p. 214). Besides, due to the fact that n_{HEG} parameters have to be modified in each iteration step, the minimizing procedure for the identification of μ_{HEG} limits M to small values. As a consequence, the Preisach plane \mathcal{P} is also roughly discretized. We require, therefore, an additional interpolation method to handle operator inputs between the discretized values of the changeover points α and β .

To summarize, one can state that the adjustment of simulations to measurements is a much better option to determine spatially discretized weighting distributions for ferroelectric materials than the approach based on FORCs. From the practical point of view, the large amount of required parameters n_{HEG} , however, may cause significant problems, e.g., uniqueness as well as robustness of the identified parameters.

6.5.2 Analytical Weighting Distribution

Alternatively to determining the individual entries of the spatially discretized weighting distribution, we can describe $\mu_{\mathcal{H}}(\alpha, \beta)$ through analytical functions. Such an analytical function is desired to fulfill three properties:

1. The analytical description of the weighting distribution should enable reliable modeling for different working areas of ferroelectric actuators, i.e., unipolar, semi-bipolar as well as bipolar working areas.
2. With a view to uniquely identifying the parameters of the analytical function, each parameter should exclusively modify one property of the hysteresis curve, e.g., slope steepness.
3. The analytical function for $\mu_{\mathcal{H}}(\alpha, \beta)$ should be defined by a small number of parameters.

If an analytical function fulfills these properties, we will be able to describe and to identify weighting distributions for Preisach hysteresis models in a rather simple manner. Property 2 is especially useful to consider additional influencing factors (e.g., mechanical prestress) on hysteresis curves by means of generalized Preisach hysteresis models (see Sect. 6.6). Concerning property 3, it is essential to find a good compromise between number of parameters and desired accuracy of the model output. Although an increased number of parameters may lead to a better accuracy, the uniqueness of the parameters is remarkably reduced.

Analytical functions for defining weighting distributions do not specify the spatial discretization M of the Preisach plane \mathcal{P} in advance. Consequently, the actual weight $\mu_{\mathcal{H}}(\alpha, \beta)$ can be computed for each combination of changeover points without performing any interpolation. Note that from the practical point of view, one also has to carry out spatial discretization since this is required for efficient numerical

evaluations of the Preisach hysteresis operator \mathcal{H}_P (see Sect. 6.4.2). Nevertheless, M for identifying the parameters of the analytical function and for utilizing \mathcal{H}_P in practical applications can differ.

DAT Function

As saturation curves are quite similar to an arctangent function, Sutor et al. [89] suggest a special analytical function for describing $\mu_{\mathcal{H}}(\alpha, \beta)$, which is based on the second-order derivative of the arctangent function. The second-order derivative is attributable to the double integral within Preisach hysteresis models (see (6.2)). For this reason, the underlying function is commonly named *DAT* (derivative arc tangent) function and reads as

$$\mu_{\text{DAT}}(\alpha, \beta) = \frac{B}{1 + \{[(\alpha + \beta) \sigma]^2 + [(\alpha - \beta - h) \sigma]^2\}^\eta} \quad (6.18)$$

with four independent parameter ($n_{\text{DAT}} = 4$) yielding the dimensionless parameter vector $\mathbf{p} = [B, \eta, h, \sigma]^t$. Originally, the DAT function was intended for modeling ferromagnetic materials. Wolf et al. (e.g., [104, 106]) utilized this analytical function to predict the large-signal behavior of ferroelectric materials through the Preisach hysteresis operator. In the following, let us concentrate on an extended version of the DAT function [101], which is given by

$$\mu_{\text{DAT}}(\alpha, \beta) = \frac{B}{1 + \{[(\alpha + \beta + h_1) \sigma_1]^2 + [(\alpha - \beta - h_2) \sigma_2]^2\}^\eta} \quad (6.19)$$

and, thus, contains six independent parameters, i.e., $\mathbf{p} = [B, \eta, h_1, h_2, \sigma_1, \sigma_2]^t$ and $n_{\text{DAT}} = 6$. Compared to (6.18), the extended DAT function⁷ is more flexible but exhibits two additional parameters. We arrive at the discretized weighting distribution $\boldsymbol{\mu}_{\text{DAT}} = [\mu_{\text{DAT},ij}]$ by spatially discretizing the Preisach plane in M equally distributed intervals for the changeover points α and β . Again, the discretized version $\boldsymbol{\mu}_{\text{DAT}}$ contains $(M^2 + M)/2$ entries.

Figure 6.11 displays a particular weighting distribution $\mu_{\text{DAT}}(\alpha, \beta)$ according to the DAT function as three- and two-dimensional representation in the Preisach plane \mathcal{P} , respectively. The pronounced maximum is affected by the parameters of the analytical function in a different manner. The individual impacts on the weighting distribution and on the resulting hysteresis curve (see Fig. 6.12) are as follows:

- B exclusively scales $\mu_{\text{DAT}}(\alpha, \beta)$ and, therefore, modifies the magnitude of hysteresis curves. We can utilize B to compensate unwanted changes in hysteresis curves due to the parameters η , σ_1 , and σ_2 .
- η prevalently affects the shape of the maximum in $\mu_{\text{DAT}}(\alpha, \beta)$. For instance, a large value for η causes a steep decrease of this maximum. Consequently, the slope steepness of hysteresis curves is specified.

⁷The extended version of the DAT function is hereinafter also called DAT function.

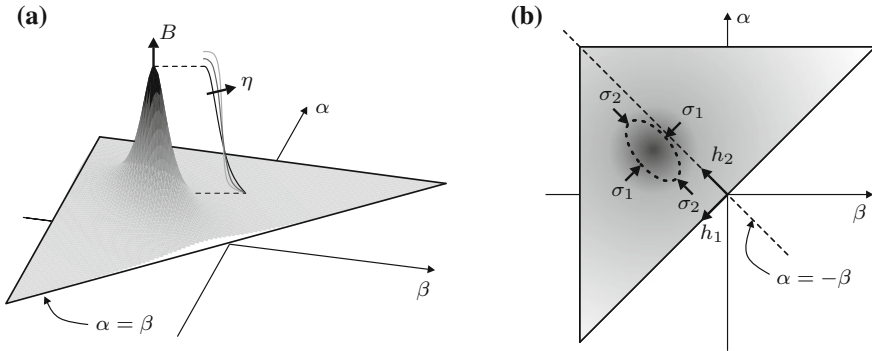


Fig. 6.11 Influence of parameters B , η , h_1 , h_2 , σ_1 , and σ_2 on weighting distribution $\mu_{\text{DAT}}(\alpha, \beta)$ in Preisach plane \mathcal{P} ; **a** three-dimensional and **b** two-dimensional representation

- h_1 shifts the maximum of $\mu_{\text{DAT}}(\alpha, \beta)$ in \mathcal{P} along the axis $\alpha = \beta$. This parameter is especially important for modeling asymmetric hysteresis curves, which may be caused by, e.g., a bias e_{bias} in the normalized electric field intensity (see Sect. 6.6.2).
- h_2 shifts the maximum of $\mu_{\text{DAT}}(\alpha, \beta)$ in \mathcal{P} along the axis $\alpha = -\beta$. In case of ferroelectric materials, we are able to vary the normalized coercive field intensity e_c^\pm of hysteresis curves through h_2 .
- σ_1 and σ_2 modify the maximum's width of $\mu_{\text{DAT}}(\alpha, \beta)$ in direction of the axes $\alpha = \beta$ and $\alpha = -\beta$, respectively. As a result, one alters magnitudes of hysteresis curves as well as shapes of minor loops.

In summary, the DAT function is able to specifically influence decisive properties of simulated hysteresis curves for ferroelectric materials, e.g., coercive field intensity and slope steepness. As already discussed, this fact is especially important for generalized hysteresis models based on the Preisach hysteresis operator.

Just as it is suggested by Hegewald [37] for identifying the entries of μ_{HEG} , the parameters B , η , h_1 , h_2 , σ_1 , and σ_2 of the DAT function result from iterative adjustments of model outputs to appropriate measurements. In doing so, we have to minimize deviations between simulated and measured signals. The underlying optimization procedure represents an ill-posed problem (see Chap. 5). Hence, we require an appropriate regularization approach, which is provided by the Levenberg–Marquardt algorithm and the iteratively regularized Gauss–Newton algorithm. Both algorithms yield the aimed parameters for the DAT function in reasonable computation time but demand a proper initial guess for the parameter vector \mathbf{p} . Such an initial guess can be figured out by manually adjusting simulations to measurements. In [101], robustness as well as reliability of the entire parameter identification is proven through different examples.

With a view to comparing the different weighting procedures μ_{DAT} and μ_{HEG} , let us also apply the DAT function to the previously mentioned measurement data for the piezoceramic disk (diameter 10.0 mm; thickness 2.0 mm; material Pz27). Figure 6.10d depicts the identified spatially discretized weighting distribution μ_{DAT}

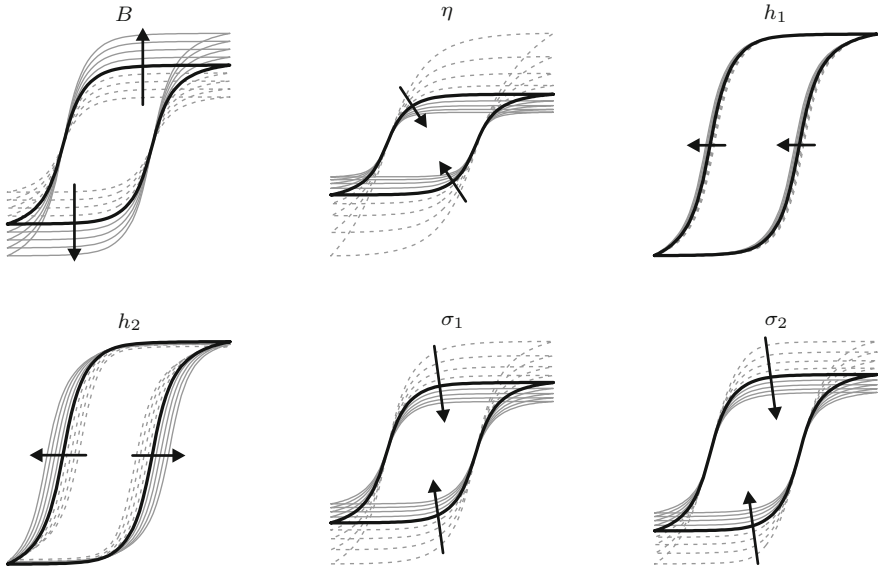


Fig. 6.12 Parameter study for DAT function $\mu_{\text{DAT}}(\alpha, \beta)$ to individually rate impacts of $B, \eta, h_1, h_2, \sigma_1,$ and σ_2 on hysteresis curves, e.g., $P(E)$; parameters are varied in the range $\pm[10, 20, 30, 40]\%$; dashed and solid lines refer to negative and positive parameter changes, respectively; arrows indicate increasing parameter values [101]

for $M = 67$ intervals. In contrast to $\mu_{\text{HEG}}, \mu_{\text{DAT}}$ is symmetrical about the axis $\alpha = -\beta$, which coincides with Assumption 3 (see p. 214). Furthermore, there do not arise isolated regions in μ_{DAT} where the weights exhibit negligible values. This fact is a consequence of the utilized analytical function.

As the comparisons of measurements $P_{\text{meas}}(E)$ and simulations $P_{\text{sim}}(E)$ for the electric polarization in Fig. 6.10a and b reveal, μ_{HEG} and μ_{DAT} lead to prediction results of similar quality. Even though the DAT function is defined by a much smaller amount of independent parameters (i.e., $n_{\text{DAT}} \ll n_{\text{HEG}}$), which also facilitates their identification, the normalized relative deviations⁸ ϵ_r between $P_{\text{meas}}(E)$ and $P_{\text{sim}}(E)$ for μ_{DAT} are only marginally higher than for μ_{HEG} (see Fig. 6.10f). It is, thus, reasonable to assume that μ_{DAT} and μ_{HEG} feature identical performance. However, from the physical point of view, the resulting weights μ_{DAT} are more reliable than μ_{HEG} . Because of the aforementioned arguments, the DAT function should be generally preferred to identify weighting distributions for Preisach hysteresis operators.

Gaussian Function and Lorentz Function

There exist several further analytical functions to describe the weighting distribution $\mu_{\mathcal{H}}(\alpha, \beta)$ for Preisach hysteresis models. Especially in case of ferromagnetic

⁸In this book, the normalized relative deviation ϵ_r usually indicates the absolute deviation related to the difference between the considered maximum and minimum.

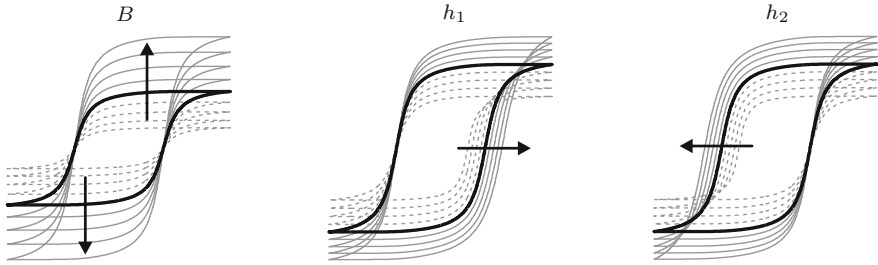


Fig. 6.13 Parameter study for Lorentz function $\mu_{\text{LOR}}(\alpha, \beta)$ to individually rate impacts of B , h_1 and h_2 on hysteresis curves, e.g., $P(E)$; parameters are varied in the range $\pm[10, 20, 30, 40]\%$; dashed and solid lines refer to negative and positive parameter changes, respectively; arrows indicate increasing parameter values [101]

materials, the analytical functions are oftentimes motivated by statistical accumulations of switching processes taking place within the material. In order to consider this fact, one can use two-dimensional *Gaussian* and *Lorentz distributions* for analytical description (e.g., [5, 20, 27, 90]). As Azzeroni et al. [6] suggest in a similar manner, the Gaussian and Lorentz function (distribution) are given by

$$\mu_{\text{GAUSS}}(\alpha, \beta) = B^2 \cdot \exp \left[-\frac{1}{2} \left(\frac{\alpha - \beta - 2h_1}{h_1} \sigma_1 \right)^2 - \frac{1}{2} \left(\frac{\alpha + \beta}{h_2} \sigma_2 \right)^2 \right] \quad (6.20)$$

$$\mu_{\text{LOR}}(\alpha, \beta) = \frac{B}{1 + \left(\frac{\beta + h_1}{h_1} \sigma_1 \right)^2} \cdot \frac{B}{1 + \left(\frac{\alpha - h_2}{h_2} \sigma_2 \right)^2}, \quad (6.21)$$

respectively. The impacts of the parameters B , h_1 , h_2 , σ_1 , and σ_2 on the weighting distribution approximately correspond to those of the DAT function. Again, B exclusive scales the magnitude of $\mu_{\text{GAUSS}}(\alpha, \beta)$ and $\mu_{\text{LOR}}(\alpha, \beta)$, which is equal to scaling hysteresis curves. Through the parameters σ_1 and σ_2 , we alter slope steepness in hysteresis curves. However, in distinction from the DAT function, h_1 as well as h_2 do not allow an independent adjustment of the normalized coercive field intensity e_c^\pm (see Figs. 6.12 and 6.13). They also change magnitudes of major loops, which may cause problems during parameter identification. On account of these facts, both the Gaussian function and the Lorentz function are not optimally suited for generalized Preisach hysteresis models.

Figure 6.14a shows measured and simulated major loops for the electric polarization $P(E)$ of a piezoceramic disk (diameter 10.0 mm; thickness 2.0 mm; material Pz27). The identified spatially discretized weighting distributions μ_{DAT} , μ_{GAUSS} as well as μ_{LOR} are depicted in Fig. 6.14b–d; Table 6.1 contains the underlying parameters. In general, μ_{DAT} , μ_{GAUSS} as well as μ_{LOR} lead to reliable model outputs of the Preisach hysteresis operator. A more detailed comparison, however, points out that the deviations between measurements and simulations with the Gaussian function

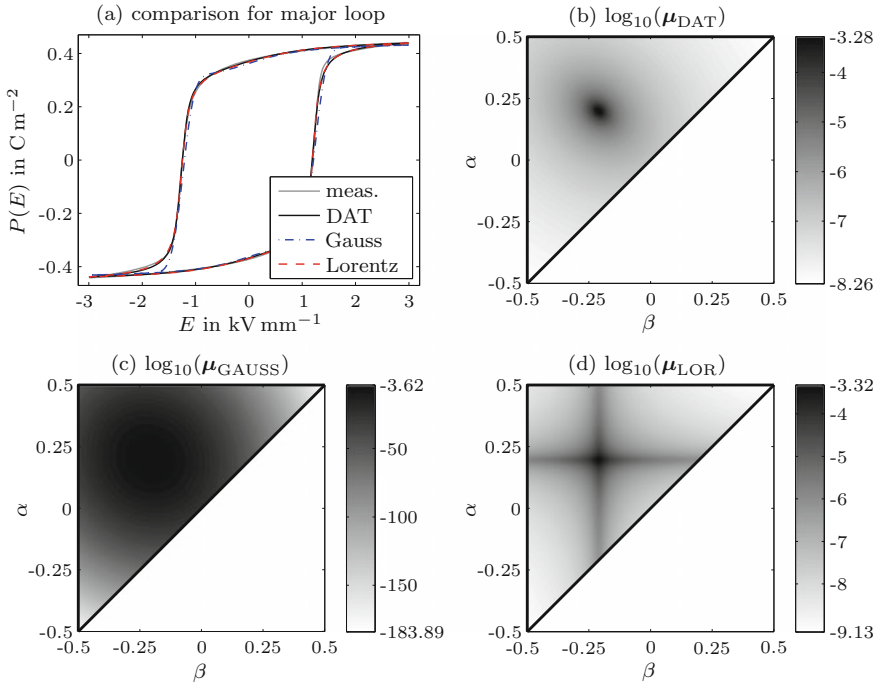


Fig. 6.14 a Comparison of measured and simulated major loops $P(E)$ for different analytical weighting distributions; **b**, **c**, and **d** resulting spatially discretized weighting distributions for $M = 800$; piezoceramic disk (diameter 10.0 mm; thickness 2.0 mm; material Pz27)

Table 6.1 Resulting parameters for DAT function $\mu_{\text{DAT}}(\alpha, \beta)$, Gaussian function $\mu_{\text{GAUSS}}(\alpha, \beta)$, and Lorentz function $\mu_{\text{LOR}}(\alpha, \beta)$; parameters a and b refer to reversible parts (see Sect. 6.6.1) in hysteresis curve

	B	η	h_1	h_2	σ_1	σ_2	a	b
DAT	338.105	1.467	0.010	0.411	47.12	36.30	0.052	5.34
Gaussian	0.016	—	0.206	0.119	5.06	3.20	0.053	7.30
Lorentz	0.022	—	0.200	0.211	13.20	12.08	0.051	5.05

are significantly higher than those with the DAT function as well as Lorentz function. Close to the reversal points of the applied electric field intensity E , measurements and simulations with μ_{GAUSS} differ considerably. Hence, $\mu_{\text{DAT}}(\alpha, \beta)$ and $\mu_{\text{LOR}}(\alpha, \beta)$ should be preferred as analytical function for predicting the large-signal behavior of ferroelectric materials. Nevertheless, when we are also interested in generalized Preisach hysteresis models, $\mu_{\text{DAT}}(\alpha, \beta)$ will be currently the only known analytical function providing uniqueness, accuracy as well as flexibility of the weighting distribution and, consequently, of the Preisach hysteresis operator [101].

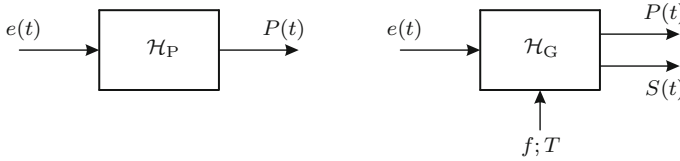


Fig. 6.15 Inputs as well as outputs of classical Preisach hysteresis operator \mathcal{H}_P and generalized Preisach hysteresis operator \mathcal{H}_G ; $e(t)$ stands for normalized electric field intensity

6.6 Generalized Preisach Hysteresis Model

The classical Preisach hysteresis operator \mathcal{H}_P is only suitable to a limited extent for predicting hysteretic behavior of ferroelectric materials. For this reason, it is important to improve and modify \mathcal{H}_P , which leads to so-called generalized Preisach hysteresis models with the underlying operator \mathcal{H}_G . Several types of model generalizations were developed as well as implemented by Wolf and colleagues (e.g., [78, 104, 106]). Principally, those generalizations can be divided into three categories. The first category aims at increasing flexibility to consider reversible parts (Sect. 6.6.1) and asymmetric behavior (Sect. 6.6.2), while the second one deals with the mechanical large-signal behavior of ferroelectric materials (Sect. 6.6.3). The third category addresses extensions of \mathcal{H}_P to take into account both the rate-dependent behavior of the materials (Sect. 6.6.4) and the impact of applied uniaxial mechanical stresses (Sect. 6.6.5). In contrast to \mathcal{H}_P , the resulting generalized Preisach hysteresis operator \mathcal{H}_G features an additional output $S(t)$ for mechanical strains of ferroelectric materials (see Fig. 6.15). Moreover, \mathcal{H}_G is equipped with two further inputs concerning frequency f of the electrical excitation signal and mechanical stress T within the material. Below, the model generalizations are studied separately.

6.6.1 Reversible Parts

Weighting distributions $\mu_{\mathcal{H}}(\alpha, \beta)$ of the Preisach hysteresis operator \mathcal{H}_P consist in general of finite values. As a result, the gradient $\partial y(k) / \partial x(k)$ of discrete-time model output $y(k) = \mathcal{H}_P[x](k)$ with respect to discrete-time input $x(k)$ is always zero at the reversal points. This characteristic can be seen in Figs. 6.12 and 6.13. However, measured output quantities of ferroelectric materials exhibit certain saturation trends. For instance, measured hysteresis curves $P(E)$ for the electric polarization show the property $\partial P / \partial E|_{E=E_{\text{sat}}} \neq 0$. Mainly, this is due to reversible effects (intrinsic effects; see Sect. 3.4.1) taking place within ferroelectric materials. Based on the assumption that there also occurs saturation for such effects, they are oftentimes modeled through an appropriate arctangent functions. Sutor et al. [89] suggest an additional linear part c , which was primarily applied for describing the large-signal behavior of ferromagnetic materials. Therewith, the entire discrete-time model out-

put $y(k)$ becomes

$$y(k) = \mathcal{H}_P[x](k) + y_{\text{rev}}(x(k)) \text{ ,} \quad (6.22)$$

whereas the added reversible part y_{rev} is given by

$$y_{\text{rev}}(x(k)) = a \cdot \arctan(b \cdot x(k)) + c \cdot x(k) \text{ .} \quad (6.23)$$

Let us utilize a slightly different approach for ferroelectric materials. Reversible parts are again considered by means of an arctangent function. Instead of adding those parts to $y(k)$, we incorporate them directly in the weighting distribution $\mu_{\mathcal{H}}(\alpha, \beta)$. This will offer particular advantages when the generalized Preisach hysteresis operator \mathcal{H}_G has to be inverted (see Sect. 6.8). With a view to explaining the approach, it is helpful to take a closer look at the weighting distribution in the Preisach plane \mathcal{P} (see Fig. 6.16a). The incorporation of reversible parts is performed through weights on the axis $\delta = \alpha = \beta$ [64, 69]. Due to the properties of the elementary switching operators $\gamma_{\alpha\beta}$, these weights will be cumulatively summed up if the operator input $x(k)$ increases. On the other hand, in case of a decreasing input, the weights are cumulatively subtracted. These cumulative operations represent the incorporated reversible part $y_{\text{rev}}(k)$ of the modified Preisach hysteresis model. Hence, $y_{\text{rev}}(k)$ reads as

$$y_{\text{rev}}(k) = \int_{\delta_1}^{\delta_2} \mu_{\mathcal{H}}(\delta, \delta) \gamma_{\delta\delta}[x](k) \, d\delta \quad (6.24)$$

in analytical formulation. Here, δ_1 and δ_2 stand for the lower and upper integration limit, respectively. While δ_1 is -0.5 for increasing inputs, decreasing inputs yield $\delta_1 = 0.5$ (see Fig. 6.16b). Since (6.24) contains an integration, we have to differentiate (6.23) with respect to $x = \delta$, which leads to the reversible parts $r(\delta)$ in the Preisach plane

$$r(\delta) = r(x) = \frac{ab}{M[1 + b^2(x + h_1/2)^2]} + c \text{ .} \quad (6.25)$$

Note that $r(\delta)$ exclusively defines the weights along the axis $\alpha = \beta$, e.g., $\mu_{\mathcal{H}}(-0.3, -0.3) = r(-0.3)$. The function is composed of the dimensionless parameters a , b , c , and h_1 . By conducting a normalization to M in (6.25), the resulting output $y_{\text{rev}}(k)$ is largely independent of the utilized spatial discretization.

As indicated in Fig. 6.16a, a , b , c , and h_1 modify $r(\delta)$ in a distinct way, respectively. The parameter a scales the maximum and b its extension. Through c , we can add an offset on the axis $\alpha = \beta$ causing a linear part in the model output. In accordance with the DAT function $\mu_{\text{DAT}}(\alpha, \beta)$, h_1 shifts the maximum of $r(\delta)$ along the axis $\alpha = \beta$. The reason for introducing the parameter h_1 will be discussed in

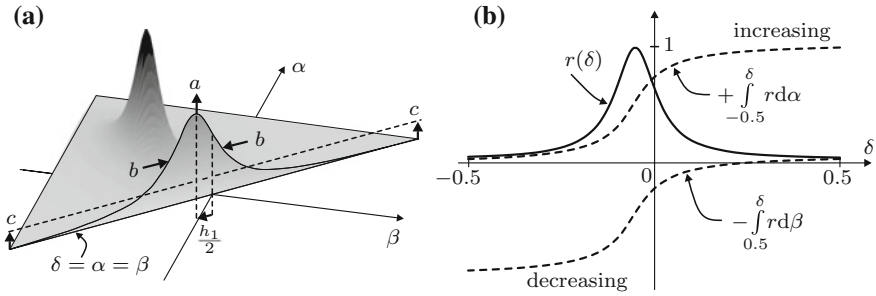


Fig. 6.16 **a** Weighting distribution $\mu_{\text{DAT}}(\alpha, \beta)$ and reversible parts $r(\delta)$ in Preisach plane \mathcal{P} ; arrows indicate increasing parameter values; **b** normalized version of function $r(\delta)$ and its integration for increasing as well as decreasing model inputs, respectively; parameter values for $r(\delta)$ (see (6.25)): $a = 0.4$, $b = 15$, $c = 0$ and $h_1 = 0.1$ [101]

Sect. 6.6.2. On account of the fact that c can usually be omitted in (6.25), $r(\delta)$ and, consequently, $y_{\text{rev}}(k)$ are described by the two additional parameters a and b [101]. Considering also the DAT function, the analytical weighting distribution for modeling the large-signal behavior as well as reversible parts comprises eight independent parameters, i.e.,

$$\mathbf{p} = [a, b, B, \eta, h_1, h_2, \sigma_1, \sigma_2]^t. \quad (6.26)$$

At this point, it should be mentioned that the reversible parts have already been applied in Figs. 6.10 and 6.14 to obtain the results by means of analytical weighting distributions. Table 6.1 additionally contains the parameters a and b for $\mu_{\text{DAT}}(\alpha, \beta)$, $\mu_{\text{GAUSS}}(\alpha, \beta)$ as well as $\mu_{\text{LOR}}(\alpha, \beta)$.

6.6.2 Asymmetric Behavior

According to the assumptions in Sect. 6.5 (see Assumptions 2 and 3 on p. 214), the switching behavior of unloaded domains inside ferroelectric materials is symmetrical to the applied electric field intensity. However, especially ferroelectrically hard materials often exhibit asymmetric hysteresis curves. This fact can be mainly ascribed to a restricted mobility of domain walls (see also Sect. 3.6.2). Such pinned or clamped domain walls originate from defects and imperfections in the crystal lattice [18]. As a result, a bias field intensity may arise which has to be compensated by the applied electric field in order to initiate domain switching processes.

The bias field intensity E_{bias} (normalized value e_{bias}) can be considered within the generalized Preisach hysteresis model by shifting an originally symmetric weighting distribution $\mu_{\mathcal{H}}(\alpha, \beta)$ along the axis $\alpha = \beta$. For this purpose, we introduced in the DAT function the parameter h_1 that shifts the maximum of $\mu_{\text{DAT}}(\alpha, \beta)$ (see Fig. 6.11b) as well as of the reversible parts $r(\delta)$ (see Fig. 6.16a) in the Preisach plane \mathcal{P} .

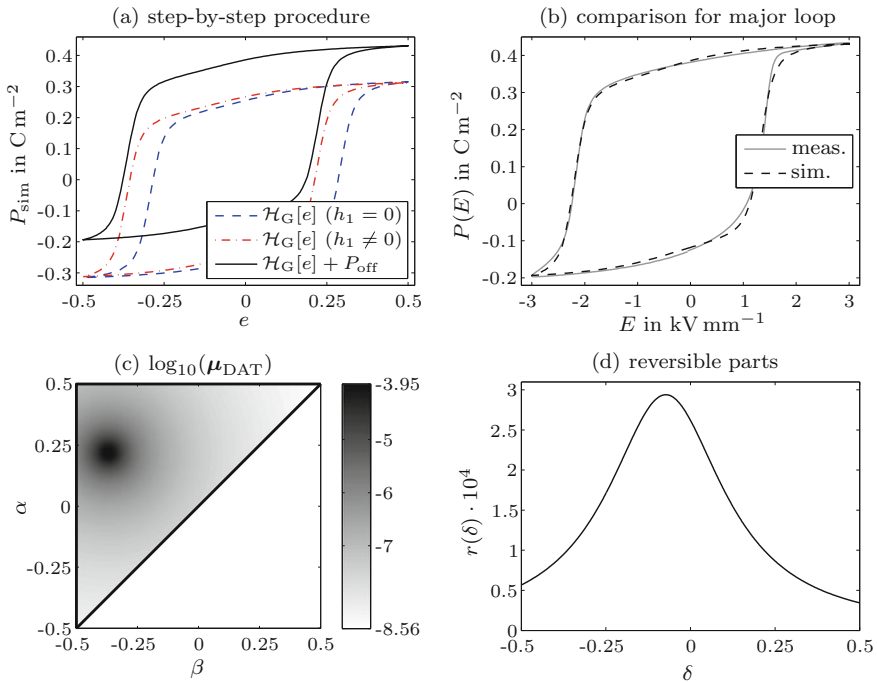


Fig. 6.17 **a** Step-by-step procedure to simulate asymmetric hysteresis curves through Preisach hysteresis modeling; **b** comparison of measurements and simulations for a major loop of $P(E)$; **c** spatially discretized weighting distribution μ_{DAT} for $M = 800$; **d** reversible parts $r(\delta)$ according to (6.25); piezoceramic disk (diameter 10.0 mm; thickness 2.0 mm; material Pz26)

Apart from the asymmetric shape of a hysteresis curve $y(x)$ with respect to the applied input x , the output y itself can be asymmetric in addition leading to $\max(y) \neq -\min(y)$ (see, e.g., Fig. 6.17b). But if every elementary switching operator $\gamma_{\alpha\beta}$ of the Preisach hysteresis model takes the output value -1 (i.e., $\mathcal{P} = \mathcal{P}^-$) or $+1$ (i.e., $\mathcal{P} = \mathcal{P}^+$), y will be symmetrical, which means $\max(y) = -\min(y)$. The Preisach hysteresis operator is, thus, not sufficient to model asymmetric outputs ranging from $\min(y)$ to $\max(y)$. In case of asymmetric hysteresis curves $P(E)$ for ferroelectric materials, we have to add an appropriate offset P_{off} to the electric polarization that is determined through measurements [101].

To present the applicability of the generalized Preisach hysteresis operator \mathcal{H}_G , let us investigate a piezoceramic disk (diameter 10.0 mm; thickness 2.0 mm) made of the ferroelectrically hard material Pz26. Figure 6.17a illustrates the step-by-step procedure to obtain an asymmetric hysteresis curve through Preisach modeling. As the comparison of measurements and simulations for a major loop in Fig. 6.17b reveals, \mathcal{H}_G yields reliable results. The asymmetric behavior with respect to E is well described by the function parameter h_1 . Figure 6.17c and d depict the obtained weighting distribution μ_{DAT} and $r(\delta)$ denoting reversible parts on the axis $\alpha = \beta$.

6.6.3 Mechanical Deformations

Until now, we have concentrated on Preisach modeling for the electrical behavior (i.e., $P(E)$) of ferroelectric materials. In many practical applications (e.g., high-precision positioning systems) of those materials, it is, however, of utmost importance to consider their mechanical behavior in addition. With a view to simulating the mechanical large-signal behavior of piezoceramic materials, let us briefly repeat relevant physical processes on the atomistic as well as mesoscopic scale (see Sect. 3.6.2). The spontaneous polarization \mathbf{p}_n of a unit cell points in direction of its largest geometric dimension. Because each \mathbf{p}_n is almost perfectly aligned in parallel to the applied electric field E in the saturation state of the piezoceramic material, the macroscopic mechanical deformation also reaches the highest value in direction of E . During changes from positive to negative saturation (and vice versa), several domains switch to the ferroelastic intermediate stage at first, which causes a negative mechanical deformation of the material [14]. When $|E|$ exceeds thereupon the coercive field intensity $|E_c^\pm|$, the domains will be aligned again in direction of E , i.e., 180° with respect to their original orientation. The macroscopic polarization state of the piezoceramic material, thus, changes its sign, while the mechanical deformations are equal for positive and negative saturation. In other words, electric polarization and mechanical deformation differ significantly in terms of the underlying large-signal behavior.

We can reasonably describe the mechanical deformation $S(E)$ of ferroelectric actuators through a generalized Preisach hysteresis model (e.g., [32, 38]) if they operate in unipolar and semi-bipolar working areas (i.e., $E > E_c^-$). The function parameter c (see (6.25)) within the presented operator \mathcal{H}_G provides shifts of simulated deformations in vertical direction, which are possibly existing in these working areas. On the contrary, butterfly curves resulting for bipolar working area demand further extensions of the Preisach hysteresis operator. For this purpose, one can find two different approaches in literature:

- Kadota and Morita [47] introduced a tristable hysteron to model the ferroelastic intermediate stage of domains. As the name indicates, this hysteron features three stable states, i.e., -1 , 0 as well as $+1$. Since the approach requires a four-dimensional weighting distribution, complexity of the underlying Preisach hysteresis models considerably increases.
- Due to the fact that mechanical deformations of ferroelectric materials are equal for positive and negative saturation, we may rectify the output $y = \mathcal{H}_p[x]$ of the classical hysteresis operator (e.g., [36]).

Concerning practical applications of Preisach hysteresis models for ferroelectric materials, the second approach should be preferred. That is why we will concentrate exclusively on this approach for describing mechanical deformations. Hegewald [36] conducted rectification of the operator output guided by the approximation $S \propto P^2$. To model the large-signal behavior of mechanical deformations by means of the Preisach hysteresis operator, he utilized the same weighting distribution as for the

electric polarization, i.e., $\mu_{\text{HEG}}(\alpha, \beta)$. Under certain circumstances, the approximation $S \propto P^2$ yields satisfactory results, but in general, the deviations between simulations and measurements of $S(E)$ are rather high. The following findings can be deduced for computing mechanical large-signal behavior through Preisach hysteresis operators [101]:

- For several ferroelectric materials, the rectified electric polarization significantly differs from the macroscopic mechanical deformation. It is, therefore, necessary to identify individual weighting distributions for the polarization and the deformation, which are parameterized by the vectors \mathbf{p}_P and \mathbf{p}_S , respectively.
- As mentioned above, domain switching processes by 180° within ferroelectric materials alter the sign of the electric polarization but do not modify their mechanical deformation. Thus, it seems reasonable to rectify the operator output y through computing its absolute value instead of squaring. In doing so, the function parameters (e.g., B) of $\mu_{\text{DAT}}(\alpha, \beta)$ influence hysteresis curves for polarization and deformation in a similar manner (see p. 219).
- To account for asymmetric large-signal behavior of mechanical deformations, we have to extend the generalized Preisach hysteresis operator \mathcal{H}_G .

An appropriate method to consider these findings for modeling mechanical deformations of ferroelectric materials is given by (time step k ; normalized electric field intensity e)

$$S(k) = \{c_1 + |\mathcal{H}_G[e](k) + c_2| + c_3(e - 0.5)\} \cdot 100\% . \quad (6.27)$$

Hence, the three parameters c_1 , c_2 and c_3 are required in addition. Overall, Preisach hysteresis modeling for mechanical deformations comprises 11 independent parameters, namely

$$\mathbf{p}_S = [a, b, B, c_1, c_2, c_3, \eta, h_1, h_2, \sigma_1, \sigma_2]^t . \quad (6.28)$$

Five parameters refer to the DAT function $\mu_{\text{DAT}}(\alpha, \beta)$ and two parameters to reversible parts in the large-signal behavior.

In order to demonstrate this modeling approach, let us investigate a ferroelectrically hard piezoceramic disk (diameter 10.0 mm; thickness 2.0 mm; material Pz26), which usually features an asymmetric large-signal behavior for both polarization and deformation. The mechanical deformations of the piezoceramic disk were acquired with a linear variable differential transformer (abbr. LVDT [99]) that was optimized for measuring small displacements.⁹ Figure 6.18a shows the basic steps in simulating a butterfly curve according to (6.27). Asymmetric behavior is incorporated in the generalized Preisach hysteresis operator \mathcal{H}_G through the parameter h_1 . Before computing the absolute value, we add an offset c_2 to the mechanical deformation. Therewith, one can model differences in maximum values of S , i.e., $S_{\text{max}}^- \neq S_{\text{max}}^+$. Finally, the linear equation $c_1 + c_3(e - 0.5)$ is added to consider different slope stiffnesses as well as

⁹The LVDT was applied for all measurements of S in this chapter.

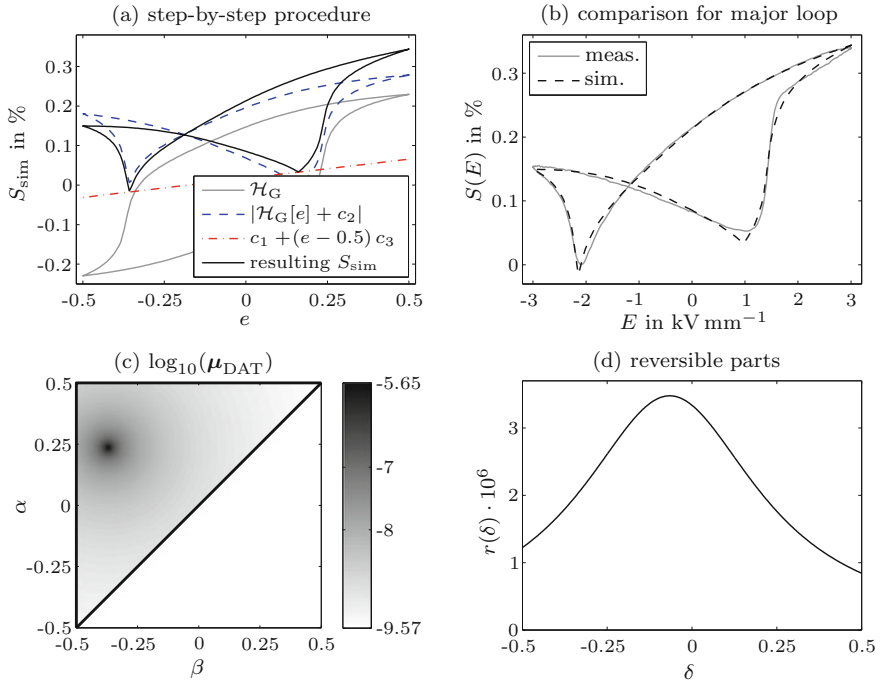


Fig. 6.18 **a** Step-by-step procedure to simulate mechanical deformations of ferroelectric materials through Preisach hysteresis modeling; **b** comparison of measured and simulated major loop (butterfly curve) $S(E)$; **c** spatially discretized weighting distribution μ_{DAT} for $M = 800$; **d** reversible parts $r(\delta)$ according to (6.25); piezoceramic disk (diameter 10.0 mm; thickness 2.0 mm; material Pz26)

the circumstance $S_{\text{min}}^- \neq S_{\text{min}}^+$. To identify the parameter vector \mathbf{p}_S , simulations have to be adjusted so that they match measurements best possible.

As Fig. 6.18b reveals, measured and simulated mechanical deformations of the piezoceramic disk coincide very well. It can be stated that the presented Preisach hysteresis model is ideally suited for predicting mechanical deformations of ferroelectric materials. Figure 6.18c and d depict the resulting weighting distribution μ_{DAT} and the reversible parts $r(\delta)$, respectively.

6.6.4 Rate-Dependent Behavior

Even though a piezoceramic material is macroscopically excited in a uniform manner, domain switching processes inside the material do not take place simultaneously. Depending on the alteration rate of the excitation signal, this may remarkably influence macroscopic quantities (e.g., mechanical strain) [46]. The macroscopic

rate-dependent behavior of piezoceramic materials originates from their inhomogeneous inner structure, which yields locally different electric field intensities as well as mechanical stresses for the domains. In a first approximation, we can assume that a single domain switches quickly after its individual switching energy is locally provided [72]. Such switching processes and reversible as well as irreversible ion displacements alter the spatial distribution of both electric field intensity and mechanical stress inside the piezoceramic material. As a result, a large number of domains do not switch immediately but depending on previous switching processes of neighboring domains and ion displacements within them. From the macroscopic point of view, this leads to the creep behavior of electric polarization and mechanical strain (e.g., [109]).

Outputs $y(t)$ of the classical Preisach hysteresis operator \mathcal{H}_P solely depend on temporal succession of the input $x(t)$ (see \mathbb{I} and \mathbb{J} in Fig. 6.7). Therefore, the alteration rate of $x(t)$ with respect to time (i.e., $\partial x(t)/\partial t$) does not affect $y(t)$. Since macroscopic electric polarizations and macroscopic mechanical strains of ferroelectric materials exhibit such a dependence, one has to extend \mathcal{H}_P , which results in so-called *dynamic* or *rate-dependent Preisach hysteresis models*. Mayergoyz [63] suggests a dynamic Preisach hysteresis model that is based on a varying weighting distribution $\mu_{\mathcal{H}}(\alpha, \beta)$ according to the partial time derivative of $y(t)$. Viswamurthy et al. [95] applied this approach to describe dynamic hysteresis of piezoceramic stack actuators. In several other research works (e.g., [67, 85]), the partial time derivative of $x(t)$ is used instead for modifying $\mu_{\mathcal{H}}(\alpha, \beta)$. As alternative to changing the weighting distribution, Bertotti [11] introduced time-dependent elementary switching operators for dynamic Preisach modeling. In contrast to common relay operators (see Fig. 6.3a), these operators can take continuous values between -1 and 1 . Actually, their practical implementation is rather complicated and, thus, the operator output cannot be calculated efficiently. Füzi [31] developed a dynamic Preisach hysteresis model through applying an appropriate time lag for $x(t)$. Thereby, the resulting hysteresis operator loses its physical meaning, which poses a significant problem regarding generalization.

A different class of dynamic Preisach hysteresis models for ferroelectric materials is based on so-called *creep operators*. Such an operator is connected in series to the output of the classical Preisach hysteresis operator, i.e., $y(t) = \mathcal{H}_P[x](t)$ represents the creep operator's input. Hegewald [36] as well as Reiländer [76] utilized a rheological modeling approach to achieve appropriate creep operators for ferroelectric materials. This phenomenological approach is commonly named *Kelvin–Voigt model*. A single elementary creep operator can be understood as a parallel connection of one spring and one damper element (cf. Fig. 5.20 on p. 168). By means of individually weighting several of those elementary creep operators, we are able to describe the creep behavior of ferroelectric materials in a reliable way (e.g., [36]). Although elementary creep operators can be efficiently implemented, the amount of necessary parameters for dynamic Preisach hysteresis models increases remarkably. Consequently, the uniqueness of the parameters might get lost during their identification.

With a view to practical applications of dynamic Preisach hysteresis models for ferroelectric actuators, we are primarily interested in a modeling approach that requires only a few additional parameters. Because ferroelectric actuators operate in most applications in a limited frequency range, one may simply extend the classical Preisach hysteresis operator \mathcal{H}_P . As presented in [67, 85], let us also alter the weighting distribution. For this purpose, a special procedure for piezoceramic actuators has been developed at the Chair of Sensor Technology (Friedrich-Alexander-University Erlangen-Nuremberg), which is based on the weighting distribution $\mu_{\text{DAT}}(\alpha, \beta)$. In short, the analytical function defining $\mu_{\text{DAT}}(\alpha, \beta)$ is modified with respect to the frequency f of the excitation signal [78, 101, 103, 104]. This leads to a dynamic weighting distribution $\mu_{\text{DAT}}(\alpha, \beta, f)$ and, therefore, we obtain a dynamic Preisach hysteresis model.

In the following, the developed procedure is illustrated on the example of a ferroelectrically soft piezoceramic disk (diameter 10.0 mm; thickness 2.0 mm; material Pz27). Figure 6.19a shows resulting hysteresis curves for the acquired electric polarization $P_{\text{meas}}(E, f)$ with respect to the excitation frequency f . Thereby, the electrical excitation was chosen so that the hysteresis curves contain major loops as well as first-order reversal curves for selected excitation frequencies. The frequencies range from 0.01 to 5 Hz and are almost logarithmically distributed in this range. While the electric polarization P_{sat}^{\pm} in the saturation state and the remanent polarization P_r^{\pm} stay nearly constant, the coercive field intensity E_c^{\pm} exhibits a significant dependence on f . If f increases, $|E_c^{\pm}|$ will also increase which, thus, widens the hysteresis curve.

To incorporate the measured behavior of the investigated piezoceramic material in our Preisach hysteresis model, let us take a look at Fig. 6.12. The parameter study reveals that the parameter h_2 of the DAT function has a similar effect on hysteresis curves as f . For this purpose, it makes sense to exclusively alter h_2 with respect to f in order to obtain a dynamic Preisach hysteresis model. It is recommended to proceed as follows: (i) As a first step, one should identify the entire parameter set of the Preisach hysteresis model at one excitation frequency; (ii) subsequently, the dependence of h_2 on f should be evaluated, i.e., the remaining parameters (e.g., B) are not modified. In case of the investigated piezoceramic disk, the entire parameter set \mathbf{p}_p for the electric polarization was identified through an appropriate adjustment of simulations to measurements at $f = 0.1$ Hz. Note that for the other excitation frequencies, h_2 was simply changed within \mathbf{p}_p . As the simulated hysteresis curves of the electric polarization $P_{\text{sim}}(E, f)$ in Fig. 6.19c point out, we can describe the frequency dependent behavior of the piezoceramic disk very well with the suggested dynamic Preisach hysteresis model. This does not only refer to the major loops but also to the minor loops.

Figure 6.19e depicts the identified values for h_2 with respect to f for the electric polarization of the investigated disk, i.e., $h_{2,p}(f)$. These values can serve as data points of a smoothing function $\psi_{\text{smooth}}(f)$ for $h_{2,p}(f)$. Due to the progression of the data points, logarithmic as well as exponential functions are appropriate smoothing functions [101]. Here, let us utilize a special exponential function, which is given by

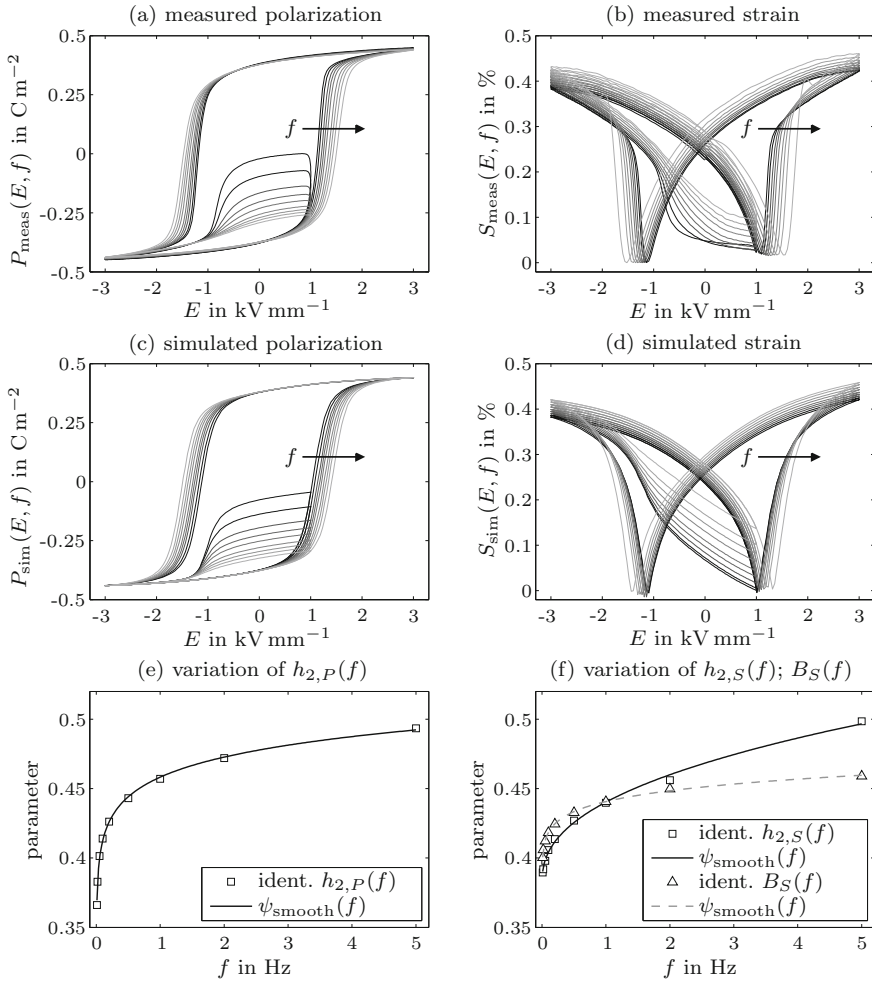


Fig. 6.19 **a** and **b** Measured electric polarization $P_{\text{meas}}(E, f)$ and mechanical strain $S_{\text{meas}}(E, f)$ with respect to excitation frequency f ; **c** and **d** simulated curves $P_{\text{sim}}(E, f)$ and $S_{\text{sim}}(E, f)$ through Preisach hysteresis modeling; **e** and **f** resulting parameter values as well as smoothing function $\psi_{\text{smooth}}(f)$ according to (6.29); excitation frequencies $f \in \{0.01, 0.02, 0.05, 0.1, 0.5, 1, 2, 5\}$ Hz; piezoceramic disk (diameter 10.0 mm; thickness 2.0 mm; material Pz27)

$$\psi_{\text{smooth}}(f) = \varsigma_1 + \varsigma_2 \cdot f^{\varsigma_3} \tag{6.29}$$

with the function parameters ς_1 , ς_2 , and ς_3 . Hence, one is able to estimate values $h_{2,P}(f)$ for excitation frequencies even if measured data for that frequencies are not available. Thereby, two additional parameters are required. Table 6.2 contains the resulting parameters of the smoothing function $\psi_{\text{smooth}}(f)$ for $h_{2,P}(f)$.

Table 6.2 Parameters ς_i of smoothing function $\psi_{\text{smooth}}(f)$ in (6.29) for dynamic Preisach hysteresis model

		ς_1	ς_2	ς_3
Polarization	$h_{2,P}(f)$	-0.2121	0.6703	0.0308
Strain	$h_{2,S}(f)$	0.3819	0.0583	0.4206
	$B_S(f)$	0.3315	0.1091	0.0995

Now, we concentrate on the dynamic large-signal behavior of the mechanical strain. Figure 6.19b depicts resulting hysteresis curves for acquired mechanical strains $S_{\text{meas}}(E, f)$ of the investigated piezoceramic disk with respect to the excitation frequency f . The minima S_{min}^{\pm} remain nearly constant, while the maxima S_{max}^{\pm} strongly depend on f . That is the reason why apart from h_2 , the parameter B of the DAT function has to be modified. However, in order to predict the dynamic large-signal behavior of the mechanical strain by means of a dynamic Preisach hysteresis model, one can perform the same steps as for the electric polarization. Again, the entire parameter set \mathbf{p}_S should be identified for a certain excitation frequency f (here 0.1 Hz) and after that the dependence of h_2 as well as of B on f should be evaluated. As the comparison of measurements $S_{\text{meas}}(E, f)$ and simulations $S_{\text{sim}}(E, f)$ (see Fig. 6.19d) indicates, the presented dynamic Preisach hysteresis model is also applicable for the mechanical strain. Figure 6.19f shows the identified values for $h_{2,S}(f)$ and $B_S(f)$ with respect to f as well as the smoothing functions $\psi_{\text{smooth}}(f)$ for both parameters according to (6.29). The underlying parameters ς_1 , ς_2 , and ς_3 are listed in Table 6.2. In summary, dynamic Preisach hysteresis modeling for the large-signal behavior of mechanical strains requires four additional parameters.

6.6.5 Uniaxial Mechanical Stresses

In various practical applications, ferroelectric actuators are mechanically clamped or loaded causing a certain mechanical prestress within the ferroelectric material. For instance, piezoelectric stack actuators have to be mechanically prestressed in order to prevent damage during operation (see Sect. 10.1). Mechanical stresses arising within a ferroelectric material can, however, alter its electrical as well as mechanical behavior significantly [106, 109, 110]. To demonstrate this fact, we consider the large-signal behavior of a ferroelectrically soft piezoceramic disk (diameter 10.0 mm; thickness 2.0 mm; material Pz27). Figures 6.20a and 6.21a depict the acquired electric polarization $P_{\text{meas}}(E, T)$ and mechanical strain $S_{\text{meas}}(E, T)$ of the disk for varying uniaxial mechanical prestresses T , respectively. The mechanical load was applied in thickness directions (3-direction) of the disk through a tension-compression testing machine. It can be clearly seen that both the electrical and mechanical behavior strongly depend on the mechanical prestress inside the disk. The reason for this lies in switching processes of domains and in the internal structure of piezoceramic mate-

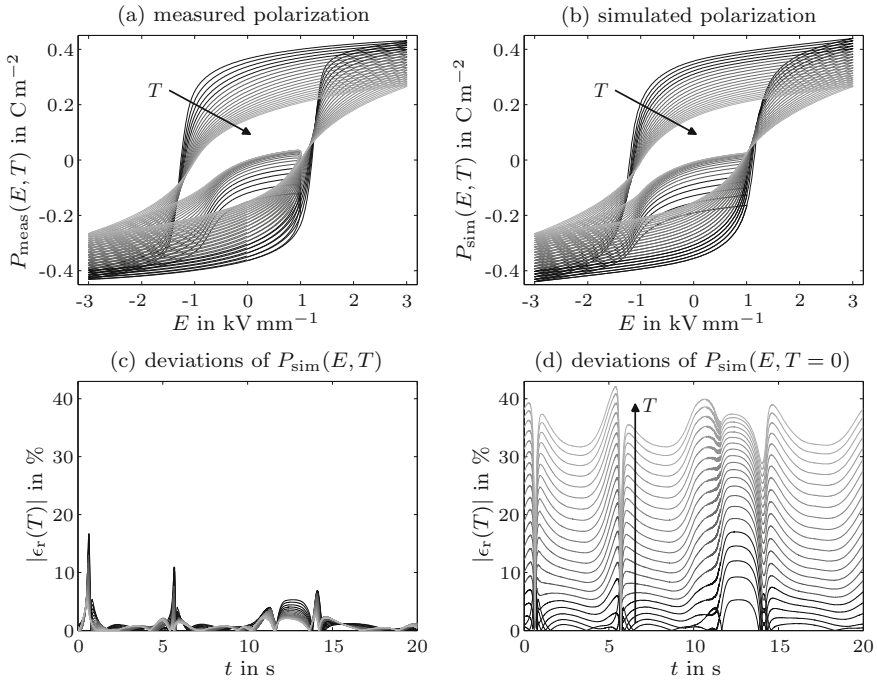


Fig. 6.20 **a** and **b** Measured and simulated electric polarization $P(E, T)$ with respect to applied mechanical prestress T ; collected normalized relative deviations $|\epsilon_r(T)|$ (magnitude) in case of **c** considered prestress during Preisach hysteresis modeling and **d** without consideration of T ; applied mechanical prestress $T = [0; 100]$ MPa in steps of 5 MPa; piezoceramic disk (diameter 10.0 mm; thickness 2.0 mm; material Pz27)

rials. The polarization direction (spontaneous polarization) within the units cells is preferably aligned in parallel to the applied electric field E . Against that due to the connection of polarization direction and largest geometric dimension of the unit cells, they are preferably aligned orthogonal to the applied mechanical stress T . Consequently, macroscopic polarizations as well as mechanical strains will be decreased if the directions of E and T coincide, which is the case for the investigated piezoceramic disk. The greater T , the more domains will stay in the ferroelastic intermediate stage during poling and can no longer be aligned in the direction of E [14]. Hence, coercive field intensity $|E_c^\pm|$, remanent polarization $|P_r^\pm|$, polarization $|P_{\text{sat}}^\pm|$ in the saturation state as well as the maximum mechanical strain S_{max}^\pm of the piezoceramic material are reduced which yield smaller hysteresis curves (see Figs. 6.20a and 6.21a).

To utilize Preisach hysteresis modeling for the large-signal behavior of mechanically prestressed ferroelectric materials, one may identify the entire parameter set of the generalized model for the current situation. That will be, however, only possible if the mechanical prestress remains constant during operation. In case of time-varying mechanical loads, it makes sense to consider the resulting mechanical prestress as

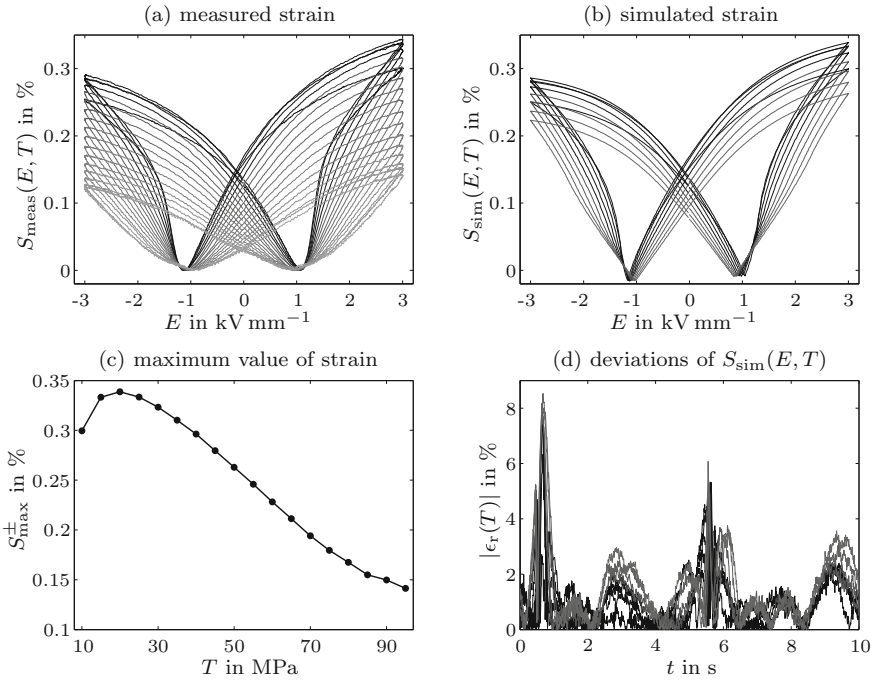


Fig. 6.21 **a** and **b** Measured and simulated mechanical strain $S(E, T)$ with respect to applied mechanical prestress T ; **c** maximum value of the mechanical strain S_{max}^{\pm} versus prestress; **d** collected normalized relative deviations $|\epsilon_r(T)|$ (magnitude) in case of considered prestress during Preisach hysteresis modeling; applied mechanical prestress for measurements $T = [10; 95]$ MPa and simulations $T = [10; 50]$ MPa in steps of 5 MPa, respectively; piezoceramic disk (diameter 10.0 mm; thickness 2.0 mm; material Pz27)

additional input of a generalized Preisach hysteresis model \mathcal{H}_G (see Fig. 6.15). For ferromagnetic materials, there can be found several publications concerning the incorporation of mechanical prestresses in Preisach hysteresis models. Some of the available methods are briefly described below. Adly et al. [1] suggest an approach that is based on the superposition of two Preisach hysteresis operators. While the magnetic field intensity serves as input for the first hysteresis operator, the mechanical stress is the input for the second one. Since the weighting distribution of the first hysteresis operator depends on stress and those of the second one on magnetic field intensity, a mutual coupling of magnetic and mechanical quantities is achieved. The particular problem here is the identification of appropriate weighting distributions. Bergqvist and Engdahl [10] use a single Preisach hysteresis operator with one input, which is given by combining magnetic field intensity and mechanical stress. Because of the fact that each elementary switching operator $\gamma_{\alpha\beta}$ requires an individual input resulting from this combination, model complexity increases extensively. Enhancements of both methods are mentioned in, e.g., [19, 60]. In contrast to ferromagnetic

materials, the number of publications dealing with Preisach hysteresis models for ferroelectric materials under additional consideration of mechanical prestress is currently very low. Hughes and Wen [41] early recognized a need for Preisach hysteresis models with two separate inputs for electrical excitation and mechanical prestress but did not pursue this path toward a generalized approach. Freeman and Joshi [30] introduced a hysteron depending on the applied mechanical prestress. However, they only presented simulation results of the rate-independent approach and did not conduct verifications through measurements on test samples.

Due to the lack of appropriate Preisach hysteresis models enabling consideration of mechanical prestress within ferroelectric materials, an appropriate generalized Preisach hysteresis model was developed at the Chair of Sensor Technology (Friedrich-Alexander-University Erlangen-Nuremberg) [101, 105, 106]. Let us explain the underlying idea by the aforementioned large-signal behavior of the piezoceramic disk in case of uniaxial mechanical prestress. During acquisition of the electric polarization $P_{\text{meas}}(E, T)$, the mechanical prestress was increased starting from 0 to 100 MPa in steps of 5 MPa. The curves in Fig. 6.20a refer to the steady state, which means that mechanical creep processes taking place within a prestressed ferroelectric material had already decayed [101]. Similar to the procedure for the rate-dependent behavior of ferroelectric materials (see Sect. 6.6.4), one can modify the weighting distribution of a classical Preisach hysteresis model with respect to the applied mechanical load. Here, we introduce the weighting distribution $\mu_{\text{DAT}}(\alpha, \beta, T)$, which is, thus, also a function of the mechanical prestress T . As the comparison of $P_{\text{meas}}(E, T)$ in Fig. 6.20a and the parameter study in Fig. 6.12 reveals, the function parameters B , η and h_2 should be altered according to the applied mechanical load. This can be ascribed to the fact that $|P_{\text{sat}}^\pm|$, $|P_{\text{r}}^\pm|$, $|E_{\text{c}}^\pm|$ as well as the slope steepness nearby $|E_{\text{c}}^\pm|$ change through T . Figure 6.20b displays simulated electric polarizations $P_{\text{sim}}(E, T)$ for different values of T . The entire parameter set of the Preisach hysteresis operator was identified for the mechanically unloaded disk, i.e., $T = 0$. Note that in the loaded case (i.e., $T \neq 0$), we solely modified B , η as well as h_2 . Figure 6.22a–c contain the resulting parameters $B_P(T)$, $\eta_P(T)$ and $h_{2,P}(T)$ with respect to T . Because these parameters feature smooth progression, they can serve as data points of the smoothing function $\psi_{\text{smooth}}(T)$

$$\psi_{\text{smooth}}(T) = \varsigma_1 + \varsigma_2 e^{\varsigma_3 T / (1 \text{ MPa})} . \quad (6.30)$$

Consequently, the generalized Preisach hysteresis operator \mathcal{H}_G comprises nine additional function parameters. For the investigated piezoceramic disk, these function parameters are listed in Table 6.3. Finally, the relative deviation $\epsilon_r(T)$ between measured and simulated electric polarization is shown for two cases. While in Fig. 6.20c, the applied mechanical prestress was considered in Preisach modeling, Fig. 6.20d depicts the results if we neglect this dependence. The comparison of the figures emphasizes once again the necessity of incorporating mechanical prestress in Preisach hysteresis models for ferroelectric materials.

As a next step, let us take a closer look at the mechanical behavior of the piezoceramic disk. In Fig. 6.21a, one can see the acquired butterfly curves $S_{\text{meas}}(E, T)$ in the

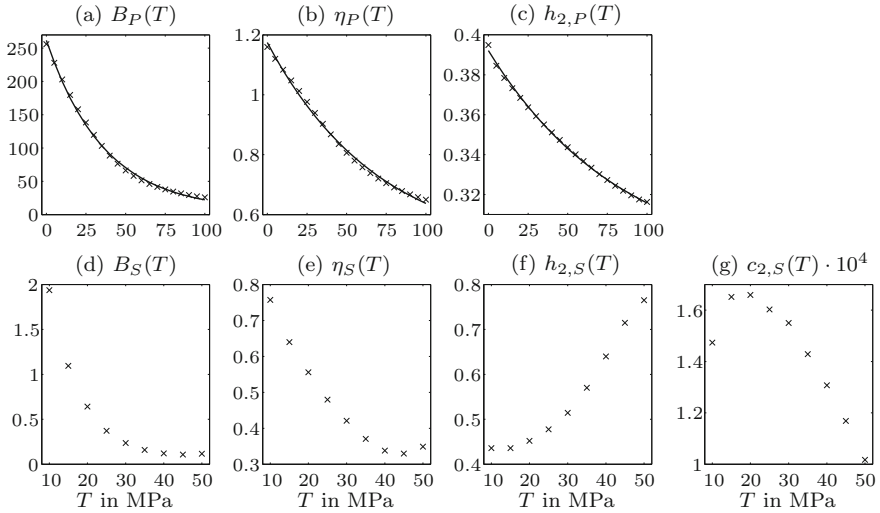


Fig. 6.22 Resulting parameter values **a–c** for electric polarization P (see Fig. 6.20) and **d–g** for mechanical strain S (see Fig. 6.21) with respect to applied mechanical prestress T , respectively; **a–c** contain smoothing functions $\psi_{\text{smooth}}(T)$ according to (6.30)

Table 6.3 Parameters c_i of smoothing function $\psi_{\text{smooth}}(T)$ in (6.30) to consider uniaxial mechanical prestress T in generalized Preisach hysteresis model \mathcal{H}_G

	ς_1	ς_2	ς_3
$B_P(T)$	5.7139	255.8991	−0.0275
$\eta_P(T)$	0.4657	0.7089	−0.0142
$h_{2,P}(T)$	0.2819	0.1102	−0.0118

steady state for different mechanical prestresses, which range from 10 to 95 MPa (step size 5 MPa). It is interesting to note that the maximum mechanical strains S_{max}^{\pm} of the piezoceramic disk slightly increase for small values of T (see Fig. 6.21c). This is mainly attributable to the increased mobility of domains within piezoceramic materials in the ferroelastic intermediate stage [101]. However, a further increase of the mechanical load strongly reduces S_{max}^{\pm} . To simulate the mechanical strain of the disk by means of Preisach hysteresis modeling, we modify the weighting distribution again with respect to the applied mechanical load, which leads to $\mu_{\text{DAT}}(\alpha, \beta, T)$. In contrast to $P_{\text{meas}}(E, T)$, parameter studies indicate that adjusting B , η , and h_2 is not sufficient to describe $S_{\text{meas}}(E, T)$ in a reliable way. The parameter c_2 (see (6.27)) has also to be varied with respect to the applied prestress. Such as for the electric polarization, the entire parameter set of the Preisach hysteresis operator was identified for the mechanically unloaded disk. In the loaded case, we only modified B , η , h_2 and c_2 . Figure 6.21b depicts the simulated butterfly curves $S_{\text{sim}}(E, T)$ for the piezoceramic disk in case of mechanical prestresses ranging from 10 MPa to 50 MPa.

The underlying parameters $B_S(T)$, $\eta_S(T)$, $h_{2,S}(T)$ as well as $c_{2,S}(T)$ are depicted in Fig. 6.22d–g. Due to the fact that S_{\max}^{\pm} slightly increases at first, one has to utilize more complicated smoothing functions than for the electric polarization. Within a limited prestress range, it is, nevertheless, possible to conduct similar approximations as in (6.30). At the end, Fig. 6.21d displays normalized relative deviations $\epsilon_r(T)$ between measured and simulated mechanical strains of the piezoceramic disk for different mechanical prestresses. These deviations stay mostly far below 10%, which confirms once more the applicability of the presented Preisach modeling approach.

6.7 Parameter Identification for Preisach Modeling

Classical as well as generalized Preisach hysteresis modeling for ferroelectric materials requires several parameters that have to be identified. For the electric polarization P and mechanical strain S , we collect these parameters in the vectors (cf. (6.26) and (6.28))

$$\mathbf{p}_P = [a_P, b_P, B_P, \eta_P, h_{1,P}, h_{2,P}, \sigma_{1,P}, \sigma_{2,P}]^t \quad (6.31)$$

$$\mathbf{p}_S = [a_S, b_S, B_S, c_1, c_2, c_3, \eta_S, h_{1,S}, h_{2,S}, \sigma_{1,S}, \sigma_{2,S}]^t, \quad (6.32)$$

respectively. In Sect. 6.7.1, a identification strategy is presented allowing reliable simulations for the different working areas of ferroelectric actuators, i.e., bipolar, unipolar as well as semi-bipolar working areas. The underlying approach is then applied to a piezoceramic disk (Sect. 6.7.2), which is made of the ferroelectrically soft material PIC255.

6.7.1 Identification Strategy for Model Parameters

Just as in Chap. 5, the parameter identification represents an ill-posed inverse problem. The desired parameter vectors \mathbf{p}_P as well as \mathbf{p}_S result from comparisons of measurements and simulations, i.e., outputs of the Preisach hysteresis operator. Due to this fact, one has to acquire adequate electrical and mechanical quantities. Through iterative adjustments of the parameters, the deviations between simulations and measurements get reduced until a sufficiently good match is found. The success of the iterative adjustments mainly depends on two points: (i) The measurement signals utilized for identification and (ii) the initial guess $\mathbf{p}_{P,S}^{(0)}$ of the parameter vectors. For Preisach hysteresis modeling, it is recommended to apply measurement signals that are close to the excitation signals actually occurring in practical applications. In other words, we should select measurement signals with respect to the working area of the ferroelectric actuator. Because Preisach hysteresis operators demand inputs in

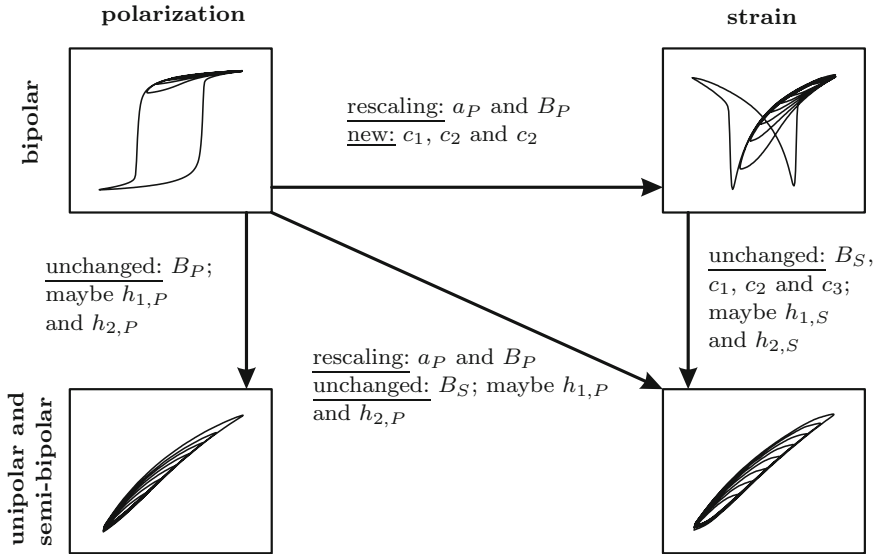


Fig. 6.23 Efficient strategy to find appropriate initial guess $\mathbf{p}_{p;s}^{(0)}$ and to reliably identify $\mathbf{p}_{p;s}$ for electric polarization and mechanical strain in different working areas of ferroelectric actuators [101]

the range $[-0.5, 0.5]$, the raw data has to be normalized to its maximum (see (6.7)). Such normalizations are necessary in each working area of the ferroelectric actuator.

The initial guess strongly affects convergence of the identification approach as well as its duration. To find $\mathbf{p}_{p;s}^{(0)}$ for the working areas, a specific procedure is indispensable. Figure 6.23 depicts an entire identification strategy that has proven to be effective for piezoceramic materials [101]. The presented strategy can be divided into two parts, which are discussed below. While the first part exclusively relates to bipolar working areas, the second one deals with unipolar as well as semi-bipolar working areas.

- Bipolar Working Area:** An appropriate initial guess $\mathbf{p}_p^{(0)}$ to predict P of piezoceramic materials in the bipolar working area (i.e., saturation and major loops) results from manually adjusting the parameters according to Fig. 6.12. After conducting iterative parameter adjustment on basis of an optimization approach (e.g., Levenberg–Marquardt algorithm), one obtains the solution \mathbf{p}_p^s . This vector serves as starting point for identifying the parameter vector \mathbf{p}_s^s , which yields reliable simulations for $S(E)$ in the bipolar working area, i.e., butterfly curves. In particular, with the exception of a_P and B_P , the components of \mathbf{p}_p^s can be used directly as initial guess for \mathbf{p}_s . Due to our definition of the Preisach hysteresis operator, we have to rescale a_p^s and B_p^s to achieve

Table 6.4 Resulting parameters (i.e., components of \mathbf{p}_P^s and \mathbf{p}_S^s) for Preisach hysteresis modeling of electric polarization P and mechanical strain S in different working areas of the piezoceramic disk; bold numbers indicate parameters excluded from identification

	B	η	h_1	h_2	σ_1	σ_2
P_{bipolar}	1868.5	1.275	0.011	0.450	76.7	167.5
P_{unipolar}	1868.5	0.920	0.011	0.450	337.7	181.6
$P_{\text{semi-bipolar}}$	1868.5	0.881	0.143	0.450	392.1	160.8
S_{bipolar}	4.432	1.157	0.009	0.434	34.2	137.6
S_{unipolar}	4.432	1.089	0.675	0.041	12.2	89.3
$S_{\text{semi-bipolar}}$	4.432	0.420	0.090	0.434	5884.4	1045.2
	$a \cdot 10^3$	b	c_1	$c_2 \cdot 10^3$	$c_3 \cdot 10^3$	
P_{bipolar}	53.8	4.624	–	–	–	
P_{unipolar}	59.6	1.718	–	–	–	
$P_{\text{semi-bipolar}}$	70.5	1.563	–	–	–	
S_{bipolar}	1.5	3.641	0	–0.096	0.273	
S_{unipolar}	16.8	0.062	0	–0.096	0.273	
$S_{\text{semi-bipolar}}$	1.5	1.608	0	–0.096	0.273	

$$\left. \begin{aligned} a_S^{(0)} &= \varsigma \cdot a_P^s \\ B_S^{(0)} &= \varsigma \cdot B_P^s \end{aligned} \right\} \text{ with } \varsigma = \frac{2(S_{\max} - S_{\min}) \cdot 1 \text{ C m}^{-2}}{(P_{\max} - P_{\min}) \cdot 100\%}. \quad (6.33)$$

The initial guess for the further parameters c_1 , c_2 as well as c_3 results from geometric considerations shown in Fig. 6.18a.

- Unipolar and Semi-bipolar Working Areas:** For these working areas, \mathbf{p}_P^s and \mathbf{p}_S^s from the bipolar working area represent appropriate initial guesses. However, with a view to ensuring convergence of the subsequent optimization approach, the parameter B should be excluded from identification, i.e., B_P^s and B_S^s as identified for the bipolar working area are directly used. It might also be necessary to exclude h_1 and h_2 during optimization, i.e., $h_{1,P}$, $h_{2,P}$, $h_{1,S}$ as well as $h_{2,S}$. If $S(E)$ is simulated in unipolar and semi-bipolar working areas without the model extension in (6.27), we can utilize a rescaled version of \mathbf{p}_P^s as suitable initial guess. Again, it is recommended to exclude B_S from identification and maybe $h_{1,S}$ as well as $h_{2,S}$ in addition.

6.7.2 Application to Piezoceramic Disk

Now, let us apply the aforementioned identification strategy to a piezoceramic disk (diameter 10.0 mm; thickness 2.0 mm), which is made of the ferroelectrically soft material PIC255. Table 6.4 contains the resulting components of \mathbf{p}_p^s and \mathbf{p}_s^s in the different working areas. As can be clearly seen, the identified parameters differ considerably for both the working areas and the physical quantities (i.e., electric polarization or mechanical strain). This emphasizes once again the importance of determining individual parameter vectors.

Figures 6.24 and 6.25 depict various measurements as well as simulations for the piezoceramic disk in unipolar and semi-bipolar working areas, respectively. The left panels deal with electric polarizations P of the disk and the right panels show the obtained mechanical strains S . Due to the fact that the initial polarization state of the disk is, strictly speaking, unknown in both working areas, it is not possible to determine absolute values for P and S . We exclusively quantify changes of the quantities instead, which are denoted by ΔP and ΔS . As the comparisons in the Figs. 6.24a, b and 6.25a, b reveal, Preisach hysteresis modeling yields reliable simulations for $\Delta P(E)$ and $\Delta S(E)$. This can also be seen in the Figs. 6.24c, d and 6.25c, d, which display the time signals utilized for identifying \mathbf{p}_p^s and \mathbf{p}_s^s (see Table 6.4). With a view to demonstrating the applicability of Preisach hysteresis modeling for piezoceramic actuators, additional comparisons were carried out by means of further time signals (Figs. 6.24e, f and 6.25e, f). Although these time signals have not been considered during parameter identification, simulations coincide very well with measurements. This is confirmed by the normalized relative deviation ϵ_r of the simulation results as shown in the Figs. 6.24g, h and 6.25g, h. In the particular cases, $|\epsilon_r|$ always stays below 6%. Summing up, it can be stated again that Preisach hysteresis modeling represents an excellent approach to predict the large-signal behavior of piezoceramic actuators, especially in unipolar and semi-bipolar working areas.

6.8 Inversion of Preisach Hysteresis Model

To conduct model-based compensation of hysteresis effects within ferroelectric actuators, we have to determine that input quantity $x_{\text{inv}}(k)$ for time step k , which yields the desired target output $y_{\text{tar}}(k)$. Under certain circumstances, it may be necessary to consider also specific boundary conditions such as applied mechanical prestress T and excitation frequency f . That is the reason why we define here input quantities $x_{\text{inv}}(k)$, target quantities $y_{\text{tar}}(k)$, and boundary conditions z_{bou} as follows (excitation voltage $u(k)$; mechanical displacement $d(k)$):

- $x_{\text{inv}}(k) \in \{E(k), u(k)\}$
- $y_{\text{tar}}(k) \in \{P(k), S(k), d(k)\}$
- $z_{\text{bou}} \in \{T, f\}$.

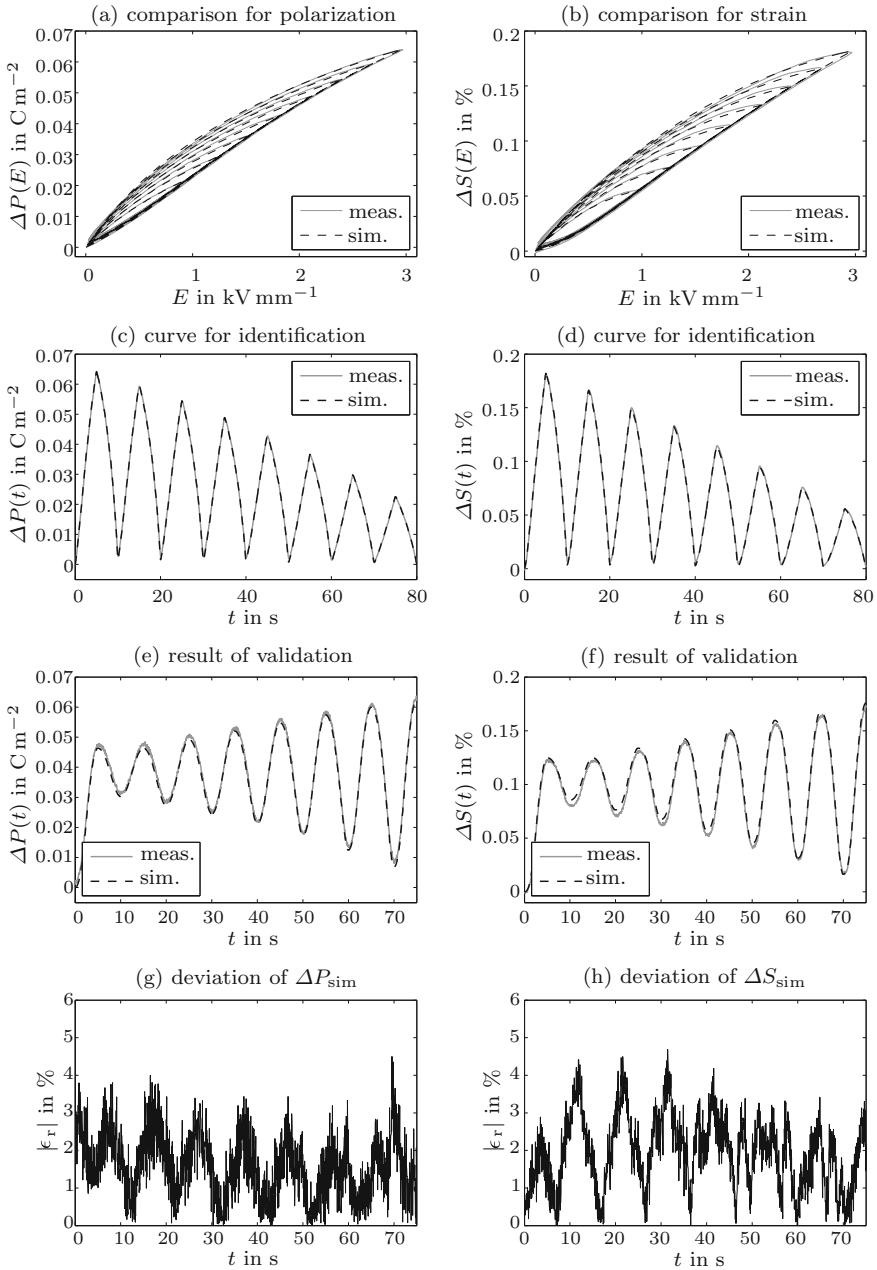


Fig. 6.24 a and b Comparison of measured and simulated hysteresis curves $\Delta P(E)$ and $\Delta S(E)$ in **unipolar** working area of the piezoceramic disk; c and d time signals for identifying weighting distributions; e and f time signals for validating Preisach hysteresis modeling; g and h resulting normalized relative deviations $|\epsilon_r|$ (magnitude) for validation signals

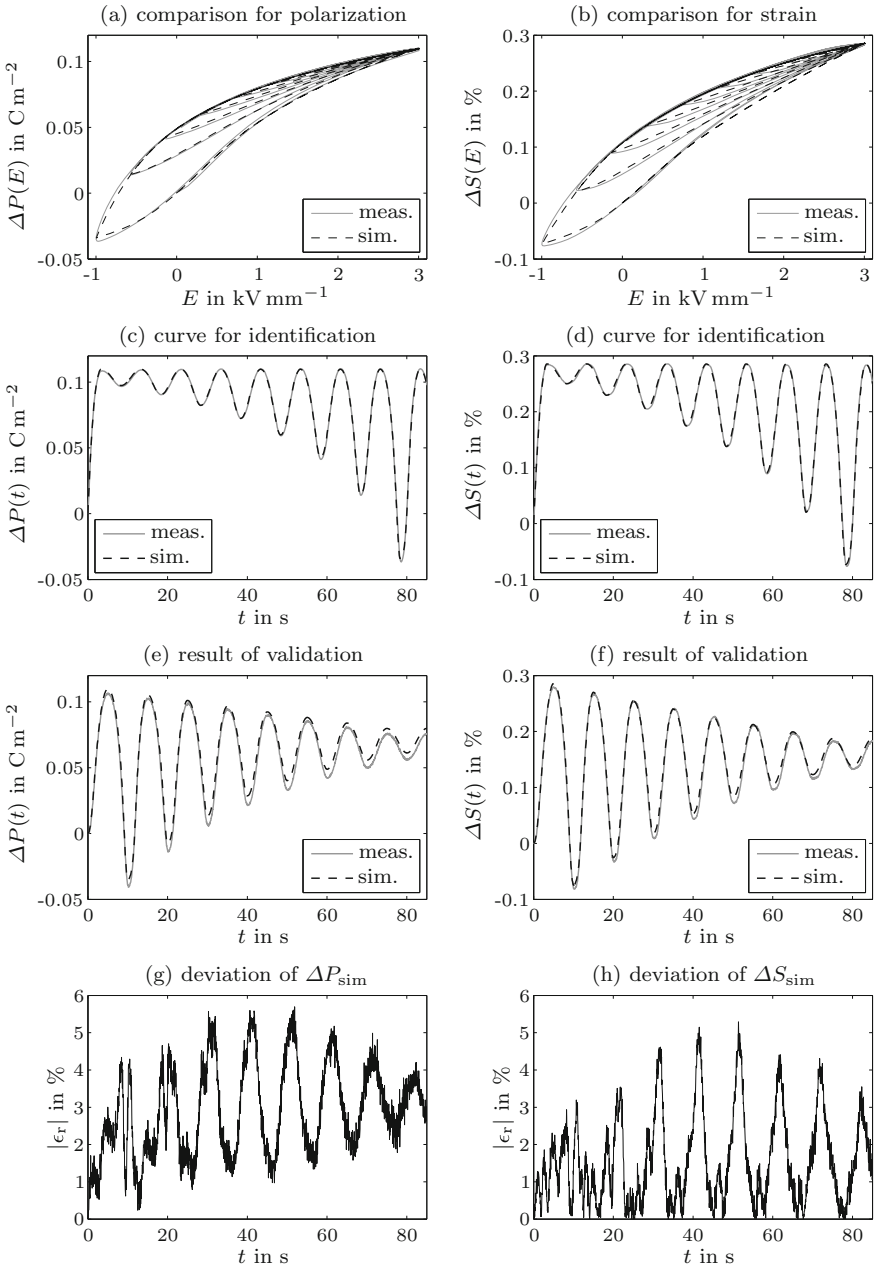


Fig. 6.25 a and b Comparison of measured and simulated hysteresis curves $\Delta P(E)$ and $\Delta S(E)$ in semi-bipolar working area of the piezoceramic disk; c and d time signals for identifying weighting distributions; e and f time signals for validating Preisach hysteresis modeling; g and h resulting normalized relative deviations $|\epsilon_r|$ (magnitude) for validation signals

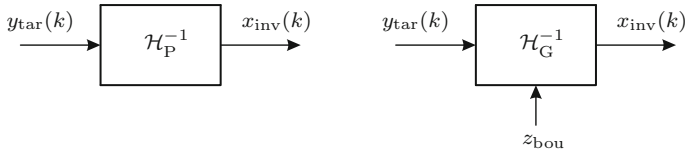


Fig. 6.26 Inverted (classical) Preisach hysteresis operator \mathcal{H}_P^{-1} and inverted generalized Preisach hysteresis operator \mathcal{H}_G^{-1}

Generalized Preisach hysteresis modeling can be used to predict the hysteretic behavior of electric polarizations $P(k)$ and mechanical strains $S(k)$ for ferroelectric materials. Since these quantities represent target quantities, the underlying Preisach hysteresis operator \mathcal{H}_P has to be inverted. In other words, the inverted generalized Preisach hysteresis operator \mathcal{H}_G^{-1} and, thus, the inverted Preisach hysteresis operator \mathcal{H}_P^{-1} are required for model-based compensation of hysteresis effects (see Fig. 6.26). However, owing to the fact that the elementary switching operators $\gamma_{\alpha\beta}$ exhibit discontinuities at the changeover points α and β , there does not exist a closed-form solution for this task. Consequently, \mathcal{H}_P has to be inverted numerically.

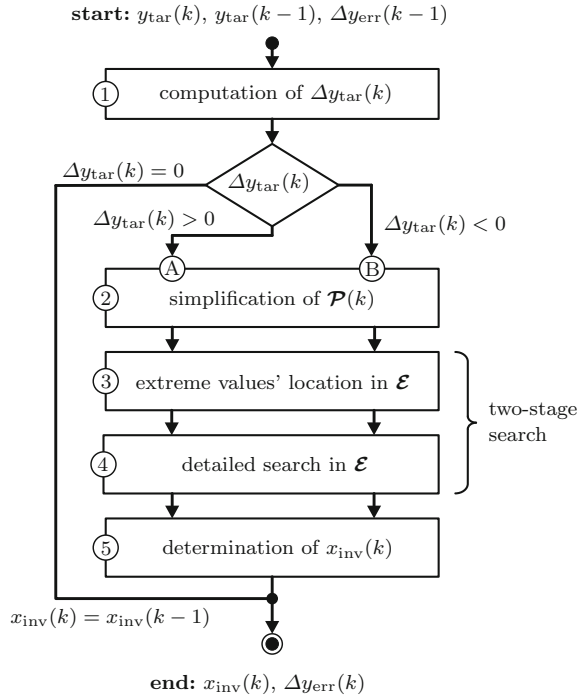
One can find various approaches in literature to obtain an appropriate approximation of \mathcal{H}_P^{-1} . Several methods are based on iterative algorithms for locally inverting discretized Preisach hysteresis models. For instance, Mittal and Menq [66] as well as Tan and Baras [92] exploited such algorithms to compensate hysteresis of electromagnetic and magnetostrictive actuators. Viswamurthy and Ganguli [95] utilized a locally inverted Preisach hysteresis model for controlling mechanical vibrations through piezoelectric stack actuators. A different approach to achieve \mathcal{H}_P^{-1} results from exchanging its input and output (e.g., [22, 91]). Thereby, the weighting distribution $\mu_{\mathcal{H}}(\alpha, \beta)$ for $\gamma_{\alpha\beta}$ has also to be inverted. With a view to ensuring positive weighting distributions, Bi et al. [12] introduced an analytical weighting distribution as well as an additional switching operator. They applied this approach for ferromagnetic materials and present convincing results. Due to exchanging input and output of \mathcal{H}_P , the physical meaning, however, gets lost which may cause problems regarding generalized Preisach hysteresis models.

Here, let us discuss an inverted Preisach hysteresis model that was developed by Wolf and colleagues [101, 102]. Section 6.8.1 deals with the underlying iterative inversion procedure, which is characterized in Sect. 6.8.2. Subsequently, the main steps toward an inverted generalized Preisach hysteresis model are addressed. Finally, model-based hysteresis compensation is applied to a piezoceramic disk.

6.8.1 Inversion Procedure

The computation of the sought-after input quantity $x_{inv}(k)$ yielding the target quantity $y_{tar}(k)$ for time step k is performed incrementally. The target quantity has to be

Fig. 6.27 Simplified flow chart for incrementally determining outputs of inverted Preisach hysteresis operator $\mathcal{H}_P^{-1}; y_{\text{tar}}(k)$ and $x_{\text{inv}}(k) = \mathcal{H}_P^{-1}[y_{\text{tar}}](k)$ represent desired target quantity and sought-after quantity for time step k , respectively



considered for the current as well as previous time step, i.e., $y_{\text{tar}}(k)$ and $y_{\text{tar}}(k-1)$. At each time step k , we analyze and simplify the current configuration of the Preisach plane $\mathcal{P}(k)$. Thereby, the vectors $\mathbf{e}_i(k)$, $\mathbf{e}_j(k)$ and $\mathbf{s}(k)$ are used to indicate location as well as sign of dominating extrema in $\mathcal{P}(k)$ (see (6.12) and (6.13)). The inversion procedure is mainly based on a two-stage evaluation of the Everett matrix $\mathcal{E} = [\mathcal{E}_{ij}]$. Figure 6.27 shows a simplified flow chart of the entire inversion procedure comprising five steps, which are explained below.

1. Computation of the Increment $\Delta y_{\text{tar}}(k)$

In a first step, the increment $\Delta y_{\text{tar}}(k)$ is computed which represents the change of the target output y_{tar} from time step $k-1$ to time step k , i.e.,

$$\Delta y_{\text{tar}}(k) = y_{\text{tar}}(k) - y_{\text{tar}}(k-1) \quad (6.34)$$

If $\Delta y_{\text{tar}}(k) = 0$ is fulfilled, one can directly continue with the subsequent time step $k+1$. The resulting output of the inverted Preisach hysteresis model is then given by $x_{\text{inv}}(k) = x_{\text{inv}}(k-1)$. This also holds for several further special cases like saturation in the Preisach plane and an increment $\Delta y_{\text{tar}}(k)$ that is smaller than the discretization error $\Delta y_{\text{err}}(k)$ from the previous iteration. How-

ever, when $\Delta y_{\text{tar}}(k) \neq 0$, we need to distinguish between two cases depending on its sign (see (6.4) and (6.5)):

- Ⓐ increasing $y_{\text{tar}}(k)$, i.e., $\Delta y_{\text{tar}}(k) > 0 \Rightarrow$ modification of α
- Ⓑ decreasing $y_{\text{tar}}(k)$, i.e., $\Delta y_{\text{tar}}(k) < 0 \Rightarrow$ modification of β .

Hence, the dividing line $\mathcal{L}(k)$ in the Preisach plane $\mathcal{P}(k)$ is modified.

2. Simplification of the Preisach Plane $\mathcal{P}(k)$

Actually, there exist various different configurations of $\mathcal{P}(k)$, e.g., number of steps in $\mathcal{L}(k)$ (see, e.g., Fig. 6.7). To standardize the subsequent inverting approach in step 3 and 4, let us simplify the configurations by reducing them to two cases, which are displayed in Fig. 6.28. For the particular configurations, the reduction implies deleting the m th entry of the vectors $\mathbf{e}_i(k)$, $\mathbf{e}_j(k)$ and $\mathbf{s}(k)$. Consequently, the output of the Preisach hysteresis operator changes by $\Delta y_{\text{simp}}(k)$ (hatched area in Fig. 6.28), which has to be included in the current increment $\Delta y_{\text{tar}}(k)$ of the target output, i.e.,

$$\begin{aligned} \Delta y'_{\text{tar}}(k) &= \Delta y_{\text{tar}}(k) + \Delta y_{\text{simp}}(k) \cdot \mathbf{s}_m(k) \\ &= \Delta y_{\text{tar}}(k) + \mathcal{E}_{i_m j_m} \cdot \mathbf{s}_m(k) . \end{aligned} \quad (6.35)$$

The following two steps deal with an iterative search in the Everett matrix \mathcal{E} . While the first one represents a coarse search, the second one is a detailed search.

3. Evaluation of Extreme Values' Locations in the Everett Matrix \mathcal{E}

The first iterative search steps exclusively considers dominating extrema in $\mathcal{P}(k)$ that are specified through the vectors $\mathbf{e}_i(k)$, $\mathbf{e}_j(k)$, and $\mathbf{s}(k)$. If necessary, the wiping-out rule of the Preisach hysteresis operator has to be applied in addition. Principally, the first iterative search step consists of three substeps (see Fig. 6.29).

- The starting point is the dominating extremum (index m), which exhibits the smallest magnitude. From this extremum, we readout the entries of $\mathcal{E} = [\mathcal{E}_{ij}]$ in descending order according to the components of $\mathbf{e}_i(k)$ and $\mathbf{e}_j(k)$. This procedure is conducted until the condition

$$\underbrace{\left| \sum_{\nu=m}^{n+1} \mathcal{E}_{i_\nu j_\nu} \cdot \mathbf{s}_\nu(k) \right|}_{\Delta y_{\text{ext}}(k)} < \left| \Delta y'_{\text{tar}}(k) \right| < \left| \sum_{\nu=m}^n \mathcal{E}_{i_\nu j_\nu} \cdot \mathbf{s}_\nu(k) \right| \quad (6.36)$$

is fulfilled.

- Now, the components $m, \dots, n+1$ of $\mathbf{e}_i(k)$, $\mathbf{e}_j(k)$ and $\mathbf{s}(k)$ are used to adjust the modified increment $\Delta y'_{\text{tar}}(k)$ of the target function by means of $\mathcal{E}_{i_\nu j_\nu}$, which leads to

$$\begin{aligned}\Delta y''_{\text{tar}}(k) &= \Delta y'_{\text{tar}}(k) + \Delta y_{\text{ext}}(k) \\ &= \Delta y'_{\text{tar}}(k) + \sum_{\nu=m}^{n+1} \mathcal{E}_{i_\nu j_\nu} \cdot \mathfrak{s}_\nu(k) .\end{aligned}\quad (6.37)$$

- At the end of the first iterative search step, the components $m, \dots, n+1$ of $\mathbf{e}_i(k)$, $\mathbf{e}_j(k)$ and $\mathfrak{s}(k)$ are deleted. We store the indices (i_ν, j_ν) of the extremum that was deleted at last.

As a result, one knows the two dominating extrema between which the sought-after entry is located in the Everett matrix \mathcal{E} . Besides, the configuration of the Preisach plane is further simplified.

4. Detailed Search for Correct Entry in the Everett Matrix \mathcal{E}

The second iterative search (detailed search) can be performed in a strongly restricted region of \mathcal{E} . For an increasing target output $y_{\text{tar}}(k)$ (i.e., case $\textcircled{\text{A}}$), the search is done along column j_m (see Fig. 6.30). In the other case (i.e., $\textcircled{\text{B}}$), one has to search in row i_m . The procedure starts in both cases at the entry $\mathcal{E}_{i_\nu j_\nu}$ featuring the indices (i_ν, j_ν) that were stored in step 3. It is desired to find the entry $\mathcal{E}_{i_r j_s}$, which coincides with $y''_{\text{tar}}(k)$ best possible, i.e.,

$$\min(|\Delta y''_{\text{tar}}(k) - \mathcal{E}_{i_r j_s}|) \quad \text{with} \quad \begin{cases} j_s = j_m & \text{for } \textcircled{\text{A}} \\ i_r = i_m & \text{for } \textcircled{\text{B}} . \end{cases} \quad (6.38)$$

An efficient method for this task is the *divide and conquer search algorithm* [54]. Even if a fine spatial discretization (e.g., $M = 800$) of the Preisach plane is utilized, the inverting procedure will require reasonable computation time.

5. Determination of the sought-after Input $x_{\text{inv}}(k)$

The indices (i_r, j_s) from step 4 are used to update $x_{\text{inv}}(k-1)$. Depending on the progression of the target output $y_{\text{tar}}(k)$, i.e., whether it is rising or falling, we choose one of the following equations (cf. Fig. 6.31)

$$x_{\text{inv}}(k) = \frac{M - i_r}{M - 1} - 0.5 \quad \text{for } \textcircled{\text{A}} \quad (6.39)$$

$$x_{\text{inv}}(k) = 0.5 - \frac{M - j_s}{M - 1} \quad \text{for } \textcircled{\text{B}} . \quad (6.40)$$

Furthermore, the discretization error $\Delta y_{\text{err}}(k)$ between the increments of actually computed target quantity $\Delta y_{\text{inv}}(k)$ and of desired target output $\Delta y_{\text{tar}}(k)$ is calculated, which is, therefore, given by

$$\Delta y_{\text{err}}(k) = \Delta y_{\text{inv}}(k) - \Delta y''_{\text{tar}}(k) = \mathcal{E}_{i_r j_s} \cdot \mathfrak{s}_m(k) - \Delta y''_{\text{tar}}(k) . \quad (6.41)$$

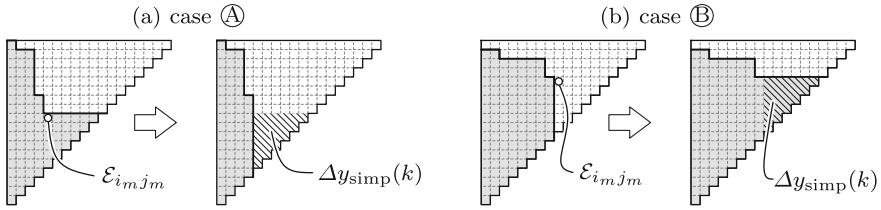


Fig. 6.28 Simplification of Preisach plane $\mathcal{P}(k)$

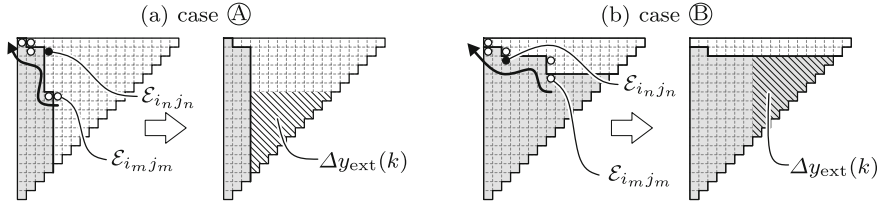


Fig. 6.29 Coarse search based on evaluation of extreme values' location in Everett matrix $\mathcal{E} = [\mathcal{E}_{ij}]$ and further simplification of Preisach plane

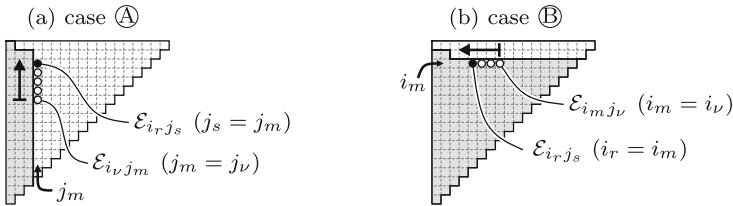


Fig. 6.30 Detailed search to figure out entry \mathcal{E}_{i_r, j_s} in Everett matrix

Note that $\Delta y_{err}(k)$ has to be considered in step 1. Finally, we update the vectors $\mathbf{e}_i(k)$, $\mathbf{e}_j(k)$, and $\mathbf{s}(k)$ according to the current input quantity $x_{inv}(k)$. This results in $\mathbf{e}_i(k + 1)$, $\mathbf{e}_j(k + 1)$ as well as $\mathbf{s}(k + 1)$.

At the end of the whole inverting procedure, information is available which is necessary to determine $x_{inv}(k + 1)$ for the subsequent time step $k + 1$. In doing so, we start again with step 1 by considering the quantities $y_{tar}(k)$, $y_{tar}(k + 1)$, and $\Delta y_{err}(k)$.

6.8.2 Characterization of Inversion Procedure

To characterize the inversion procedure, let us check its functionality and rate its efficiency in addition. These investigations are carried out through a serial connection of inverted Preisach hysteresis operator \mathcal{H}_p^{-1} and original one, i.e., \mathcal{H}_p (see Fig. 6.32) [101, 102]. We assume a target quantity $y_{tar}(k)$ that represents the input of \mathcal{H}_p^{-1} . The resulting output $x_{inv}(k) = \mathcal{H}_p^{-1}[y_{tar}](k)$ serves then again as input of \mathcal{H}_p ,

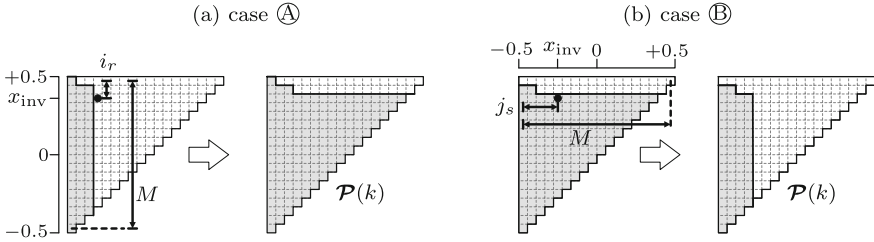


Fig. 6.31 Calculation of sought-after quantity $x_{inv}(k)$ resulting from indices (i_r, j_s) ; update of Preisach plane $\mathcal{P}(k)$

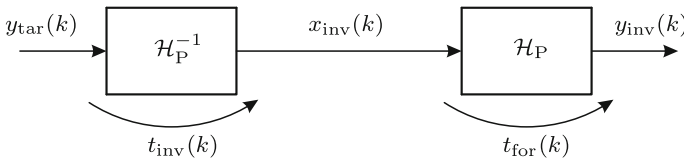


Fig. 6.32 Approach to check functionality and to rate efficiency of inversion procedure; computation time $t_{inv}(k)$ for inversion procedure; computation time $t_{for}(k)$ for evaluating \mathcal{H}_P in forward direction

which leads to the final output $y_{inv}(k) = \mathcal{H}_P[x_{inv}](k)$. Hence, one is able to compare the desired target quantity $y_{tar}(k)$ with the quantity $y_{inv}(k)$ actually determined.

Figure 6.33a displays the utilized discrete-time target signal consisting of an offset and two superimposed sine waves. The sine waves feature different amplitudes as well as frequencies, respectively. For the evaluation of \mathcal{H}_P and \mathcal{H}_P^{-1} , a spatial discretization of $M = 200$ was applied in the Preisach plane. Figure 6.33b compares the desired target quantity with the output of the serial connection in a small time window. As the comparison reveals, $y_{inv}(k)$ coincides very well with $y_{tar}(k)$. Apart from deviations due to the spatial discretization of the Preisach plane, there do not arise any further deviations. It can, thus, be stated that the inversion procedure provides reliable results.

The computation time of the inversion procedure denotes a decisive criterion with regard to practical applications. Strictly speaking, the maximum duration $t_{inv,max}$ that is required for a single time step determines the maximum sampling rate $f_{inv,max} = 1/t_{inv,max}$ for inverting the target quantity $y_{tar}(k)$. If model-based hysteresis compensation is applied in open- or closed-loop control, $x_{inv}(k)$ can be updated after the time interval $t_{inv,max}$, i.e., $t_{k+1} - t_k \geq t_{inv,max}$. In Fig. 6.33c, one can see the duration $t_{inv}(k)$ for time step k , which is required for inverting $y_{tar}(k)$ in the considered time window (cf. Fig. 6.33b). The calculations were conducted on a standard desktop PC.¹⁰ Interestingly, $t_{inv}(k)$ takes mainly two values. The lower value results from termination conditions in step 1 of the inversion procedure, whereas the higher value $t_{inv,max}$ is a consequence of running through all steps (i.e., step 1 to step 5). Note that even if the target quantity y_{tar} exhibits an arbitrary progress, $t_{inv,max}$ will never be exceeded.

¹⁰Desktop PC: Intel Core i5 with 3.19GHz and 4 GB RAM.

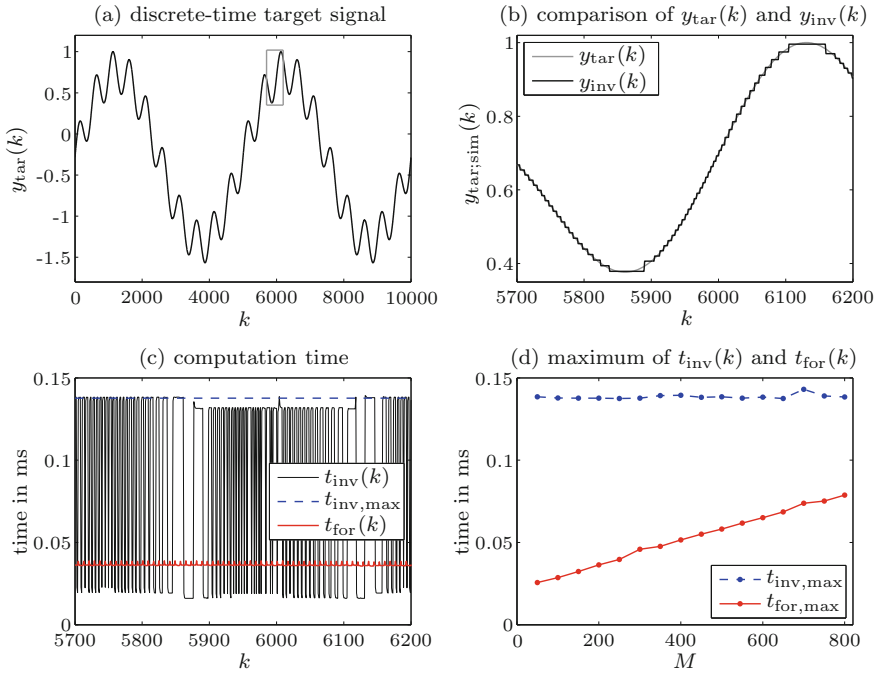


Fig. 6.33 Characterization of inversion procedure: **a** Discrete-time target signal $y_{tar}(k)$; **b** comparison of $y_{tar}(k)$ and output $y_{inv}(k)$ (cf. Fig. 6.32) for spatial discretization $M = 200$; **c** computation times for inversion procedure $t_{inv}(k)$ as well as forward calculation $t_{for}(k)$; maximum computation time $t_{inv,max}$; **d** comparison of $t_{inv,max}$ and $t_{for,max}$ with respect to M

As a result, $t_{inv,max} < 0.15$ ms is guaranteed for the spatial discretization $M = 200$, which leads to the sampling rate $f_{inv,max} = 6.67$ kHz.

Figure 6.33d depicts maximum durations $t_{inv,max}$ of the inversion procedure for different spatial discretizations M . Moreover, maximum durations $t_{for,max}$ per time step (cf. Fig. 6.32) are shown for evaluating the Preisach hysteresis operator \mathcal{H}_P in forward direction. It is worth to emphasize that $t_{inv,max}$ stays almost constant in the considered range of spatial discretizations. This behavior can be ascribed to the efficient divide and conquer search algorithm in step 4 of the inversion procedure. However, contrary to $t_{inv,max}$, the duration $t_{for,max}$ increases almost along a straight line with rising M .

According to these findings, the presented inversion procedure is an efficient method for inverting Preisach hysteresis operators. Since the underlying algorithm allows time-efficient computation of the desired quantities, it can be exploited for both open- and closed-loop control of actuators exhibiting hysteretic behavior. The inversion procedure is not restricted to ferroelectric actuators but can also be used for actuators containing ferromagnetic materials.

6.8.3 Inverting Generalized Preisach Hysteresis Model

The generalized Preisach hysteresis operator \mathcal{H}_G (see Sect. 6.6) for ferroelectric materials comprises reversible parts, asymmetric behavior, mechanical deformations as well as consideration of rate-dependent behavior and applied uniaxial mechanical stresses. If generalization is restricted to reversible parts and asymmetric behavior, we can evaluate the inverted generalized Preisach hysteresis operator \mathcal{H}_G^{-1} in the same manner as given in Sect. 6.8.1. This can be ascribed to the fact that both generalizations directly alter the weighting distribution $\mu_{\mathcal{H}}(\alpha, \beta)$ for the Preisach hysteresis model. However, in case of the remaining generalizations (e.g. mechanical deformation), further important points arise during inverting \mathcal{H}_G , which are discussed below.

Let us start with the inversion approach for mechanical deformations S and mechanical displacements d of ferroelectric materials. In the bipolar working area, there exist two solutions of these target quantities for positive and negative electrical excitations. Thus, it is impossible to invert S and d uniquely. Ferroelectric actuators, however, usually operate in unipolar and semi-bipolar working areas. Due to this fact, we are able to describe the underlying large-signal behavior through a generalized Preisach hysteresis operator \mathcal{H}_G that does not require the extension given in (6.27). As a result, the sought-after input quantities electric field intensity E and excitation voltage u of ferroelectric actuators can be determined according to the inversion procedure in Sect. 6.8.1. For instance, the target quantity $d(k)$ for time step k serves as input of the inverted generalized Preisach hysteresis operator \mathcal{H}_G^{-1} , which leads to the output $u(k) = \mathcal{H}_G^{-1}[d](k)$.

To consider rate-dependent behavior and mechanical stresses for ferroelectric materials by means of \mathcal{H}_G , one has to take additional inputs (i.e., $z_{\text{bou}} \in \{T, f\}$) into account, respectively. The inputs modify the spatially discretized weighting distribution μ and, consequently, the Everett matrix \mathcal{E} (see Sects. 6.6.4 and 6.6.5). It is of utmost importance to incorporate such modifications in the inversion procedure since only by doing so, we are able to determine reliable outputs of \mathcal{H}_G^{-1} . For that reason, $\mu(z_{\text{bou}})$ as well as $\mathcal{E}(z_{\text{bou}})$ should be calculated for different inputs z_{bou} in advance [101]. In practical applications of ferroelectric actuators, the task is to select an appropriate spatially discretized weighting distribution and Everett matrix. The selection depends, of course, on the boundary conditions z_{bou} , which actually occur during application.

6.8.4 Hysteresis Compensation for Piezoceramic Disk

Here, model-based compensation of hysteresis effects through an inverted generalized Preisach hysteresis operator is applied to a piezoceramic disk (diameter 10.0 mm; thickness 2.0 mm), which is made of the ferroelectrically soft material PIC255. Before the results are presented, let us discuss a particular hardware-based approach

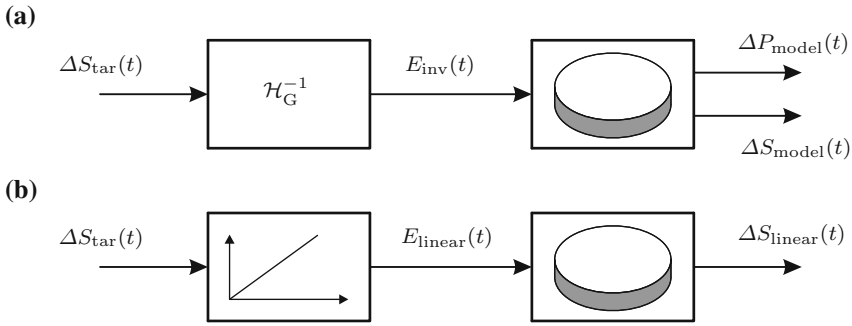


Fig. 6.34 Block diagram to achieve desired mechanical strains $\Delta S_{tar}(t)$ of the piezoceramic disk for **a** model-based hysteresis compensation and **b** uncompensated case (i.e., linearization); determined quantities: $E_{inv}(t)$ and $E_{linear}(t)$; measured quantities: $\Delta P_{model}(t)$, $\Delta S_{model}(t)$ as well as $\Delta S_{linear}(t)$

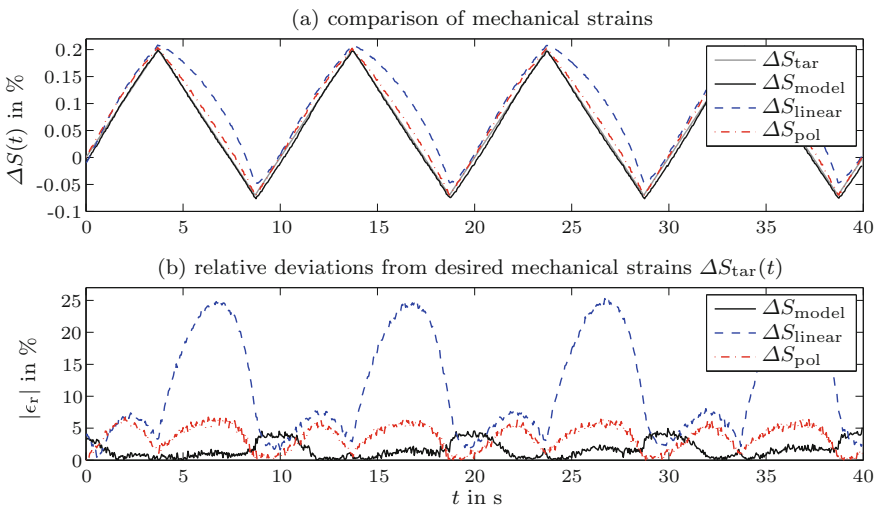


Fig. 6.35 **a** Comparison of desired mechanical strains $\Delta S_{tar}(t)$ and achieved quantities with respect to time t ; measured quantities: $\Delta S_{model}(t)$ and $\Delta S_{linear}(t)$; computed quantity: $\Delta S_{pol}(t)$; **b** normalized relative deviations $|\epsilon_r|$ (magnitude) between resulting strains and desired ones; piezoceramic disk (diameter 10.0 mm; thickness 2.0 mm; material PIC255)

for compensating nonlinearities of ferroelectric actuators. Contrary to model-based compensation where we use electrical voltage as excitation signal, this hardware-based approach directly relates to the electric polarization (e.g., [28, 29, 108]). To influence the electric polarization within the ferroelectric material, electric charges Q are impressed on the actuator electrodes by means of an appropriate charge drive circuit. It is assumed that Q is directly proportional to the resulting mechanical strain S of the ferroelectric actuator, i.e., $Q \propto S$. Although a remarkable reduction of

nonlinearities is achieved compared to open-loop configurations operating with voltage excitations, charge drive circuits usually exhibit substantial drawbacks. This includes limited low-frequency performance, dependence of voltage gain on capacitance of the ferroelectric material as well as time-consuming tuning procedure. Besides, when the ferroelectric actuator is driven into saturation (e.g., semi-bipolar working area), the relation of electric charge and mechanical displacement will be no longer linear [101]. As a result, the deviations of desired and actually achieved displacements of the ferroelectric actuator increase.

To compare the different types of compensations, let us desire a triangular-shaped time signal for the mechanical strain of the piezoceramic disk. The model-based compensation exploits the inverted generalized Preisach hysteresis operator \mathcal{H}_G^{-1} to obtain the electrical excitation signal $E_{\text{inv}}(t)$, which is then applied to the disk sample for measurements (see Fig. 6.34a). Against that, we emulate mechanical strains $\Delta S_{\text{pol}}(t)$ of the hardware-based solution by rescaling the electric polarization $P_{\text{model}}(t)$. The expression $P_{\text{model}}(t)$ stands for the measured electric polarization actually occurring in the disk. Since the underlying rescaling does not exhibit any dependencies on electronic components, it represents the best case for charge drive circuits in open-loop configuration. Figure 6.35a depicts target strains $\Delta S_{\text{tar}}(t)$, measured strains $\Delta S_{\text{model}}(t)$ for model-based compensation of hysteresis effects as well as those for hardware-based compensation $\Delta S_{\text{pol}}(t)$. Moreover, measured strains $\Delta S_{\text{linear}}(t)$ for the uncompensated case are given meaning that the electrical excitation signal $E_{\text{linear}}(t)$ is assumed to be directly proportional to the desired mechanical strain $\Delta S_{\text{tar}}(t)$ (see Fig. 6.34b). The comparison of the different strain curves clearly indicates that $\Delta S_{\text{model}}(t)$ coincides best with $\Delta S_{\text{tar}}(t)$. In contrast, there occur normalized relative deviations of $\Delta S_{\text{linear}}(t)$ up to 25% (see Fig. 6.35b), which emphasizes the importance of considering hysteresis effects in actuator applications.

References

1. Adly, A.A., Mayergoz, I.D., Bergqvist, A.: Preisach modeling of magnetostrictive hysteresis. *J. Appl. Phys.* **69**(8), 5777–5779 (1991)
2. Al Janaideh, M., Su, C.Y., Rakheja, S.: Development of the rate-dependent Prandtl-Ishlinskii model for smart actuators. *Smart Mater. Struct.* **17**(3), 035,026 (2008)
3. Al Janaideh, M., Rakheja, S., Su, C.Y.: A generalized Prandtl-Ishlinskii model for characterizing the hysteresis and saturation nonlinearities of smart actuators. *Smart Mater. Struct.* **18**(4), 045,001 (2009)
4. Arockiarajan, A., Sansour, C.: Micromechanical modeling and simulation of rate-dependent effects in ferroelectric polycrystals. *Comput. Mater. Sci.* **43**(4), 842–854 (2008)
5. Azzerboni, B., Cardelli, E., Finocchio, G., La Foresta, F.: Remarks about Preisach function approximation using Lorentzian function and its identification for nonoriented steels. *IEEE Trans. Magn.* **39**, 3028–3030 (2003)
6. Azzerboni, B., Carpentieri, M., Finocchio, G., Ipsale, M.: Super-Lorentzian Preisach function and its applicability to model scalar hysteresis. *Phys. B: Condens. Matter* **343**, 121–126 (2004)
7. Ball, B.L., Smith, R.C., Kim, S.J., Seelecke, S.: A stress-dependent hysteresis model for ferroelectric materials. *J. Intell. Mater. Syst. Struct.* **18**(1), 69–88 (2007)

8. Bassiouny, E., Ghaleb, A.F., Maugin, G.A.: Thermodynamical formulation for coupled electromechanical hysteresis effects - I. Basic equations. *IEEE Trans. Ultrason. Ferroelectr. Freq. Control* **26**(12), 1279–1295 (1988)
9. Belov, A.Y., Kreher, W.S.: Viscoplastic models for ferroelectric ceramics. *J. Eur. Ceram. Soc.* **25**(12), 2567–2571 (2005)
10. Bergqvist, A., Engdahl, G.: A stress-dependent magnetic Preisach hysteresis model. *IEEE Trans. Magn.* **27**(6 pt 2), 4796–4798 (1991)
11. Bertotti, G.: Dynamic generalization of the scalar Preisach model of hysteresis. *IEEE Trans. Magn.* **28**(5), 2599–2601 (1992)
12. Bi, S., Sutor, A., Lerch, R., Xiao, Y.: An efficient inverted hysteresis model with modified switch operator and differentiable weight function. *IEEE Trans. Magn.* **49**(7), 3175–3178 (2013)
13. Boddu, V., Endres, F., Steinmann, P.: Molecular dynamics study of ferroelectric domain nucleation and domain switching dynamics. *Sci. Rep.* **7**(1) (2017)
14. Chaplya, P.M., Carman, G.P.: Dielectric and piezoelectric response of lead zirconate-lead titanate at high electric and mechanical loads in terms of non-180° domain wall motion. *J. Appl. Phys.* **90**(10), 5278–5286 (2001)
15. Chonan, S., Jiang, Z., Yamamoto, T.: Nonlinear hysteresis compensation of piezoelectric ceramic actuators. *J. Intell. Mater. Syst. Struct.* **7**(2), 150–156 (1996)
16. Cohen, R.E.: Origin of ferroelectricity in perovskite oxides. *Nature* **358**(6382), 136–138 (1992)
17. Cohen, R.E.: Theory of ferroelectrics: A vision for the next decade and beyond. *J. Phys. Chem. Solids* **61**(2), 139–146 (2000)
18. Damjanovic, D.: Ferroelectric, dielectric and piezoelectric properties of ferroelectric thin films and ceramics. *Rep. Prog. Phys.* **61**, 1267–1324 (1998)
19. Davino, D., Giustini, A., Visone, C.: Design and test of a stress-dependent compensator for magnetostrictive actuators. *IEEE Trans. Magn.* **2**, 646–649 (2010)
20. Della Torre, E., Vajda, F.: Parameter identification of the complete-moving-hysteresis model using major loop data. *IEEE Trans. Magn.* **30**(6), 4987–5000 (1994)
21. Devonshire, A.F.: Theory of ferroelectrics. *Adv. Phys.* **3**(10), 85–130 (1954)
22. Dlala, E., Saitz, J., Arkkio, A.: Inverted and forward Preisach models for numerical analysis of electromagnetic field problems. *IEEE Trans. Magn.* **42**, 1963–1973 (2006)
23. Dong, R., Tan, Y.: A modified Prandtl-Ishlinskii modeling method for hysteresis. *Phys. B: Condens. Matter* **404**(8–11), 1336–1342 (2009)
24. Ducharme, B., Zhang, B., Guyomar, D., Sebald, G.: Fractional derivative operators for modeling piezoceramic polarization behaviors under dynamic mechanical stress excitation. *Sens. Actuators A: Phys.* **189**, 74–79 (2013)
25. Endres, F., Steinmann, P.: Molecular statics simulations of head to head and tail to tail nanodomains of rhombohedral barium titanate. *Comput. Mater. Sci.* **97**, 20–25 (2015)
26. Everett, D.H.: A general approach to hysteresis. Part 4. An alternative formulation of the domain model. *Trans. Faraday Soc.* **51**, 1551–1557 (1955)
27. Finocchio, G., Carpentieri, M., Cardelli, E., Azzèrboni, B.: Analytical solution of Everett integral using Lorentzian Preisach function approximation. *J. Magn. Magn. Mater.* **300**, 451–470 (2006)
28. Fleming, A.J.: Charge drive with active DC stabilization for linearization of piezoelectric hysteresis. *IEEE Trans. Ultrason. Ferroelectr. Freq. Control* **60**(8), 1630–1637 (2013)
29. Fleming, A.J., Moheimani, S.O.R.: Improved current and charge amplifiers for driving piezoelectric loads, and issues in signal processing design for synthesis of shunt damping circuits. *J. Intell. Mater. Syst. Struct.* **15**(2), 77–92 (2004)
30. Freeman, A.R., Joshi, S.P.: Numerical modeling of PZT nonlinear electromechanical behavior. *Proc. SPIE - Int. Soc. Opt. Eng.* **2715**, 602–613 (1996)
31. Füzı, J.: Computationally efficient rate dependent hysteresis model. *COMPEL - Int. J. Comput. Math. Electr. Electron. Eng.* **18**(3), 445–457 (1999)

32. Ge, P., Jouaneh, M.: Generalized preisach model for hysteresis nonlinearity of piezoceramic actuators. *J. Precis. Eng.* **20**, 99–111 (1997)
33. Gu, G., Zhu, L.: Modeling of rate-dependent hysteresis in piezoelectric actuators using a family of ellipses. *Sens. Actuators A: Phys.* **165**(2), 303–309 (2011)
34. Guyomar, D., Ducharme, B., Sebald, G.: Dynamical hysteresis model of ferroelectric ceramics under electric field using fractional derivatives. *J. Phys. D: Appl. Phys.* **40**(19), 6048–6054 (2007)
35. Guyomar, D., Ducharme, B., Sebald, G., Audiger, D.: Fractional derivative operators for modeling the dynamic polarization behavior as a function of frequency and electric field amplitude. *EEE Trans. Ultrason. Ferroelectr. Freq. Control* **56**(3), 437–443 (2009)
36. Hegewald, T.: Modellierung des nichtlinearen Verhaltens piezokeramischer Aktoren. Ph.D. thesis, Friedrich-Alexander-University Erlangen-Nuremberg (2007)
37. Hegewald, T., Kaltenbacher, B., Kaltenbacher, M., Lerch, R.: Efficient modeling of ferroelectric behavior for the analysis of piezoceramic actuators. *J. Intell. Mater. Syst. Struct.* **19**(10), 1117–1129 (2008)
38. Hu, H., Ben Mrad, R.: On the classical Preisach model for hysteresis in piezoceramic actuators. *Mechatronics* **13**(2), 85–94 (2002)
39. Huber, J.E.: Micromechanical modelling of ferroelectrics. *Curr. Opin. Solid State Mater. Sci.* **9**(3), 100–106 (2005)
40. Huber, J.E., Fleck, N.A., Landis, C.M., McMeeking, R.M.: A constitutive model for ferroelectric polycrystals. *J. Mech. Phys. Solids* **47**, 1663–1697 (1999)
41. Hughes, D., Wen, J.T.: Preisach modeling of piezoceramic hysteresis; independent stress effect. *Math. Control Smart Struct.* **2442**, 328–336 (1995)
42. Hwang, S.C., Lynch, C.S., McMeeking, R.M.: Ferroelectric/ferroelastic interactions and a polarization switching model. *Acta Metall. Mater.* **43**(5), 2073–2084 (1995)
43. Janocha, H., Kuhn, K.: Real-time compensation of hysteresis and creep in piezoelectric actuators. *Sens. Actuators A: Phys.* **79**(2), 83–89 (2000)
44. Jiang, H., Ji, H., Qiu, J., Chen, Y.: A modified Prandtl-Ishlinskii model for modeling asymmetric hysteresis of piezoelectric actuators. *EEE Trans. Ultrason. Ferroelectr. Freq. Control* **57**(5), 1200–1210 (2010)
45. Jiles, D.C., Atherton, D.L.: Theory of ferromagnetic hysteresis. *J. Magn. Magn. Mater.* **61**(1), 48–60 (1986)
46. Jung, H., Shim, J.Y., Gweon, D.: New open-loop actuating method of piezoelectric actuators for removing hysteresis and creep. *Rev. Sci. Instrum.* **71**(9), 3436–3440 (2000)
47. Kadota, Y., Morita, T.: Preisach modeling of electric-field-induced strain of ferroelectric material considering 90° domain switching. *Jpn. J. Appl. Phys.* **51**(9), 09LE08–1–09LE081–6 (2012)
48. Kahler, G.R., Della Torre, E., Cardelli, E.: Implementation of the Preisach-Stoner-Wohlfarth classical vector model. *IEEE Trans. Magn.* **46**(1), 21–28 (2010)
49. Kaltenbacher, B., Kaltenbacher, M.: Modeling and iterative identification of hysteresis via Preisach operators in PDEs. *Lect. Adv. Comput. Methods Mech.* **1**, 1–45 (2007)
50. Kamlah, M.: Ferroelectric and ferroelastic piezoceramics - modeling of electromechanical hysteresis phenomena. *Contin. Mech. Thermodyn.* **13**, 219–268 (2001)
51. Kamlah, M., Böhle, U.: Finite element analysis of piezoceramic components taking into account ferroelectric hysteresis behavior. *Int. J. Solids Struct.* **38**(4), 605–633 (2001)
52. Kamlah, M., Tsakmakis, C.: Phenomenological modeling of the non-linear electro-mechanical coupling in ferroelectrics. *Int. J. Solids Struct.* **36**(5), 669–695 (1999)
53. Keip, M.A.: Modeling of electro-mechanically coupled materials on multiple scales. Ph.D. thesis, Universität Duisburg-Essen (2011)
54. Knuth, D.E.: *The Art of Computer Programming: vol. 3.* Addison-Wesley, Sorting and Searching (1998)
55. Krasnosel'skii, M.A., Pokrovskii, A.V.: *Systems with Hysteresis.* Springer, Berlin (1989)
56. Kurzhöfer, I.: Mehrskalens-Modellierung polykristalliner Ferroelektrika. Ph.D. thesis, Universität Duisburg-Essen (2007)

57. Landis, C.M.: Fully coupled, multi-axial, symmetric constitutive laws for polycrystalline ferroelectric ceramics. *J. Mech. Phys. Solids* **50**(1), 127–152 (2002)
58. Lenk, A., Ballas, R.G., Werthschützky, R., Pfeifer, G.: *Electromechanical Systems in Microtechnology and Mechatronics: Electrical, Mechanical and Acoustic Networks, their Interactions and Applications*. Springer, Berlin (2010)
59. Lin, C.J., Yang, S.R.: Precise positioning of piezo-actuated stages using hysteresis-observer based control. *Mechatronics* **16**(7), 417–426 (2006)
60. Ma, Y., Mao, J.: On modeling and tracking control for a smart structure with stress-dependent hysteresis nonlinearity. *Acta Autom. Sin.* **36**(11), 1611–1619 (2010)
61. Macki, J.W., Nistri, P., Zecca, P.: Mathematical models for hysteresis. *SIAM Rev.* **35**(1), 94–123 (1993)
62. Mayergoyz, I.D.: Hysteresis models from the mathematical and control theory points of view. *J. Appl. Phys.* **57**(8), 3803–3805 (1985)
63. Mayergoyz, I.D.: Dynamic preisach models of hysteresis. *IEEE Trans. Magn.* **24**(6), 2925–2927 (1988)
64. Mayergoyz, I.D.: *Mathematical Models of Hysteresis and their Applications*. Elsevier, New York (2003)
65. Meggitt Sensing Systems: Product portfolio (2018). <https://www.meggittsensingsystems.com>
66. Mittal, S., Menq, C.H.: Hysteresis compensation in electromagnetic actuators through preisach model inversion. *IEEE/ASME Trans. Mechatron.* **5**(4), 394–409 (2000)
67. Mrad, R.B., Hu, H.: A model for voltage-to-displacement dynamics in piezoceramic actuators subject to dynamic-voltage excitations. *IEEE/ASME Trans. Mechatron.* **7**(4), 479–489 (2002)
68. Nierla, M., Sutor, A., Rupitsch, S.J., Kaltenbacher, M.: Stageless evaluation for a vector Preisach model based on rotational operators. *COMPEL - Int. J. Comput. Math. Electr. Electron. Eng.* **36**(5), 1501–1516 (2017)
69. Oppermann, K., Armingier, B.R., Zagar, B.G.: A contribution to the classical scalar preisach hysteresis model for magneto-elastic materials. In: *Proceedings of IEEE/ASME International Conference on Mechatronics and Embedded Systems and Applications (MESA)*, pp. 180–185. IEEE (2010)
70. Padthe, A.K., Drincic, B., Oh, J.H., Rizos, D.D., Fassois, S.D., Bernstein, D.S.: Duhem modeling of friction-induced hysteresis. *IEEE Control Syst. Mag.* **28**(5), 90–107 (2008)
71. PI Ceramic GmbH: Product portfolio (2018). <https://www.piceramic.com>
72. Polomoff, N.A., Premnath, R.N., Bosse, J.L., Huey, B.D.: Ferroelectric domain switching dynamics with combined 20 nm and 10 ns resolution. *J. Mater. Sci.* **44**(19), 5189–5196 (2009)
73. Preisach, F.: über die magnetische Nachwirkung. *Zeitschrift für Physik* **94**(5–6), 277–302 (1935)
74. Quant, M., Elizalde, H., Flores, A., Ramírez, R., Orta, P., Song, G.: A comprehensive model for piezoceramic actuators: modelling, validation and application. *Smart Mater. Struct.* **18**(12), 1–16 (2009)
75. Rakotondrabe, M., Clévy, C., Lutz, P.: Complete open loop control of hysteretic, creeped, and oscillating piezoelectric cantilevers. *IEEE Trans. Autom. Sci. Eng.* **7**(3), 440–450 (2010)
76. Reiländer, U.: *Das Großsignalverhalten piezoelektrischer Aktoren*. Ph.D. thesis, Technische Universität München (2003)
77. Richter, H., Misawa, E.A., Lucca, D.A., Lu, H.: Modeling nonlinear behavior in a piezoelectric actuator. *Precis. Eng.* **25**(2), 128–137 (2001)
78. Rupitsch, S.J., Wolf, F., Sutor, A., Lerch, R.: Reliable modeling of piezoceramic materials utilized in sensors and actuators. *Acta Mech.* **223**, 1809–1821 (2012)
79. Sawyer, C.B., Tower, C.H.: Rochelle salt as a dielectric. *Phys. Rev.* **35**(3), 269–273 (1930)
80. Schrade, D.: *Microstructural modeling of ferroelectric material behavior*. Ph.D. thesis, Technische Universität Kaiserslautern (2011)
81. Schröder, J., Romanowski, H.: A simple coordinate invariant thermodynamic consistent model for nonlinear electro-mechanical coupled ferroelectrics. In: *Proceedings of European Congress on Computational Methods in Applied Science and Engineering (ECCOMAS)* (2004)

82. Schwaab, H., Grünbichler, H., Supancic, P., Kamlah, M.: Macroscopical non-linear material model for ferroelectric materials inside a hybrid finite element formulation. *Int. J. Solids Struct.* **49**(3–4), 457–469 (2012)
83. Sepiarsky, M., Asthagiri, A., Phillpot, S.R., Stachiotti, M.G., Migoni, R.L.: Atomic-level simulation of ferroelectricity in oxide materials. *Curr. Opin. Solid State Mater. Sci.* **9**(3), 107–113 (2005)
84. Smith, R.C., Hatch, A.G., Mukherjee, B., Liu, S.: A homogenized energy model for hysteresis in ferroelectric materials: General density formulation. *J. Intell. Mater. Syst. Struct.* **16**(9), 713–732 (2005)
85. Song, D., Li, C.J.: Modeling of piezo actuator's nonlinear and frequency dependent dynamics. *Mechatronics* **9**(4), 391–410 (1999)
86. Stancu, A., Ricinshi, D., Mitoseriu, L., Postolache, P., Okuyama, M.: First-order reversal curves diagrams for the characterization of ferroelectric switching. *Appl. Phys. Lett.* **83**(18), 3767–3769 (2003)
87. Stoleriu, L., Stancu, A., Mitoseriu, L., Piazza, D., Galassi, C.: Analysis of switching properties of porous ferroelectric ceramics by means of first-order reversal curve diagrams. *Phys. Rev. B* **74**(17), 174,107 (2006)
88. Sutor, A., Bi, S., Lerch, R.: Identification and verification of a Preisach-based vector model for ferromagnetic materials. *Appl. Phys. A: Mater. Sci. Process.* **118**(3), 939–944 (2014)
89. Sutor, A., Rupitsch, S.J., Lerch, R.: A Preisach-based hysteresis model for magnetic and ferroelectric hysteresis. *Appl. Phys. A: Mater. Sci. Process.* **100**, 425–430 (2010)
90. Szabó, Z.: Preisach functions leading to closed form permeability. *Phys. B: Condens. Matter* **372**(1), 61–67 (2006)
91. Takahashi, N., Miyabara, S.I., Fojiwara, K.: Problems in practical finite element analysis using preisach hysteresis model. *IEEE Trans. Magn.* **35**, 1243–1246 (1999)
92. Tan, X., Baras, J.S.: Modeling and control of hysteresis in magnetostrictive actuators. *Automatica* **40**(9), 1469–1480 (2004)
93. Tellini, B., Bologna, M., Pelliccia, D.: A new analytic approach for dealing with hysteretic materials. *IEEE Trans. Magn.* **41**(1), 2–7 (2005)
94. Visintin, A.: *Differential Models of Hysteresis*. Springer, Berlin (1994)
95. Viswamurthy, S.R., Ganguli, R.: Modeling and compensation of piezoceramic actuator hysteresis for helicopter vibration control. *Sens. Actuators A: Phys.* **135**(2), 801–810 (2007)
96. Völker, B.: Phase-field modeling for ferroelectrics in a multi-scale approach. Ph.D. thesis, Karlsruher Institut für Technologie (KIT) (2010)
97. Völker, B., Marton, P., Elsässer, C., Kamlah, M.: Multiscale modeling for ferroelectric materials: A transition from the atomic level to phase-field modeling. *Contin. Mech. Thermodyn.* **23**(5), 435–451 (2011)
98. Wang, D.H., Zhu, W.: A phenomenological model for pre-stressed piezoelectric ceramic stack actuators. *Smart Mater. Struct.* **20**(3), 035,018 (2011)
99. Webster, J.G.: *The Measurement, Instrumentation, and Sensors Handbook*. CRC Press, Boca Raton (1999)
100. Wen, Y.K.: Method for random vibration of hysteretic systems. *J. Eng. Mech. Div.* **102**(2), 249–263 (1976)
101. Wolf, F.: Generalisiertes Preisach-Modell für die Simulation und Kompensation der Hysteresis piezokeramischer Aktoren. Ph.D. thesis, Friedrich-Alexander-University Erlangen-Nuremberg (2014)
102. Wolf, F., Hirsch, H., Sutor, A., Rupitsch, S.J., Lerch, R.: Efficient compensation of nonlinear transfer characteristics for piezoceramic actuators. In: *Proceedings of Joint IEEE International Symposium on Applications of Ferroelectric and Workshop on Piezoresponse Force Microscopy (ISAF-PFM)*, pp. 171–174 (2013)
103. Wolf, F., Sutor, A., Rupitsch, S.J., Lerch, R.: Modeling and measurement of hysteresis of ferroelectric actuators considering time-dependent behavior. *Procedia Eng.* **5**, 87–90 (2010)
104. Wolf, F., Sutor, A., Rupitsch, S.J., Lerch, R.: Modeling and measurement of creep- and rate-dependent hysteresis in ferroelectric actuators. *Sens. Actuators A: Phys.* **172**, 245–252 (2011)

105. Wolf, F., Sutor, A., Rupitsch, S.J., Lerch, R.: Modeling and measurement of influence of mechanical prestress on hysteresis of ferroelectric actuators. *Procedia Eng.* **25**, 1613–1616 (2011)
106. Wolf, F., Sutor, A., Rupitsch, S.J., Lerch, R.: A generalized Preisach approach for piezoceramic materials incorporating uniaxial compressive stress. *Sens. Actuators A: Phys.* **186**, 223–229 (2012)
107. Xu, Q., Li, Y.: Dahl model-based hysteresis compensation and precise positioning control of an xy parallel micromanipulator with piezoelectric actuation. *J. Dyn. Syst. Meas. Control* **132**(4), 1–12 (2010)
108. Yi, K.A., Veillette, R.J.: A charge controller for linear operation of a piezoelectric stack actuator. *IEEE Trans. Control Syst. Technol.* **13**(4), 517–526 (2005)
109. Zhou, D., Kamlah, M.: Room-temperature creep of soft PZT under static electrical and compressive stress loading. *Acta Mater.* **54**(5), 1389–1396 (2006)
110. Zhou, D., Kamlah, M., Munz, D.: Effects of uniaxial prestress on the ferroelectric hysteretic response of soft PZT. *J. Eur. Ceram. Soc.* **25**(4), 425–432 (2005)